FERMILAB-THESIS-1979-08

SLAC-216
UC-34d
(T/E)

THE PRODUCTION OF NEUTRINOS AND NEUTRINO-LIKE PARTICLES IN PROTON-NUCLEUS INTERACTIONS*

John Patrick Dishaw
Stanford Linear Accelerator Center
Stanford University
Stanford, California 94305

March 1979

Prepared in part for the Department of Energy
under contract number DE-AC03-76SF00515
and the National Science Foundation

Printed in the United States of America. Available from National Technical Information Service, U.S. Department of Commerce, 5285 Port Royal Road, Springfield, VA 22161. Price: Printed Copy $8.00; Microfiche $3.00.

* Ph.D. dissertation.

THE PRODUCTION OF NEUTRINOS AND NEUTRINO-LIKE PARTICLES IN PROTON-NUCLEUS INTERACTIONS

John Patrick Dishaw
Stanford University, June 1979

An experimental search was performed to look for the direct production of neutrinos or neutrino-like particles, i.e., neutral particles which interact weakly with hadrons, in proton-nucleus interactions at 400 GeV incident proton energy. Possible sources of such particles include the semi-leptonic decay of new heavy particles such as charm, and the direct production of a light neutral Higgs particle such as the axion.

The production of these particles has been inferred in this experiment by energy nonconservation in the collision of a proton with an iron nucleus. The total visible energy of the interaction was measured using a sampling ionization calorimeter. The calorimeter was calibrated with muons. This calibration was adjusted slightly by requiring consistency in the calorimeter shower profile for primary interactions beginning at various depths in the calorimeter. Fluctuations in the electromagnetic and hadronic components were reduced using a weighted measurement algorithm. After correcting for beam intensity effects and cutting the data to eliminate systematic effects in the measurement, the final resolution of the calorimeter was 3.51% and increased with decreasing incident beam energy with a square root dependence on the beam energy.

Energy nonconservation in the data is manifest as a nonGaussian distribution on the low side of the calorimeter measured energy.

Model calculations yield the fraction of events expected in this nonGaussian behavior for the various sources of neutrinos or neutrino-like particles. A maximum likelihood fit to the data with the theoretical fraction of events expected yields the 95% confidence level production cross section upper limit values. The upper limits for general production of neutrino-like particles for various parameterizations of the production cross section are presented. The following specific upper limits have been established:

charm particle production	<	670 μbarns
supersymmetric particle production carrying an additional quantum number "R"	<	33 μbarns (mass of 1 GeV) 8 μbarns (mass of 3 GeV)
axion production	<	10^{-3} times the π^{o} production cross section

Acknowledgements

This experiment, like any undertaking of appreciable magnitude, involved the tireless efforts of a number of individuals. It is a pleasure to acknowledge these people.

The spirit, strength, and intelligence of Stanley Wojcicki permeated the entire experiment. I have yet to meet anyone whose mind moves as fast as Stan's. His hard work and limitless imagination saved the experiment from disaster any number of times. I also thank him for his endless patience in teaching this graduate student the art of experimental physics. I couldn't have had a better tutor.

Barry Barish offered brilliant insights in both the running of the experiment and during the analysis. I am especially thankful for his guidance during the early days of my experimental experience on the neutrino experiment.

I thank Frank Merritt for his work on the calorimeter calibration and maintenance of the analysis program. I also thank him for his intelligent comments and his many major contributions to all phases of the experiment. Dr. Merritt's Herculean work habits and dedication provided inspiration for us all.

I thank Arie Bodek and Mike Shaevitz for the construction and maintenance of the toroid spectrometer. I especially appreciate their indulgence in the game of musical chambers we played between the neutrino target and the toroid spectrometer.

I thank John Liu for his work on the initial phases of the experiment and the preliminary version of the analysis program.

I thank Alain Diamant-Berger for his work on the calibration and the tape writing routines. The shower calibration technique Alain initiated was truly brilliant.

I especially want to thank my fellow graduate students Wyatt Brown and Eric Siskind for their help in the grungy, usually monotonous, often boring details of the experiment. Eric deserves added thanks for his efforts in teaching me the fundamentals of electronics. I really appreciate Wyatt's work on the on-line software. I also thank Frank, Wyatt, Eric, Mike and Arie for the time they spent at Fermilab constructing the apparatus and for the day to day running of the experiment.

I thank Dan Porat for his design of the special electronics used in this experiment. Thanks also go to Dale Ouimette, Anthony Tilghman, and Len Birkwood for the construction of these electronics. Dale deserves special thanks for braving 95 degree Illinois heat with 85 percent humidity to help install the CD chamber system.

I thank Roger Coombes for the design of the calorimeter and time spent in its construction at Fermilab. I also thank Cliff Rasmussen for his help in the mechanical aspects of the experiment, especially the CD chamber system. Cliff's abilities are truly remarkable. I also thank Hank Thomas for his help in the initial phases of the experiment.

I thank the many people who worked on the toroid spectrometer, in particular James Lee and Paul Lindsay for their work on the acrylic counters. I would also like to thank George Krafcyzk and Gene Fisk for the use and maintenance of the 10' X 10' chamber used in the toroid system.

I thank Fritz Bartlett for his work on an implementation of the on-line data collection system. The power and beauty of this system was awe inspiring. I also thank Glennys Farrar for many informative discussions regarding the phenomenology of supersymmetry.

The Neutrino Lab at Fermilab deserves due credit for the success of this experiment. I thank Dick Lundy and Dennis Theriot for their support in all phases of the experiment. I thank Dennis for his perseverance and diplomacy during the critical times with the bubble chamber. Thanks go to Linda Stutte and Gordon Koizumi for their help on the beam line. I also thank Don Carpenter and the Lab 7 technicians for their technical assistance throughout the experiment. Special thanks are due to the Neutrino Lab Operations Crew. They were literally responsible for the effective running of the beam line and all accelerator interfacing. I sincerely appreciate their time and effort.

I thank Muzaffer Atac and John Urish for providing and maintaining the PWCs used in the upstream momentum tagging system. I also thank the Accelerator Division at Fermilab for their efforts during our run, especially for their work on improving the spill structure.

I acknowledge the SLAC Computer Center and its highly qualified staff for providing the powerful computing facility which performed the analysis chores on this experiment with very little machine associated difficulty. I would also like to thank the Technical Illustrations group at SLAC for providing the beautiful figures included in this thesis, many redone several times at the request of yours truly. I also thank Sally Lockhart for a fine job typing the final draft of this thesis.

I thank the U.S. Department of Energy and the National Science Foundation for financial support of this endeavor.

My sincere thanks also go to my wife, Debra, who suffered with me during our two year separation prior to our marriage while I was at Fermilab. I also thank her for her editorial skills in the creation of this tour-de-force document and for many hours spent typing into the computer a manuscript which looked like it had previously lined the bottom of a bird cage.

I feel that it is fitting at this time to thank those people who have contributed in so many ways to my development. I thank Jonas Schultz for first showing me the beauty of particle physics. I thank my good friend William Hill for stimulating discussions on any number of subjects over the years and for introducing me to the wonders of science. But of all the people who deserve thanks, my warmest, most heartfelt thanks go to my parents, Charles and Elizabeth Dishaw. Their hard work, loving guidance, and constant encouragement have furthered my development as an individual more than they realize. I thank them sincerely for their arduous labors.

In nomine Patris

et Filii

et Spiritus Sancti

Table of Contents

Chapter Page

I. Introduction 1

II. Theoretical Motivation and Existing Data 7

A. Heavy Particle Decays 7

1. Charmed Particles 7

2. Heavy Lepton Decays 13

3. Neutral Vector Boson Decay 14

4. Supersymmetric Theories of Strong Interactions .. 16

B. Weakly Interacting Particles 20

1. Axions 21

2. Existing Data on Long-lived Particles 23

C. Summary 25

III. Experimental Apparatus 27

A. Beam 28

B. Calorimeter 31

C. Trigger Counters and Logic 39

D. Electronics 43

E. Data Collection 47

IV. Data Taking Procedures 49

A. Normal Running 49

B. I.B. Runs 50

C. Muon Runs 50

V. Data Analysis 52

A. ADC Response 52

B. Calorimeter Calibration 53

1. Muon Calibration 54

2. Shower Calibration 57

3. Minimization of the Resolution 60

4. Weighting 61

C. Rate Corrections to the Energy 72

1. EVENT HISTORY Correction 72

2. FLYING SCALER Correction 79

D. Data Cuts 82

1. Position of Primary Interaction 82

2. Total Energy Sum 85

3. Shower Profile Cuts 85

4. Upstream Interaction Cuts 87

5. Muon Cuts 90

VI. Results and Conclusions 96

A. Calorimetry Backgrounds 96

B. High Energy Tail 102

C. Missing Energy Monte Carlo 108

D. Maximum Likelihood Analysis 110

1. Supersymmetric Particles 112

2. Charm Production 113

3. General Particle Production 119

E. Conclusions 124

Appendix A - Hadron Calorimetry 126

1. Physical Processes in Hadron Calorimetry 127

2. Calorimeter Design Considerations 129

Appendix B - Photomultiplier Gain Tests 137

References 141

List of Tables

Page

I. Experimental sensitivity to weakly interacting particles. 8

II. Calibration results 72

III. Percentage of events lost by cuts 94

IV. Expected and observed number of low energy events 98

V. Supersymmetric particle limits 114

VI. Charm particle limits 118

VII. General particle limits 120

VIII. Axion production limits 123

List of Figures

Page

1. Neutrino production through heavy particle decay. (a) Charm particle production and decay, (b) heavy lepton production and decay 9

2. Neutrino production through Z^o decay. (a) Z^o production through quark-anti-quark annihilation, (b) Z^o production through the decay of a $\psi(3100)$ 15

3. Diagrams contributing to the decay of a supersymmetric particle 18

4. Fermilab external beam lines 29

5. Fermilab N-5 hadron beam line 30

6. Upstream portion of the E-379 apparatus 32

7. Light flasher trigger logic 36

8. Electronics for calorimeter energy measurement 38

9. E-379 experimental apparatus 40

10. Beam trigger logic 42

11. Typical EVENT HISTORY distribution 45

12. Muon pulse height in the HIs 56

13. Shower profile second moment distribution 63

14. Calorimeter performance -vs- second moment 64

15. Calorimeter performance -vs- weighting fraction 66

16. Measured energy distribution after weighting 68

17. Probability distribution for the measured energy. (a) Unweighted energy, (b) weighted energy 69

18. Measured energy -vs- incident beam energy 70

19. Calorimeter resolution -vs- incident beam energy 71
20. Beam intensity effects on the measured energy 73
21. Flasher difference -vs- hit position in the FLASHER HISTORY 76
22. X^2-vs- time constant for the EVENT HISTORY correction 77
23. Measured energy after EVENT HISTORY correction 78
24. Fractional measured energy change -vs- FLYING SCALER rate parameter 81
25. Measured energy after EVENT HISTORY and FLYING SCALER correction 83
26. Comparison of high intensity corrected and low intensity measured energy 84
27. Measured energy -vs- position of first interaction 86
28. Measured energy -vs- energy deposition in Chief 88
29. Measured energy -vs- fraction of energy deposited in the first 20 plates 89
30. Chief distribution for momentum analyzed muons 92
31. Measured energy for final data sample 95
32. Low energy distribution for final measured energy 97
33. EVENT HISTORY distribution for high intensity data 105
34. B0 distribution for high energy tail events 107
35. Typical maximum likelihood distribution 111
36. Laboratory neutrino energy spectrum for D decay 117
37. Typical profile for a hadronic shower in the calorimeter ... 130
38. Shower profile for 400 GeV in the E-379 calorimeter 131
39. Effect of non-containment on the measured energy 133
40. Effect of sample spacing on the calorimeter resolution 136

41. Photomultiplier gain test apparatus 138
42. Photomultiplier gain test results 139

CHAPTER I

Introduction

The weak force plays a unique role in the scheme of particle physics. The weak interactions are responsible for the decays of the long lived particles. These particles can not decay via the strong interactions because of either kinematic or quantum number effects involved in the decay.

As an example consider the decays of the charged pi-meson (pion) and K-meson (kaon). The pion is a member of the lightest strongly interacting multiplet. Consequently the pion cannot decay by strong interactions into other hadrons and can only decay weakly. The pion decays almost 100 percent of the time into a muon and a neutrino. Other pion decays are several orders of magnitude less probable than the above muon decay. The decay of the kaon is a more interesting case. The kaon has a mass of more than three times the mass of the pion and one would naively expect the kaon would decay very quickly into pions by way of the strong interactions. The kaon does not decay this way, however, because it carries an additional property called strangeness. Strangeness is conserved in strong interactions and the kaon is the lightest particle with this property. Thus, as with the pion, the kaon only decays through the weak interactions. Unlike the pion, the kaon has a large contribution to its decay rate from hadronic decays, but its branching ratio into a muon and a neutrino is still large, about 64 percent {1}. As a comparison between the effects of strong and weak interactions in the decays of particles, consider the rho meson. This particle is allowed to

decay via strong interactions. The rho meson has a lifetime of 10^{-24} secs {1} and decays almost exclusively into two pions. The lifetime of the kaon on the other hand is 10^{-8} secs {1}.

The same quantum number considerations which play such a dominant role in the decay of the lightest strange particles such as the kaon play an analogous role in the decays of the "new" particles, the lightest charmed mesons {2}. Energy conservation requires that a heavy particle decay into a lighter particle. The light charmed hadrons cannot decay into lighter hadrons and still conserve their charm characteristic. Since charm is conserved in strong interactions these particles can not decay via strong interactions, but can only decay weakly into other particles. Because the charmed particles are so heavy, the number of weak hadronic decay modes is much larger than in the kaon case, but the leptonic modes in the decay of this particle are still significant, their sum being approximately 22 percent {3}.

In view of the above quantum number effects in the decays of strongly interacting particles, a natural experimental question is how one can go about detecting the production of new particles in strong interactions. If this new particle is heavy, such as in the charm case, the hadronic decay modes constitute a major fraction of the decays. Traditionally in searches for new states, combinations of secondary pions (and/or kaons) are studied and an enhancement in the effective mass distribution of these pions is viewed as an indication of a particle. For the "new" particles, this method has problems. Since the production cross section for these "new" particles is presumably small, just the phase space combinatorics of uncorrelated

particles will swamp the search with a large background. These hadronic backgrounds can be circumvented however, if one concentrates on the leptonic decays. One important question is whether the branching ratio into leptons is large enough to accommodate a significant yield in the data. From the previous discussion, it would seem that the leptonic branching ratios are large enough to produce a measurable rate. A problem with this technique is that the neutrino in the final state is not detected, and thus the mass of the decaying particle cannot be reconstructed. Because of this fact, production of these "new" particles is manifested as an enhanced signal of leptonic final states over the background in lieu of a mass bump in an effective mass distribution.

In an experiment performed at the Fermi National Accelerator Laboratory, our collaboration decided to search for the production of new particles in proton-nucleus collisions by concentrating on these leptonic decay modes. Muonic decay modes were used in lieu of electronic modes because of the easy identification of muons by their penetration through large amounts of matter. This identification, as well as momentum analysis of the produced muons, can be accomplished by using a solid steel toroid system placed behind the target that has been magnetized to saturation. By dispersing spark chambers throughout the toroid system, one can measure the deflection of the muon trajectory in the magnetic field in the steel and determine the momentum. Identification is achieved simply by the penetration.

Along with muons, neutrinos are presumably produced in the decay of these new particles. A typical signature for a new particle decay then, would be a muon with energy missing from the interaction.

This missing energy is due to the neutrinos which carry away energy from the decay. The missing neutrino energy can be determined if the target is also a calorimeter. The calorimeter would measure the total energy of the hadronic system in the interaction. This measurement, in combination with the muon energy would yield the neutrino energy. The neutrino energy is found by comparing the sum of the calorimeter and muon energies to the incident proton energy. Any difference between these two must be due to neutrinos.

Since the incident energy is important in the missing energy comparison, it should be known precisely for each event. In this experiment, the incident proton was allowed to pass through an air-gap magnet immediately before the target-calorimeter. By measuring the deflection of the proton trajectory in this magnetic field, one obtains the momentum of each proton striking the target-calorimeter, removing any doubts about the incident energy.

Combining all of the above elements together the result is a consistent set of apparatus for measuring the muonic decays of new particles. This apparatus consists of a momentum analyzed proton beam striking a target-calorimeter with the final state muon energy measured in a solid steel magnet system.

As well as measuring the neutrino energy associated with muons produced in new particle decay, the calorimeter allows us to measure the production of other particles also. To see this, consider the interaction of a proton in the calorimeter. At some level the measured energy should be statistical in nature, leading to a Gaussian response function for the measured energy. The Gaussian shape can be altered, however, if for some reason large amounts of energy were

leaving the calorimeter undetected. Such a source of undetected energy would be the production of neutrinos or neutrino-like objects which interact only weakly with the nuclei in the calorimeter. Since they do not interact, any energy going into these objects will not be deposited in the calorimeter. This alters the Gaussian profile of the calorimeter distribution by the addition of a low energy tail arising from those events which have a large amount of energy going into this neutrino-like sector.

A calorimetry search is sensitive to the above production over a wide and previously unexplored region of kinematic variables. If the source of these neutrinos were the decay of some unstable particle, then the decay has to occur before the particle can interact with the nuclei of the calorimeter. This requires that the lifetime of these particles be shorter than 10^{-10} secs. If this undetected energy is due to the production of some new neutrino-like object, then this means that the particle must leave the calorimeter without interacting. This implies that the particle-nucleus cross section must be less than one percent of the proton-nucleus cross section for a typical calorimeter of approximately 20 absorption lengths. If these neutrino-like particles can decay, then the fact that they must leave the calorimeter before decaying puts a lower limit of 10^{-9} secs for the lifetimes of these particles.

An experiment of this magnitude searches for new particle production in several ways. One hopes to see an enhanced signal of single muons coming from the primary interaction as an indication of new particle production. Simultaneous decay of pair produced new particles would lead to muon pair production with a large amount of

missing energy. Finally, extra low energy tails on the calorimetry data would yield evidence for new particle production. What follows addresses the last of these possible signals. During the course of the muon running indicated above, a small fraction of proton calibration events were taken as a running monitor of the calorimeter performance. This thesis is an analysis of this calorimetry data in order to search for the production of neutrinos or other neutrino-like objects.

Chapter II is a discussion of a few viable theoretical candidates for these particles, Chapter III is a discussion of the apparatus, and Chapter IV describes the data taking procedures of the experiment. Chapter V is a detailed presentation of the calorimetry analysis and finally, Chapter VI gives the results and conclusions derived from the calorimetry data.

CHAPTER II

Theoretical Motivation and Existing Data

As discussed in the previous chapter, a calorimetry search is sensitive to two classes of particles. The first class is those states that decay rapidly into neutrinos or neutrino-like particles. The second class is particles which are long-lived and interact only weakly with the nuclei of the calorimeter. To emphasize this point further Table I shows the range of lifetimes and cross sections for which a calorimetry search is sensitive. Also noted are the other types of experiments which are sensitive in these particular ranges. The rest of this chapter will discuss these two classes of particles.

A. Heavy Particle Decay

1. Charmed Particles

A very likely candidate for the new particle decays would be hadronic production of charmed particles {4}. As mentioned in the first chapter, the lightest charmed mesons can only decay weakly. The strong decays are forbidden by conservation of charm. Because of this, the branching ratio for charmed mesons into leptons is large. Measurements at e^+-e^- colliding beam accelerators indicate semileptonic branching ratios of approximately 11%. Copious production of charmed particles in proton-nucleus collisions followed by their semileptonic decay, as shown in figure 1(a), would lead to a substantial production of neutrinos.

The experimental situation in hadronic charm production has

TABLE I

EXPERIMENTAL SENSITIVITY TO WEAKLY INTERACTING PARTICLES

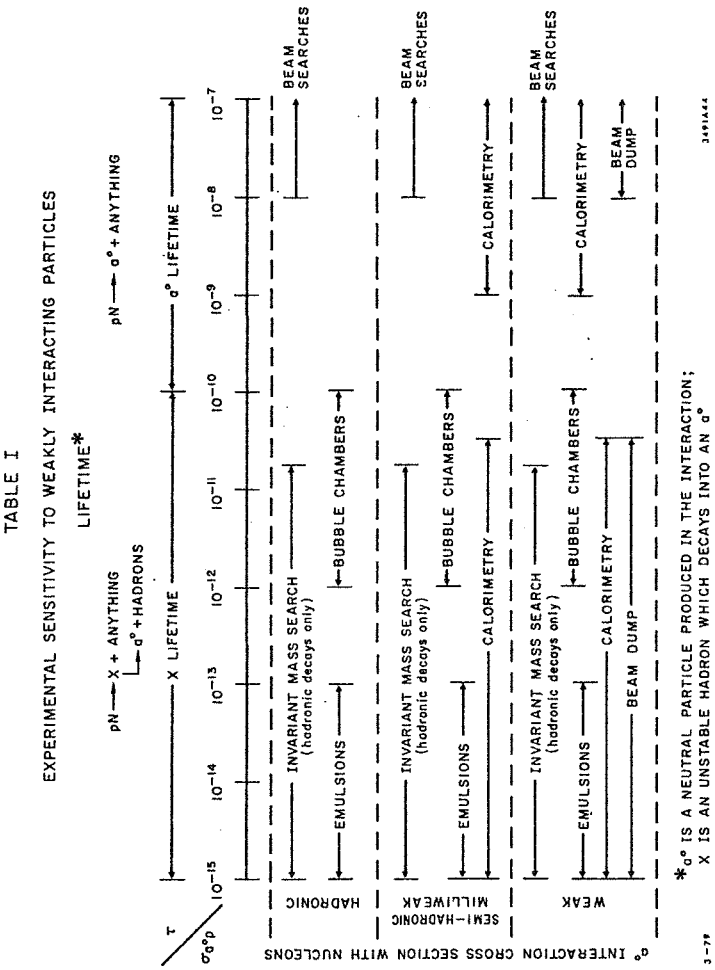

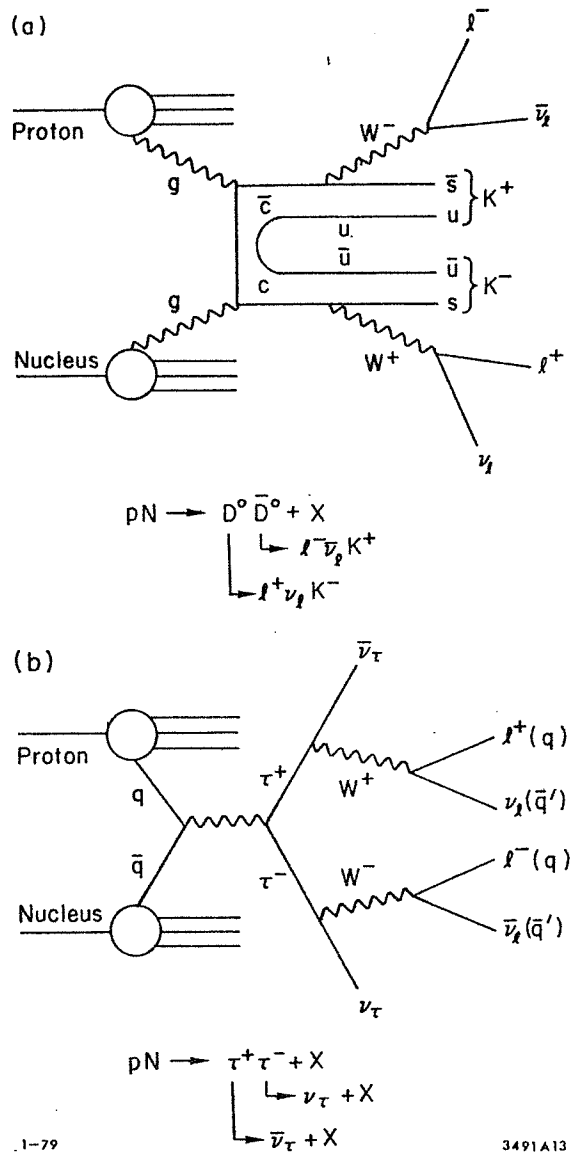

Fig. 1 (a) Hadronic pair production of charmed D mesons and semi-leptonic decay of these mesons into $K^{\pm}l^{\mp}\nu(\bar{\nu})$.
(b) Hadronic production of $\tau^{+}\tau^{-}$ via a quark-anti-quark annihilation process. The τ decays producing a ν_{τ} plus final states containing other leptons and hadrons.

recently been reviewed by Diebold {5}. Charm search experiments have been performed at a variety of energies, but charm production cross sections rise steeply with center of mass energy {6} so that it probably only makes sense to consider the high energy searches for comparison in this thesis. There are three basic techniques that have been pursued in searches for charm: (1) mass reconstruction of the hadronic decay products (almost exclusively $K^{\pm}\pi^{\mp}$), (2) looking for short tracks in emulsions arising from decays of short lifetime particles, and (3) anomalous production of leptons in hadronic interactions as an indication of the weak decay of a charmed particle ($e^{\pm}, \mu^{\pm}, e^{\pm}\mu^{\mp}, \nu$). The individual experiments will be considered below.

Several experiments {7} have searched for charm production in the $K^{\pm}\pi^{\mp}$ invariant mass distribution. A bump in this distribution is expected from the decay $D^{o} \rightarrow \pi^{+} K^{-}$, $\overline{D^{o}} \rightarrow \pi^{-} K^{+}$. As mentioned previously, this method seems ideal for finding charmed particles, but the experimental searches are dominated by a large background from the phase space distribution of uncorrelated πs and Ks. The most restrictive of these is Ditzler et al., who place a limit of $\sigma_{c} < 108$ μbarns/nucleon {8}.

A few groups {9} have searched for short tracks in nuclear emulsions exposed to hadron beams as evidence for charm production. These short tracks would presumably arise from the production of a charmed meson which travels a small distance in the emulsion before decaying. These experiments are very sensitive to the lifetime of the charmed meson because of the limited scanning range for visible decays {10}. If we take 3×10^{-13} as a measure of the D lifetime {11},

then the cross section limits range from < 3 μbarns to as much as < 40 μbarns. A recent measurement by Ushida et al. has established a positive charm signal of 25 ± 13 μbarns for charm production at 400 GeV which is inconsistent with previous limits. This inconsistency may be due to scanning inefficiencies in the earlier experiments. Even so, a charm cross section of from 5-15 μbarns is not inconsistent with these experiments.

The anomalous production of $e^{\pm}\mu^{\mp}$ pairs in hadronic interactions has been investigated as an indication of charm production. This final state configuration cannot come from electromagnetic sources such as lepton pair production or the decays of known mesons, but could be due to the associated production and weak decay of charmed particles where one of the particles decays into an electron and one decays into a muon. Two colliding beam experiments at 53 GeV center of mass energy have published results on this signature {12}. L. Baum et al. have set a limit of < 91 μbarns for the production of charmed particles from this source (taking a 10% branching ratio into leptons for D decay). A. G. Clark et al. have seen a positive signal of 70 ± 36 μbarns for charm production. Scaling this number to 400 GeV (center of mass energy of 27.4 GeV) {6,18} yields a cross section of 23 ± 12 μbarns for charm. This is consistent with a limit of 51 μbarns set by an $e^{\pm}\mu^{\mp}$ search using 300 GeV neutrons {13}.

As well as the production of lepton pairs, the production of single leptons in hadronic interactions is also indicative of weak decays of new particles. Investigating a prompt muon signal, our collaboration has determined that approximately 50% of the prompt muons in the kinematic range of p_T from $.8 < p_T^{\mu^+} < 1.5$ GeV/c and

low x_F ($12 < E_{\mu^+} < 50$ GeV, where E_{μ^+} is the muon energy) occur singly. Assuming that all of these prompt single muons originate from weak decays yields a cross section of approximately 30 μbarns/nucleon for the production of charm particles {14}. An earlier measurement of the polarization of prompt muons had previously set a limit of less than 10% of the prompt muons arising from weak decays of new particles {15}. This previous experiment was performed at high p_T and is not inconsistent with the single muon measurement of our group.

Of the lepton searches, the ones most directly applicable to this analysis are the so called beam dump experiments {4}. In these experiments, one dumps a beam of protons onto a thick target and attempts to detect neutrinos produced in the proton interactions downstream of the target. The thick target severely suppresses neutrino production from uninteresting long lived particle decay so that neutrinos could only be coming from the decays of short lived objects such as charmed particles. After subtracting for a residual contribution to the detected neutrinos from unabsorbed background decays, one is left with an enhancement indicating a prompt neutrino signal. Using various models for the production and decay of charm particles, the prompt neutrino signal yields a charm cross section. The high energy beam dump experiments have all seen positive signals for prompt neutrino production. Model dependent calculations yield charm cross sections of from 25 to 50 μbarns (assuming linear A dependence) for BEBC and Gargamelle. The CDHS group has measured a smaller cross section of 10 μbarns. The discrepancy between the CDHS measurement and the other two measurements is not presently understood.

It is very difficult to compare the charm search experiments

because of the model dependent calculations for the experimental acceptance. The problem lies in the fact that most experiments see only a small percentage of the produced charmed particles. The fraction detected is intimately connected to the dynamics of the production process. Different models for these production mechanisms lead to a different acceptance and thus to a different total cross section. The problem is compounded further by the fact that most experiments use nuclear targets rather than hydrogen. To obtain the cross section on protons alone (i.e. cross section per nucleon) one must assume a model for the A dependence of the cross section. Given all of the above fiats, it appears that a charm cross section of from 10 - 50 μbarns is not inconsistent with the available data.

2. Heavy Lepton Decays

The discovery of the τ heavy lepton in e^+-e^- annihilations {16} indicates that there now exist three charged lepton pairs in nature, the electrons, muons, and the τs. Unlike the other two, the τ is very short lived ($\Gamma^{-1} < 2.3 \times 10^{-12}$ secs.) {17} and decays quickly into a τ neutrino (ν_τ) plus other particles, some of which could be additional neutrinos. Hadronic production of a $\tau^+\tau^-$ pair as shown in figure 1(b), could lead to a missing energy tail due to these neutrinos.

The number of τ leptons produced in proton-nucleus interactions can be calculated using the data from direct $\mu^+\mu^-$ production in hadronic interactions {18}

$$\sigma_{total}\,(pp \to \tau^+\tau^-) = \int_{2m_\tau}^{\infty} \frac{d\sigma}{dM}\,(pp \to \mu^+\mu^-)\,dM$$

Taking a mass dependence for this μ pair cross section of the form {18}

$$M^3 \left.\frac{d^2\sigma}{dMdy}\right|_{y=0} = 3 \times 10^{-32} e^{-14.9\, M/\sqrt{s}}\ cm^2\text{-}GeV^2$$

and assuming a flat y distribution, the above integral yields

$$\sigma_{total}(pp \to \tau^+\tau^-) = .184 \text{ nanobarns}$$

Of the 150,000 proton interactions considered in this thesis, the above total cross section corresponds to .002 events. Thus $\tau^+\tau^-$ production is not a major contribution to the low energy calorimeter distribution.

3. Neutral Vector Boson Decays

Production and decay of the neutral intermediate vector boson, Z^o {19}, could be a possible source of neutrinos in hadronic interactions. One possible mechanism would be the production of the Z^o through quark-anti-quark annihilation similar in spirit to the Drell-Yan model {20}. This mechanism is shown in figure 2(a). Because of the limited energy available in the center of mass, 400 GeV proton interactions on a stationary target would only be sensitive to masses for the Z^o of 27 GeV or less. Gauge theory estimates of the Z^o mass place it in the area of 70-100 GeV {19} so that such quark-anti-quark mechanisms should not produce a Z^o.

A virtual Z^o could be produced through resonance production of a ψ(3100) {21} and its subsequent decay into a virtual Z^o. Such a mechanism is shown in figure 2(b). Estimates of the $\nu\bar{\nu}$ decay mode of the ψ(3100) {22} yield a ratio

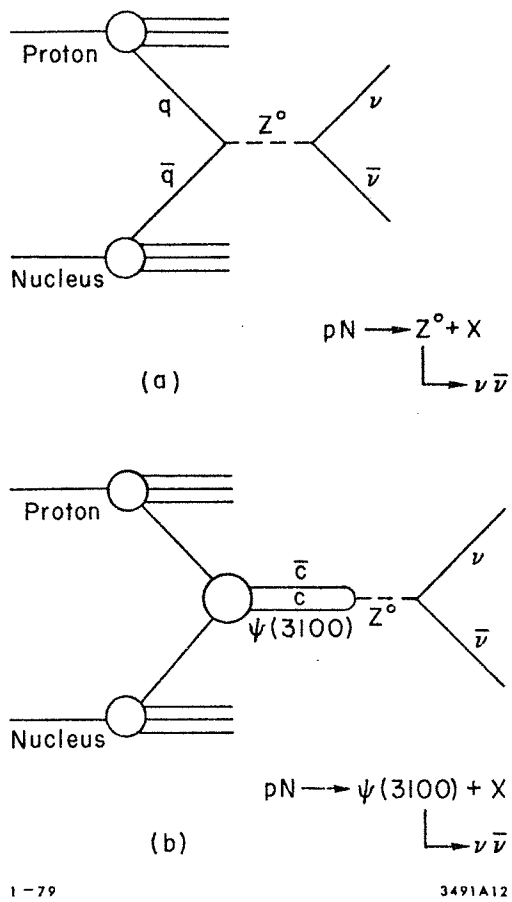

Fig. 2 (a) Hadronic production of the Z^o through a quark-anti-quark annihilation process. The Z^o then decays into a $\nu\bar{\nu}$ pair.
(b) Hadronic production of the Z^o through resonance production of a $\psi(3100)$.

$$\frac{\Gamma\ (\psi \rightarrow \nu\bar{\nu})}{\Gamma\ (\psi \rightarrow \mu^+\mu^-)} \simeq \frac{3\ (G_F/\sqrt{2})^2}{(4/9(\alpha/M^2_\psi)^2} \simeq 10^{-3}$$

where the factor of 3 comes from the number of possible neutrinos in the decay and the factor 4/9 is the charge of the charmed quark squared. Many measurements of $\psi(3100)$ {21,33} production have been performed which indicate a significant ψ cross section. Using this experiments value of 21 nanobarns {24} for the total $\psi(3100)$ production cross section followed by $\mu^+\mu^-$ decay, one expects only

$$N_{\psi \rightarrow \nu\bar{\nu}} = 10^{-3}\ (21 \times 10^{-33}\mathrm{cm}^2/87 \times 10^{-33}\mathrm{cm}^2)$$
$$= .25 \times 10^{-3}$$

where the denominator is the single event cross section for the data reported here. Thus, this source of prompt neutrinos is also not very viable.

4. Supersymmetric Theories of Strong Interactions

If the present ideas on supersymmetry are correct, then an additional source of heavy particles which could decay into neutrino-like objects comes from those particles carrying the additional supersymmetry quantum number. A brief discussion of the principles of supersymmetry and the phenomenology associated with this new symmetry are discussed below.

One of the basic fundamental tenets of all physical theory is that the laws of nature are invariant under Lorentz transformations. This property is Poincare invariance. It could be possible though, that the laws of nature are invariant under an even larger group of transformations, a symmetry which requires invariance under Poincare

transformations, but also invariance upon transformations of spin, i.e., from fermions to bosons and vice versa. Such a symmetry is called supersymmetry {25} and has been under theoretical investigation for the past several years.

In supersymmetric theories, rotations of spin are accomplished by application of spinorial generators which rotate fermions into bosons and vice versa. The spinorial generators form an algebra with the Poincare generators and the Lagrangian of the interaction is formulated in such a way to be invariant under all transformations. If supersymmetry were exact then for each fermion there would exist a boson partner and vice versa in a large particle multiplet. This leads to such undesirable characteristics as spin-0 leptons and spin-1/2 vector bosons. Clearly, supersymmetry has to be broken. However, if it is broken in a gauge invariant way, then the interaction may still be supersymmetric even though the undesirable particles are extremely massive and undetectable {26}.

Supersymmetric theories lead to an interesting phenomenology. There exist realistic models of elementary particle interactions incorporating supersymmetry {27}. These have an additional conserved quantum number designated R. Demanding R invariance in the interaction of elementary particles requires that the supersymmetric partners of the octet of gluons (gluinos) should be massless. Since gluinos interact with quarks strongly, this gives rise to new hadrons, R-hadrons, containing this new quantum number. The traditional particles all have R=0 while an interesting managerie of particles exist with R=1. In addition, some of these hadrons will decay, as shown in figure 3 ("nuino" stands for a gluino or photino, the fermionic partner of the

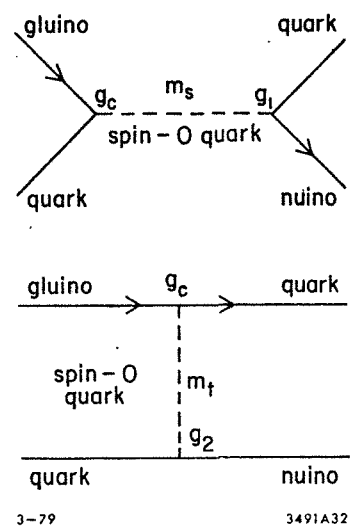

Fig. 3 Diagrams contributing to the decay of a supersymmetric particle. "gluino" is the supersymmetric partner of the gluon, "nuino" represents a photino (the supersymmetric partner of the photon) of a gluino, g_c is the strong coupling constant and g_1, g_2 are the coupling for the nuino and the spin-0 quark.

photon). The lifetime of such particles can be estimated if it is assumed that supersymmetry is broken in a way similar to weak interaction spontaneous symmetry breaking {27}. In this case the mass of the exchange particle in the t (m_t) and s (m_s) channels is m_W, the mass of the intermediate vector-boson. The coupling constants in those two channels, g_1, and g_2 respectively, are then equal to the weak coupling constant g so that the decay coupling strength is

$$G_{decay} \simeq \frac{g_1 g_c}{M_t^2} \simeq \frac{g g_c}{M_W^2} \simeq \frac{g_c}{g} G_F$$

where g_c is the strong coupling constant. Taking $g^2/4\pi = \alpha$ and $g_c^2/4\pi = .1 \rightarrow 1$ an estimate of the lifetime for a R-hadron mass of approximately 1.2 GeV/c yields $\tau = 10^{-12} - 10^{-15}$ secs. An additional factor of 20 over the weak decay lifetimes is obtained because there is no $\sin^2\theta_c$ factor in these decays. This lifetime range is well within the sensitivity of this experiment as shown in Table I. A requirement for detection of these particles in this experiment is that the nuino leaves the calorimeter without interacting which implies, from Table I, that the nuino-nucleus cross section be less than 1% of the total proton-nucleus cross section. To get an estimate of the nuino interaction cross section we only need to look at the diagrams in reverse. This leads to a cross section estimate of

$$\sigma_{nuino\text{-}proton} \simeq \frac{g_c^2}{g^2} \sigma_{\nu p}$$

again, well within the limit of $10^{-2}\ \sigma_{pp}$ required in this experiment {27}.

All of the above considerations are highly model dependent, but serve to illustrate that a calorimetry search is sensitive to this type

of production. It is also worth adding that although our sensitivity does require a certain window on the nuino interaction cross section, this window is not very restrictive and makes this experiment much more insensitive to this model dependent calculation than other experiments which require the nuino to interact to be detected.

B. Weakly Interacting Particles

As previously discussed and shown in Table I, a calorimetry search is sensitive not only to the production and decay of short lived heavy particles, but also to the direct production of weakly interacting particles. As indicated in Table I, the lifetimes of these particles have to be longer than 10^{-9} secs in order to leave the calorimeter before decaying. Also, the interaction cross section of these particles with nuclei has to be less than 1% of the proton-nucleus interaction cross section since they must leave the calorimeter (~20 interaction lengths) without interacting.

There exist several theoretical candidates for such massive weakly interacting particles. The Higgs particles in standard gauge theories of weak interactions would satisfy such constraints {28}. Lately, interest has turned to a light pseudo-scaler Higgs-type particle called the axion {29}, which may be necessary in removing CP violation in strong interactions. This particle will be discussed more fully below. Extended theories of the weak interaction with large gauge groups require heavy neutral leptons which could be detected in a calorimetry search such as this {30}. Recently R. Cahn has postulated that the next generation of quarks (truth and beauty) may be quasi-stable and fall into the

category of weakly interacting and long-lived particles {31}. If these ideas are correct then a calorimetry search is sensitive to this type of production.

Present experimental limits and the axion case are discussed below.

1. Axions

In the last years, there has been a tremendous amount of theoretical discussion concerning the possible existence of a light, neutral, quasi-stable particle called the axion or higglet {29}. Briefly, this particle arises in a somewhat natural way in the consideration of field theories of strong interactions. Due to non-unique vacuum solutions to the field equations of the theory (instantons) {32}, the Langrangian of the theory contains a form which violates CP (charge conjugation times parity) invariance in strong interactions {33}. Strong experimental evidence indicates that CP is a conserved quantum number in strong interactions so that these CP violating terms in the Langrangian must be spurious. One method to eliminate these terms is to impose an additional symmetry (with a symmetry group U(1)) on the Langrangian {34}. Invariance under this new symmetry then allows one to rotate into a frame where these CP violating terms vanish. To impose this additional symmetry, one incorporates a new doublet of particles. After all of the dust settles (spontaneous symmetry breaking, Higgs mechanism, etc.), one is left with a light ($\approx$100 KeV) long lived (τ = .3 secs) neutral particle, the axion.

Model dependent estimates of the axion decay mode of the kaon {29,35} yield values which are only an order of magnitude less than the present

upper limit on this decay {35}. Theoretical calculations {36} of the product of the axion production and interaction cross sections are approximately an order of magnitude or more greater than the upper limits for this quantity from the beam dump experiments {4}. Although these limits do not bode well for the axion, there is some room left in the experimental data for the axion to exist {28}. There are models of the axion with a larger symmetry group which would incorporate the kaon data and still leave the axion intact to help with CP {37}. Also, the axion could be more massive than first believed {38}. If the axion exists, it should be produced in hadronic interactions. Estimates of the axion-proton cross section yield values on the order of 10^{-8} times the pion-proton cross section {29}. Thus the produced axion would leave the calorimeter without interacting. This would yield a missing energy tail, similar to neutrinos in the measured energy distribution and thus this experiment is sensitive to this production and can establish limits on its cross section.

It should be noted that there are other mechanisms besides the axion mechanism which would eliminate the CP non-conserving terms in the Lagrangian. One way is to require that one of the quarks be massless {39}. The massless quark is usually taken to be the up quark. There are problems with this approach because of the fact that calculations using current algebra relations and the SU(3) properties of the pseudoscaler mesons yield a finite mass for the quarks {40}. One must be sure that in assigning a massless up quark, one is consistent with these calculations. Recent work seems to indicate that these current algebra results remain when the up quark is massless {39}.

2. Existing Data on Long-lived Particles

Several searches for long-lived particles have been performed at high energy accelerators. Most of these searches have looked for massive charged particles. In these types of experiments, one chooses a momentum for the particles produced in a target. The mass of the produced particle is then determined by time of flight information for the particle. Using this method several experiments {41} have set limits on the invariant cross section of from .01-4 μbarns/GeV for the production of massive penetrating charged particles. These limits are sensitive to the mass and lifetimes of these particles.

Only a few searches have been performed looking for neutral particles. Gustafson et al. {42} have performed a search for neutral hadrons with mass greater than 2 GeV using time of flight techniques and a hadron calorimeter to measure the neutral particle energy. Using their data they set limits of

$$E \frac{d^3\sigma}{dp^3} < 10^{-32} - 10^{-34} \text{ cm}^2 \text{ GeV}^{-2}$$

for various masses. Since the particle is required to interact in the calorimeter this places a lower limit of $> .1\ \sigma_{pp}$ for the interaction cross section of these particles. Bechis et al. {43} have searched for neutral heavy leptons produced on p-C interactions by looking downstream of a thick target for the decay

$$L^o \rightarrow \mu^{\mp}\pi^{\pm}$$

They quote a limit of

$$BR(L^o \rightarrow \mu^{\pm}\pi^{\mp})\sigma(pN \rightarrow L^o) < 3 \times 10^{-35} \text{cm}^2/\text{nucleon}$$

for masses less than 1 GeV and a lifetime range between 10^{-10} and 10^{-8} secs. This measurement also requires $x_F = P_L^* / 2\sqrt{s}$ to be greater than

0.2. The fact that the heavy leptons must pass through the thick target implies an upper limit for the interaction cross section of $< .02\ \sigma_{pp}$.

In addition to neutrinos, the beam dump experiments mentioned previously can place limits on the production of neutral weakly interacting particles as well. In this case, an excess of neutral current type events over that expected from normal neutrino interactions would indicate the production of a new neutral particle. Since this neutral particle must interact to be detected, one can only set limits on the product $\sigma(pN \rightarrow a^o)\ \sigma\ (a^oN \rightarrow X)$ where a^o is the neutral particle and N the target nucleus. The high energy beam dump experiments set limits of

$$\sigma(pN \rightarrow a^o)\ \sigma\ (a^oN \rightarrow X) < 10^{-67} \text{ cm}^4$$

This is to be compared with 9×10^{-66} cm^4 as calculated by Ellis and Gaillard {35} for the case where a^o is the axion discussed above. If one assumes that both the interaction and production cross sections of these particles is related to the pion cross sections

$$\sigma(pN \rightarrow a^o) \simeq R\sigma(pN \rightarrow \pi^o) \quad ; \quad \sigma(a^oN \rightarrow X) \simeq R\sigma(\pi^oN \rightarrow X)$$

then one obtains

$$R < 10^{-8}$$

which is 2 orders of magnitude smaller than the limit from kaon decay for a light neutral particle {32}

$$\frac{\Gamma\ (K^+ \rightarrow \pi^+ a^o)}{\Gamma\ (K^+ \rightarrow \text{all})} < 10^{-6}$$

The beam dump limits would have to be corrected however, if the neutral particle had a shorter lifetime then expected because of possible decay before reaching the detector.

C. Summary

How does a calorimeter search compare with the beam dump experiments? Since calorimetry measurements are affected by the incident beam intensity, the data taking rate is limited. The beam dump experiments on the other hand are only limited by the accelerator intensity. Correspondingly, the beam dump experiments are more sensitive to direct neutrino production. However, a calorimeter search is nicely suited for detecting particles that decay into something other than neutrinos where the decay product has an interaction cross section less than 1% of the proton interaction cross section but greater than the neutrino interaction cross section or where the decay product has an interaction cross section much less than the neutrino cross section.

For detection of weakly interacting particles a calorimetry search is less sensitive than a beam dump experiment to theoretical estimates of the particle interaction cross section since the particle need not interact to be detected but only has to leave without interacting. This advantage is negated somewhat by the finite resolution of the calorimeter.

For the detection of new long-lived particles, a calorimeter search has the advantage that the beam search experiments do not have that all masses and all lifetimes greater than 10^{-9} secs are simultaneously measured. However, this property also implies that if something were

leaving the calorimeter, the mass and lifetime are unknown. Since the neutral particle must interact to be detected, the same comments with regards to the interaction cross section of these new particles for the beam dump experiments also apply to the beam search experiments.

CHAPTER III

Experimental Apparatus

This experiment was performed at the Fermi National Accelerator Laboratory using the hadron beam in the Neutrino area. Four hundred GeV protons from a production target 1 km upstream of our apparatus were incident on the target calorimeter located in Lab E. The incident energy of each beam particle was momentum analyzed and the energy of the interaction was measured in the hadron calorimeter. Located behind the calorimeter was a steel toroidal magnetic spectrometer for measurement of final state muons produced in the interaction.

Scintillation counter banks were located behind the calorimeter, in the toroidal spectrometer, and behind the toroidal spectrometer. These counters were used to identify muons and select events of interest. Wire spark chambers in the toroidal spectrometer measured the curvature of the muon and thus determined its momentum.

A small PDP 11 computer was used to collect data from the various detectors and transfer this data to magnetic tape for further analysis. The computer also monitored the performance of the apparatus and provided analysis of some of the data as it was collected.

It is useful to consider each aspect of the apparatus in detail. Since this thesis is concerned only with the calorimetry aspects of the experiment, the toroid spectrometer will not be discussed. The interested reader is referred to references 14 and 24.

A. Beam

The beam was first accelerated to 400 GeV in the main ring, then extracted and delivered to the experimental areas, shown in figure 4. This experiment used only a small fraction of the total beam available from the accelerator. This small fraction then struck a 30 cm copper target. Secondary particles produced in the target from nuclear interactions with the protons were then transported approximately 1 km downstream to be used for physics purposes in the calorimeter-toroidal spectrometer apparatus located in LAB E. The schematic of this 1 km long beam line is shown in figure 5. Both the charge and momentum of the beam particles could be selected and this was accomplished by the first series of dipoles in the beam.

The total phase space accepted by the beam line downstream of the production target was very small with an angular acceptance of .3 μsteradians and a momentum bite of 1% {44}. The data in this thesis used 400 GeV protons, but some calibration runs were taken at lower energies from 30 to 300 GeV. Some calibration data was also taken at a test run of the accelerator at 450 GeV. Varying the beam energy allowed us a check on the calorimeter linearity.

In addition to normal hadron running, the beam line could be used to produce momentum analyzed muons. To accomplish, this, the beam line was set to some nominal energy less than 400 GeV. Muons from hadrons decaying both before momentum selection and after momentum selection were then transported down the beam line. To help remove undecayed hadrons still left in the beam, six feet of polyethylene was placed in the beam at the last focus before the detector. A reasonable flux of

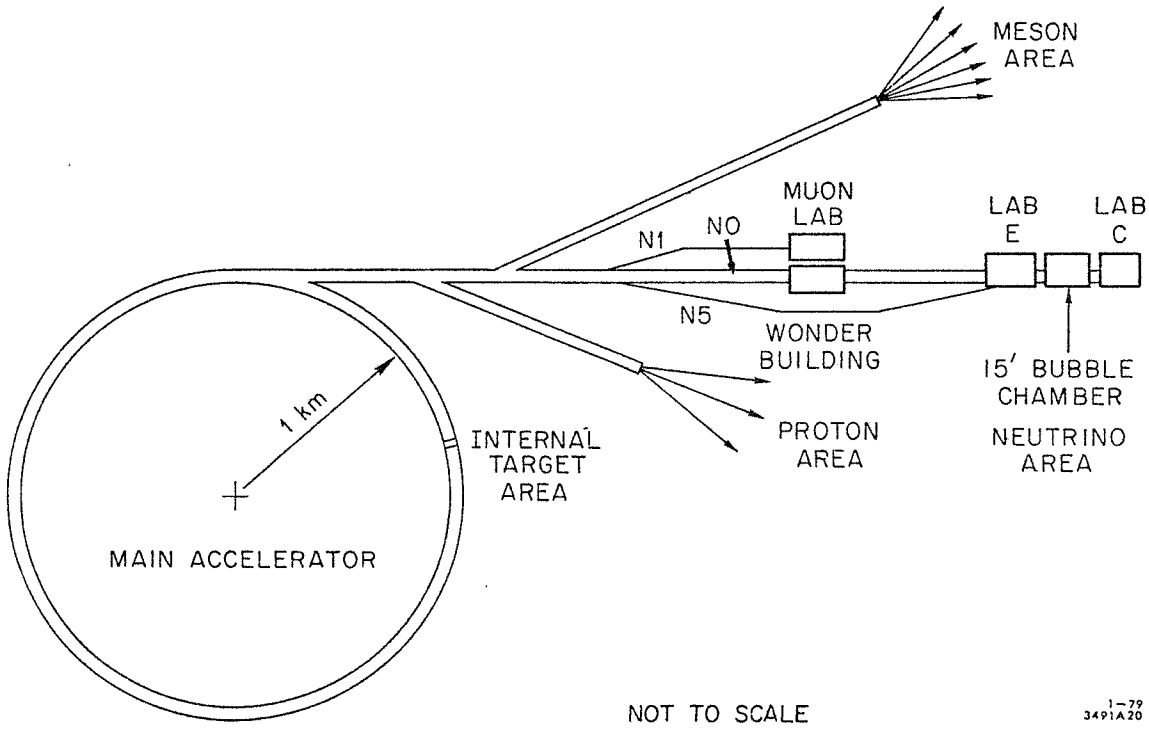

Fig. 4 Fermilab external beam lines and experimental areas. This experiment was performed in LAB E just upstream of the 15' bubble chamber. This figure is not drawn to scale.

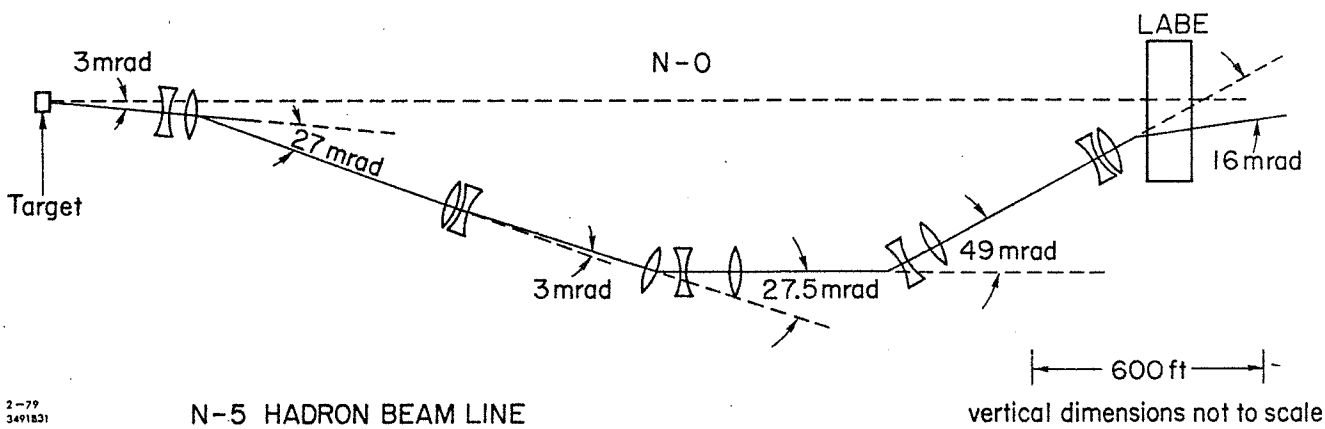

Fig. 5 The hadron beam line to the 15' bubble chamber used in this experiment. The last bend (16 mr) provided momentum information for each proton hitting the detector.

muons was obtained by this method. The best muon/hadron ratio obtained was 30% but typically it was more like 15%.

As a protection against off-momentum particles, the momentum of the incident beam particle was measured for each event by a tagging system upstream of the apparatus. The system consisted of two planes of proportional wire chambers upstream of a magnetic dipole, followed by two more proportional wire chambers downstream. The last chamber was immediately upstream of the target calorimeter and provided interaction vertex information as well as momentum tagging. The chambers measured both the horizontal and vertical portion of the beam with 48 wires in each direction with 1 mm spacing. The dipole magnet consisted of two 20 foot main ring dipoles with a 4 inch horizontal and 2 inch vertical gap. The total bend was 16 mr and provided a momentum resolution of 1%.

B. Calorimeter

The hadron calorimeter consisted of two major sections. The front section of the calorimeter, known affectionately as "MacMurphy" {45}, contained most of the shower. The rear section, known just as affectionately as the "Chief," was primarily for absorbing long showers and identification of muons prior to the toroids. Figure 6 shows a schematic of the calorimeter.

MacMurphy consisted of 45 steel plates 30 inches on a side. These forty-five plates were divided into twenty 1/12 inch thick plates followed by twenty-five 2 inch thick plates. The first 41 plates were each separately mounted on a cylindrical bearing rail along the top support I-beam. By moving these plates in

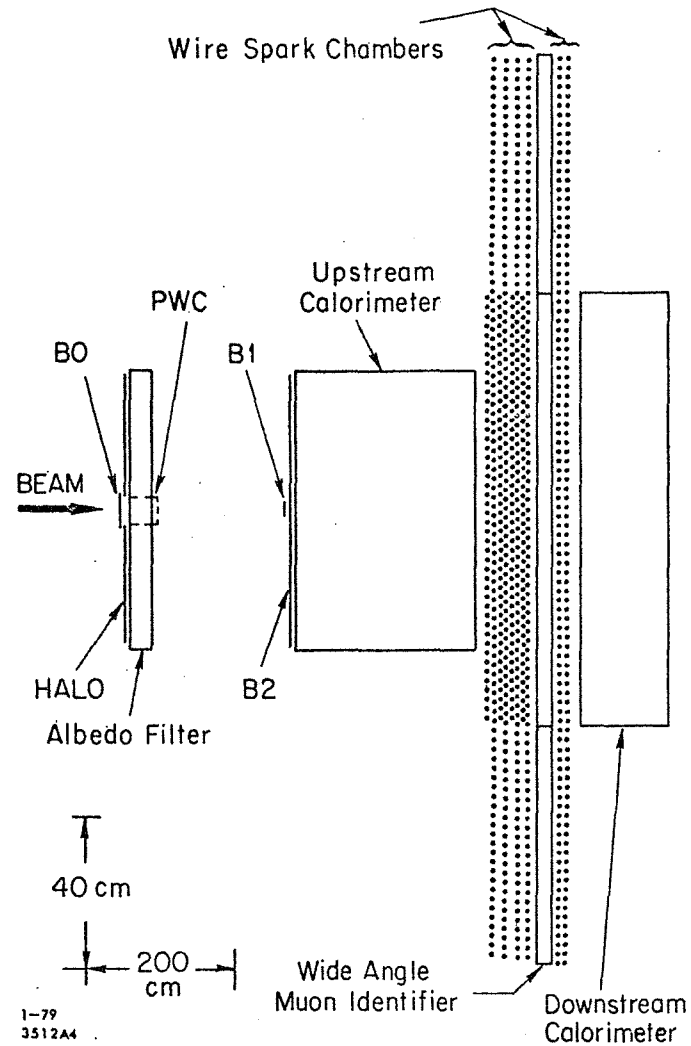

Fig. 6 Upstream portion of the experimental apparatus. The upstream calorimeter is refered to as "MacMurphy" in the text. The downstream calorimeter is the "Chief". B0, B1, B2, and HALO are counters used in the trigger.

the beam direction it was possible to change the mean density of the calorimeter for study of the hadron decay background. For this analysis only the most compacted configuration was used. The last four plates were welded to the support I-beam for structural reasons.

Mounted to the back of each steel plate was a 30 inch x 30 inch x 1/4 inch plastic scintillator with an adiabatic light pipe made from UVT acrylic plastic. Each scintillator was viewed by a RCA 6342A photomultiplier tube. The high voltage base for each photomultiplier contained an amplifier (x40) so that both an amplified (HI) and an unamplified (LO) signal was obtained from each tube. Each counter was also equipped with an LED which could be pulsed both manually or by computer control. The LEDs were used extensively as counter diagnostics and to cross calibrate the unamplified and amplified outputs of each counter.

The phototubes were vertical and alternated top to bottom for every counter. The position of the phototube was left-right asymmetric, with the direction of this asymmetry rotated every other counter. This was done to facilitate close packing of the counters and to remove systematic geometric effects. For precise calorimetry, it was crucial that the response of each counter by uniform across the entire counter. To insure this, each counter was mapped in both the horizontal and vertical directions with a nuclear source. Nonuniformities in the horizontal direction were reduced by systematically degrading the signal in those portions of the light pipe that transported light from segments of the counter showing relatively larger pulse height. This difference was typically less than 10% across the counter. In the vertical direction, a 25% systematic shift was found in the counter

pulse height as one moved the source from the junction of the counter and the light guide to the edge of the counter. It was determined that this effect was due to blue scintillation light being attenuated in the counter and was corrected by placing yellow filters in front of the photocathode.

Portions of the calorimeter had several hundred minimum ionizing particles traversing the counters, and with a several hundred kHz beam rate, this corresponded to large amounts of light impinging on the photocathode. Each phototube was measured to check its gain versus this large rate. These measurements are discussed in Appendix B. It was evident that some tubes experienced significant gain changes as a function of the incident rate. In assigning phototubes to the counters, care was taken to place the tubes most insensitive to rate at shower maximum, with the other tubes further downstream. Also, the direction of the gain changes were alternated as much as possible to partially cancel residual effects.

The gains of the photomultiplier tubes were monitored on an event by event basis and a long term basis by a spark gap light flasher which was viewed by a fiber optic bundle. The fiber optic bundle consisted of 35 separate fiber optic strands, 31 went to the first 31 counters in calorimeter, while 3 more went to phototubes external to the calorimeter and 1 was kept as a spare. The three external phototubes served as a reference for normalization of the spark gap signal. Two of these reference tubes also viewed an Americium source imbedded in a NaI(Tl) crystal. The signal in these tubes from the Amercium acted as an absolute normalization for the phototube gains.

The flasher was triggered once before the beam spill and once after each event taken during the spill. The flasher signals taken before the spill served two purposes. The ratio of the counter signal to reference tube signal for the off-spill flasher triggers, along with the Americium information in the reference tubes, was used to adjust the phototube gains in the off-line analysis for long term gain drifts. In addition, these off-spill ratios served as a calibration for the same ratios calculated from the event flasher triggers taken during the spill. The spill ratios were used in studying beam rate associated effects. The trigger logic for the light flasher system is shown in figure 7. The gate to the flasher ADCs was generated by the coincidence in the reference tubes due to the pulsing of the flasher. Due to hardware difficulties, the actual flashing of the spark gap occurred several tens of μsecs after being triggered. To keep noise voltage from giving spurious gates during this time, the coincidence of the reference tubes was only allowed to occur within a 10 μsec window which opened after an 80 μsec wait time.

The "Chief" consisted of ten 4 inch thick steel plates, 48 inches vertically, and 45 inches horizontally. These plates were mounted on an I-beam support structure positioned approximately 58 inches behind MacMurphy. Behind each steel plate were four 1/2 inch x 48 inch x 10 inch plastic scintillator counters which measured the energy deposition. These counters were viewed by Amperex 56 AVP phototubes attached to a lucite light pipe. Each counter had an LED attached to the bottom of the counter for diagnostic purposes. The direction of the phototube was alternated after each plate to avoid systematics due to attenuation in the counters and also for close packing considerations.

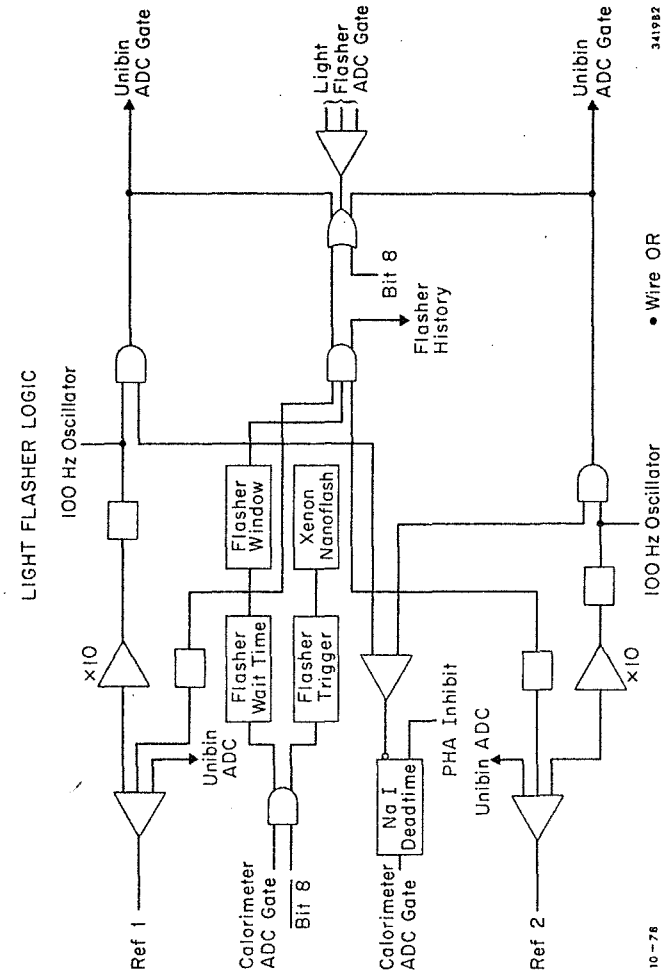

Fig. 7 Trigger logic for pulsing the light flasher and gating the flasher ADCs. BIT 8 refers to a PEDESTAL record discussed in Chapter IV. The flasher is fired on a gate to the ADCs except for PEDESTAL records. The 100 Hz oscillator was used to generate pedestal values in the NaI ADCs.

The main purpose of the Chief was to absorb anomalously long hadron showers. The intensity at the Chief was on the average very low and no provision was made to monitor the gain. The Chief also served to identify muons by penetration of the muon through the forty inches of steel in the Chief. This property was used to eliminate muons from the events of interest which will be discussed in Chapter V.

The electronics involved in the calorimetry measurement is shown in figure 8. Briefly, the LOs for each MacMurphy counter were fanned out through resistive dividers. The 1/4 output from this divider was then ganged together to form a SUPERLO. The SUPERLO was used to calculate the pulse height in a counter when the LO for the counter saturated. This will be discussed in a later chapter. For counters 1-31 the 3/4 output from the resistive divider was fanned out through a d.c. coupled fan out. One of these outputs went into the calorimeter ADCs, the other into the flasher ADCs. For counters 2 through 9, a third output was hardware summed to form the F_2-F_9 requirement for the beam trigger. All ADCs except the flasher ADCs, were then gated by a level from the master trigger module when a trigger was received. The HI outputs (amplified phototube signal) were directly coupled to the ADC through on a.c. coupled fan out.

The signals from the Chief counters were fanned out through an a.c. coupled fan out. One output went directly to the ADCs for pulse height analysis. The other output was added to the three other counters in the appropriate plane to form a total signal for each plane. The plane pulse heights were then added to form a SUPERLO for the Chief counters. The plane pulse heights in planes 6 through 10 were also used in the two muon trigger. Even though the shower particle intensity

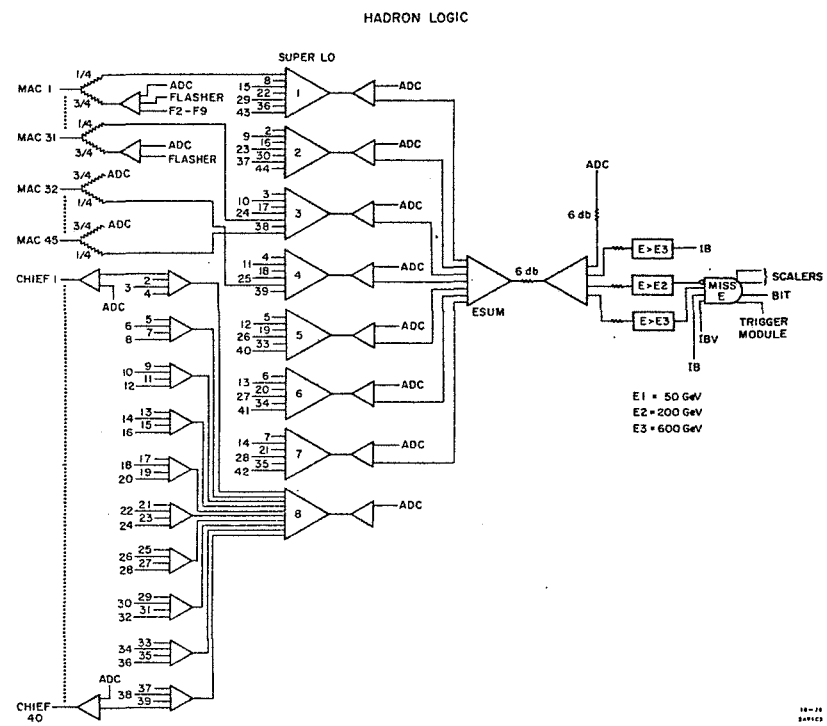

Fig. 8 Electronics used in the calorimeter energy measurement. The triangular figures represent linear adders and provide a total sum of all of the inputs. The outputs labeled SUPERLO are used for counters that saturate their ADCs (see Chapter V).

at the Chief was on the average very small, some affects due to the a.c. coupling were evident in the front few planes of the Chief. Because of this, the a.c. fan outs were replaced with resistive dividers in the second half of the run.

C. Trigger Counters and Logic

A schematic of the apparatus showing the positions of all the trigger counters is shown in figure 9. The counters downstream of the Chief (C, S1, S2, ACR1-3, T2, P1-3, MV, S3, T4) will not be discussed here since they were used only for defining the muon topology for the event. The interested reader is directed to theses of Wyatt Brown and Eric Siskind.

Since any energy measurement ultimately rests on the energy of the incident beam, the beam particle as defined by the trigger counters should be as clean as possible. The initial beam was defined by the upstream trigger counters B0, B1, B2 and HALO shown in figures 6 and 9. B0 was located farthest upstream and just covered the hole in HALO immediately downstream. The dimensions of B0 were 3 inches x 3 inches x 1/16 inch. The thickness was kept to a minimum to reduce background from interactions in the counter. HALO was identical to a MacMurphy counter (30 inch x 30 inch x 1/4 inch) with a 2 1/2 inch x 2 1/2 inch hole in the center to allow passage of the proton beam. HALO was mounted to the upstream side of a steel block to prevent backsplash from the proton interaction in the calorimeter from giving spurious hits in the counter. This "albedo filter" was made from a 30 inch x 30 inch x 12 inch steel block with a 2 1/2 inch x 2 1/2 inch hole in

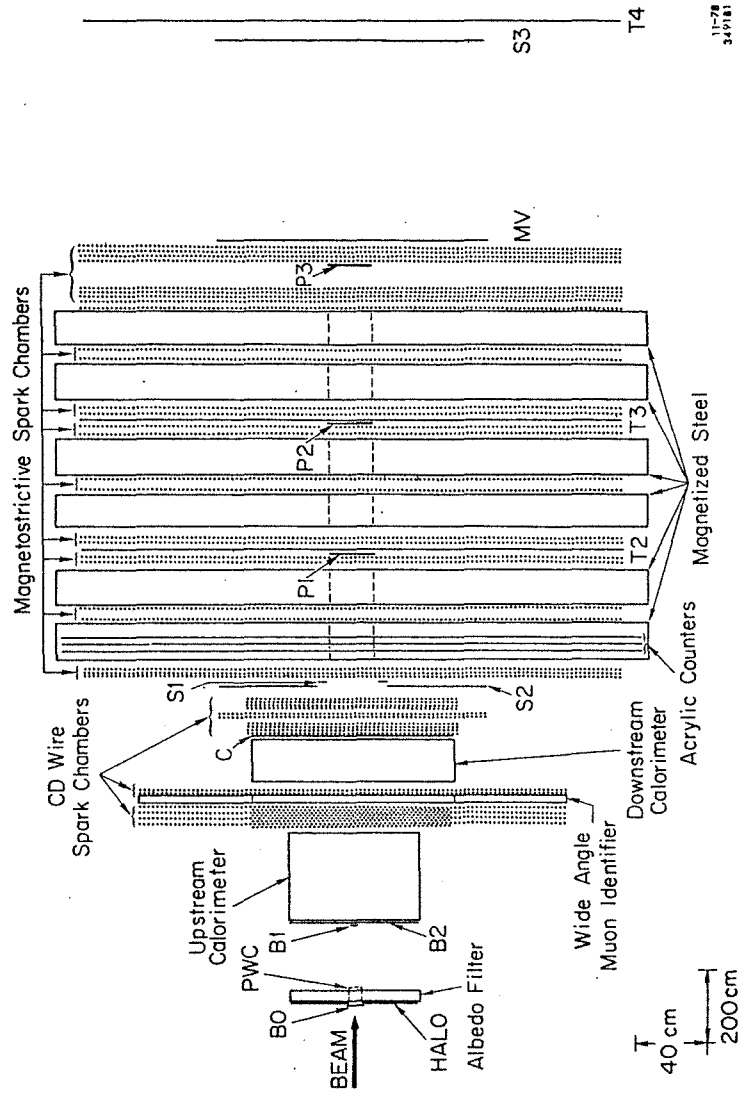

Fig. 9 Schematic of the full apparatus showing positions of all the trigger counters. The downstream toroid spectrometer was used in the muon aspects of the experiment.

the center to exactly match the hole in HALO. Further definition of the beam was given by B1 (2 inch x 2 inch x 1/4 inch) and B2 (30 inch x 30 inch x 1/4 inch). The size of B1 was a good match to the beam envelope at the face of the calorimeter. All of the beam counters were viewed by Amperex 56 AVP phototubes. The outputs from these counters were also pulse height analyzed.

A schematic of the beam logic is shown in figure 10. A primary beam particle trigger was defined as a coincidence between B0, B1, B2 with no hit in HALO. The primary trigger was put in anti-coincidence with $(B0+H)\cdot B2$, called BLOB, delayed by 60 nsecs and advanced by 60 nsecs. These timing coincidences were to insure no additional hits in the calorimeter near the beam particle of interest. As well as this time requirement, the primary beam trigger was also put in anti-coincidence with B0 delayed 95 nsecs (5 r.f. buckets) and advanced 95 nsecs. Again this was to insure that there were no additional beam particles near the beam particle of interest. To be certain that there was only one particle in the triggering r.f. bucket, an added requirement called for the total hardware sum of all the counters (E_{SUM}) be less than 600 GeV. Finally, the trigger demanded that the proton interact within the first eight plates by requiring that the hardware sum of counters 2 through 9 be greater than 270 m.i.p. The final trigger, call IBV, was

$$IBV = B0\cdot B1\cdot B2\cdot\overline{HALO}\cdot BLOB_{DELAYED}\cdot BLOB_{ADVANCED}\cdot BO_{DELAYED}$$
$$\cdot BO_{ADVANCED}\cdot(E_{SUM} < 600\ \text{GeV})\cdot\left(\sum_{i=2}^{9} N_i < 270\ \text{m.i.p.}\right)$$

where N_i is the number of minimum ionizing particles in counter i. IBV was the only trigger requirement for the events used in this analysis. The events with only an IBV trigger were labeled INTERACTING BEAM (I.B.) events.

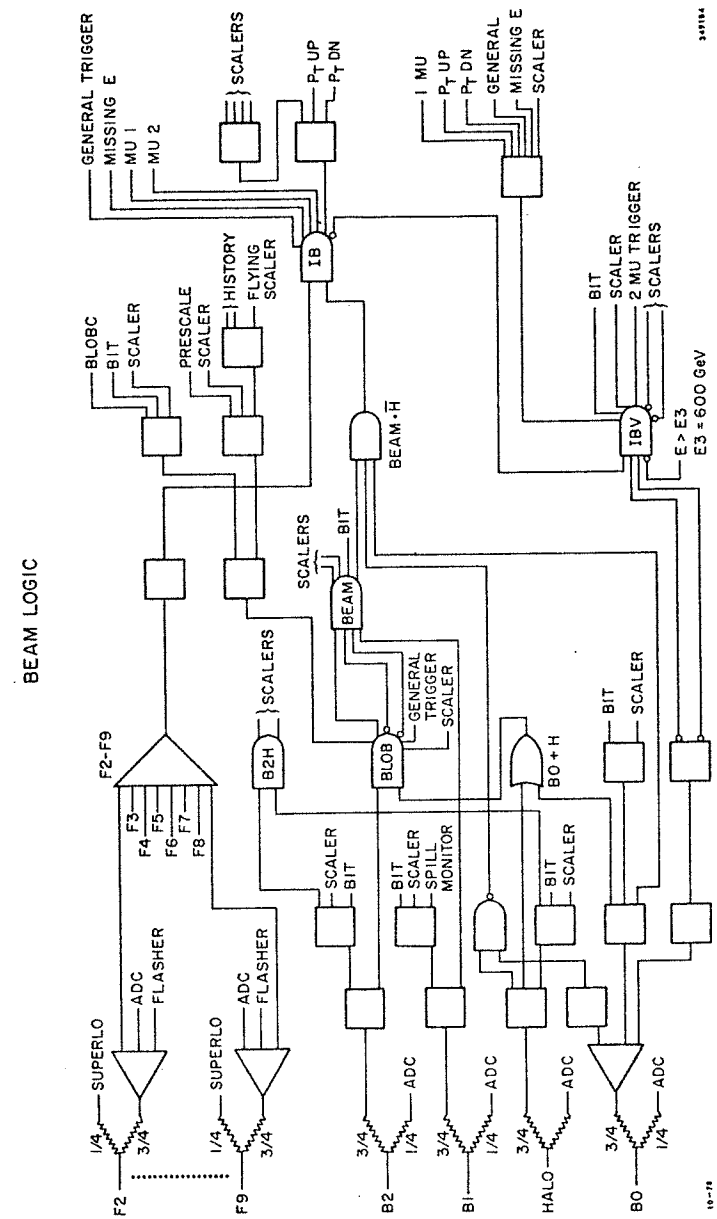

Fig. 10 Trigger logic for INTERACTING BEAM triggers. Not shown are the timing delays discussed in the text.

D. Electronics

Most of the electronics used to process signals in this experiment were fairly standard and do not deserve added comment. However, some of the hardware was of unique design and should be discussed. Further, problems encountered with some of the conventional modules need to be elaborated.

The phototube gain measurements discussed in Appendix B indicated that the large anode currents associated with large beam intensities could severely affect the phototube signal. To correct for these effects in the off-line analysis, it was crucial that one had a measure of the beam intensity during the time the event was taken. To this end, special modules were built to measure the beam intensity before the event. The modules were the EVENT HISTORY, the FLASHER HISTORY, and the FLYING SCALER.

The EVENT HISTORY and FLASHER HISTORY measured the beam intensity on a short time scale. Each module provided a history of the beam on a single r.f. bucket basis up to 192 r.f. buckets (approximately 3 μsecs) before the event. Briefly, these devices were effectively sophisticated shift registers. The input to the shift register was the logical signal BLOB defined previously. This logical signal is simply any particle striking the calorimeter. The clock to this shift register was provided by the r.f. signal of the accelerator. Hits in BLOB registered as 1 at the input and were shifted along by the r.f. Clocking for the EVENT HISTORY was inhibited by an event trigger in the apparatus. This inhibit occurred a fixed time (approximately 10 r.f. buckets) after the trigger decision so that a large spike occurred in

the EVENT HISTORY for the hit associated with the beam particle which gave the trigger. Clocking for the FLASHER HISTORY was inhibited by the reference tube coincidence which generated the gate for the flasher ADCs. This inhibit also occurred a fixed time after the coincidence, but due to an oversight, the flasher gate arrived just off scale of the FLASHER HISTORY for most of the run. This oversight was corrected late in the run by addition of a delay to the inhibit of the FLASHER HISTORY and allowed a determination of the timing. This is only relevant for corrections to the flasher ratio from tails due to beam particles hitting the calorimeter immediately before the flasher fired. Each module was also equipped with internal diagnostic hardware for checking the operation of the module.

A typical EVENT HISTORY distribution is shown in figure 11. One notices immediately the peak due to the trigger particle. In addition, requirements in the trigger requiring no additional beam particles near the event can be seen as voids in the background distribution before and after the trigger particle. This device was most useful in the rate correction to the measured energy. The bit pattern for both of the HISTORYs was written to tape for each event then cleared to continue counting.

The FLYING SCALER consisted of twelve 8 bit scalers and a 16 bit scaler. The 16 bit scaler counted the number of r.f. buckets. The 8 bit scalers counted BLOB. The way the device worked is that certain of these scalers were cleared on specific bit pattern transitions in the r.f. counter. This had the effect that the scalers were cleared periodically. The first four scalers were cleared every 100_8 of the r.f. counter in such a way that scaler 1 was cleared when the lowest

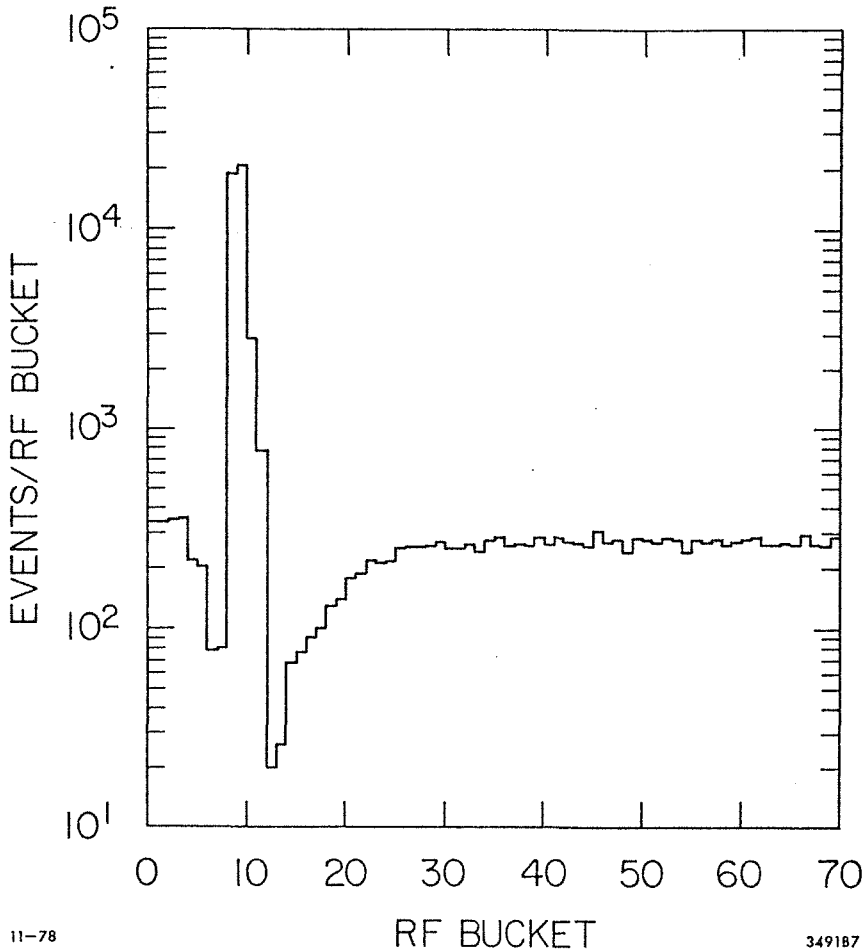

Fig. 11 Typical hit distribution in the EVENT HISTORY. The large peak is the position of the particle which triggered the event. Depletions before and after the triggering particle are due to the time requirements in the beam trigger.

order bits of the r.f. counter obtained the pattern 100_8 and 500_8, scaler 2 on 200_8 and 600_8, etc. The second and third groups of four scalers were cleared on 1000_8 and 10000_8 in a similar fashion to the first four. The r.f. counter and the scalers were inhibited when an event trigger occurred. To determine the last scaler cleared, one checked the bit pattern in the r.f. counter. In this way, one obtained the beam intensity up to 320 μsecs before the event, but even better, the actual time structure of the beam in various increments was also obtained. Since there is some overlap in the counting range of the various grains of the FLYING SCALER, a correction for double counting was made to determine the time structure. The value of the r.f. counter and 12 scaler values were recorded on tape for each event, cleared, and then allowed to continue counting.

The NaI signal was obtained by a hard-wired histogramming module. The histogrammer consisted of 1024 16 bit words of memory. The first half of this memory was used for reference tube 1 (REF 1), the other half for reference tube 2 (REF 2). The histogrammer also contained two ADC units to pulse height analyze the signals from REF 1 and REF 2. The values of the pulse height in the ADCs were transferred to the histogrammer except for the flasher signal. Both ADC values were recorded on tape for each event. The histogrammer memory was also recorded on tape prior to the beam spill and immediately after the beam spill.

The ADC units used for pulse height analysis were standard LeCroy 2249A ADC modules. The units were specified to be linear to within .25% of the number of channels plus or minus 2 channels {46} but a measurement of the linearity indicated significant deviations. A

correction for this nonlinearity was made in the analysis. The actual charge, Q, deposited in the ADC was derived from the channel count in the ADC from the relation

$$Q = KC^{\alpha}$$

where C is the channel number and K and α are constants. α ranged from 1.00 to about 1.08 depending on the ADC channel. Unfortunately, only the first one hundred and forty-four channels of the ADCs were measured. This means that the flasher ADCs were not corrected according to the above formula. The linearity of the flasher ADCs had to be determined separately from the low intensity INTERACTING BEAM running.

E. Data Collection

A DEC PDP 11/45 computer was used to collect the data for each event and transfer this data to magnetic tape. In addition to these collection functions, the computer also acted as a monitor of the equipment performing several tests during the data collection to insure the quality of the data. Most of the data was transferred to the computer using standard CAMAC hardware to interface to the experimental equipment. The CAMAC system was then interfaced to the PDP 11 by KINETIC SYSTEMS CAMAC interface. The NaI hardwired histogrammer was attached directly to the PDP 11 UNIBUS. These devices were read directly into the computer via DMA transfer.

As mentioned previously, the computer monitored all phases of the experiment. The pedestal values for each ADC channel and the values for these ADCs when the LEDs for each counter were pulsed were monitored

before each beam spill during the entire run and a message was printed out at the terminal if they were outside windows set by the experimenter. The FLYING SCALER was continuously checked for reasonable counting rates by calculating the beam intensity from the scaler counts. The computer also performed diagnostics on the spark chambers such as checking fiducial values, spark bank overflow, spark chamber efficiency, etc. Probably the single most useful diagnostic was the single event display on the graphics terminal. Problems became very obvious by simply looking at a few events on this display. The histogramming capabilities of the on-line program were almost limitless. Flexible conditions on the histogramming allowed one to study any experimental parameter under any condition. This allowed for a close watch to be kept on the apparatus and insured the integrity of the data. This program, a version of MULTI (Multi-task system) written and subsequently adapted for this experiment by J.F. Bartlett, contributed greatly to the success of the experiment.

CHAPTER IV

Data Taking Procedures

A. Normal Running

Several different types of data records were taken during the course of the experiment. At the beginning of a data run a data record was written to tape denoting the start of a run. These BEGIN RUN records contained pertinent information about the run such as magnet current, purpose of the run, etc. Prior to each beam spill three additional types of records were taken. The first of these recorded the ADC values without any particles striking the counters. These PEDESTAL records were used to determine the charge associated with each ADC due simply to the gating of the ADC. This has to be subtracted from the ADC measurement to determine the ADC signal for real energy deposition in the counters. The second of these pre-spill records recorded the ADC values after the LEDs in each counter were pulsed. These LED records were used to check that each phototube was operating correctly. The light flasher was also fired and the corresponding ADC values recorded on the pre-spill LED records for use in flasher studies without complications from beam particles in the calorimeter. The last record, the BEGIN SPILL record, wrote the NaI hardware histogram information to tape for later analysis. During the beam spill both events with muon triggers and INTERACTING BEAM triggers were taken. The INTERACTING BEAM events (I.B.) were normal interacting protons without any muon requirement whatsoever. The only requirement for this trigger was a good beam particle as defined

in the previous chapter. Because this logical combination occurred very often, not every proton satisfying this requirement was accepted. Only after a preset number of logical signals was a trigger accepted. This prescaling had the effect of distributing the INTERACTING BEAM triggers randomly in the spill. This helps avoid systematic effects which could occur if the INTERACTING BEAM events were associated with a given time in the spill. One final record was written after the beam spill. These END SPILL records contained additional NaI histogrammer information and the values of all of the scalers which counted during the spill.

B. I.B. Runs

As well as the I.B. events taken during the normal running, a few runs were taken with only I.B. triggers. During these runs all of the muon triggers were turned off and the prescaler on the logical I.B. signal was set to 0 so that every I.B. coincidence generated an event. These runs were taken at a very low beam intensity, typically 1-5 x 10^3 protons per pulse. The low intensity kept any adverse rate effects on the calorimetry to a minimum. This allowed one to study the calorimeter response without the added complications due to gain shifts in the phototubes. This low intensity data also served as a check on the quality of the rate correction applied to the main body of data.

C. Muon Runs

To calibrate the calorimetry counters and to also align the spark chambers, several runs were taken with a muon beam. The muon running

was divided into two parts. The first involved strict alignment of the chambers. The alignment data was useful for calibrating the Chief counters, but could not be used for the MacMurphy counters because of spark chamber noise problems in the HI ADCs. The second part of the muon running involved turning off the spark chambers and running only calorimeter calibration data. This data was used for calibration of both the MacMurphy and Chief counters.

CHAPTER V

Data Analysis

The final data sample from this experiment consisted of 50 magnetic tapes and 15 trillion data bits. The purpose of this analysis is to convert this collection of ones and zeros into some meaningful form. The first stage of the analysis consisted of selecting the I.B. events out of the total sample by using the trigger bit pattern written on tape for each event. The second procedure involved correction to the ADC for nonlinearity, calibration of the calorimeter, then finally conversion of the calorimeter response to an energy. The last procedure was to improve the energy measurement by judicious use of cuts on the data. After all of these procedures the best possible energy measurement was obtained. Any neutrino production could then be searched for in this energy distribution.

A. ADC Response

Conversion of the number of counts in the ADC to energy deposited in the scintillator involved several steps. The first step involved subtracting the pedestal value for each ADC from the ADC value written on tape. This pedestal value was determined from the PEDESTAL event taken before each spill. After subtraction of the pedestal, all of the calorimeter ADCs were corrected for nonlinearity using the coefficient determined for each ADC. As mentioned in Chapter III, this correction is of the form

$$C' = C^{\alpha}$$

where C' is the corrected channel number, C the actual channel number

and α varies from 1 to 1.08 depending on the ADC. All subsequent analysis was done with the corrected channel number.

The SUPERLOs mentioned in Chapter III were used to obtain the pulse height in those counters which saturated their ADCs. This pulse height was obtained using the relation

$$C_i^{'sat} = (C'_{SUPERLO_k} - \sum_{j \neq i}^{N_k} a_j C'_j) / a_i$$

where $C_i^{'sat}$ is the real number of channels in the saturating counter i, $C'_{SUPERLO_k}$ is the number of channels in the SUPERLO which contains counter i, a_i is the fraction of the pulse height in counter i which contributes to $SUPERLO_k$ (i.e. a_i times the number of counts in the ADC for counter i equals the contribution in counts for counter i to the ADC for $SUPERLO_k$), C'_j is the number of channels in the non-saturating counters in $SUPERLO_k$, and N_k is the number of counters comprising the SUPERLO. The sum in the above expression is over all of the nonsaturating counters in $SUPERLO_k$. If more than one counter is saturated in a given SUPERLO, then the excess in the SUPERLO beyond the sum of the nonsaturating component is divided equally among the saturating counters.

B. Calorimeter

For calorimetry techniques as discussed in Appendix A to work effectively, the number of charged particles at various depths in the calorimeter must be counted correctly. Since the response of a counter to a minimum ionizing particle (m.i.p.) varied, this number had to be determined individually for each counter. This relative calibration was accomplished by three different methods:

(1) using muons as single m.i.p.s

(2) requiring consistency in the shower profile for different positions of the first interaction

(3) minimization of the total resolution

Finally, after obtaining the relative calibration for each counter, the total calorimeter response could be converted to an energy in GeV by using a momentum analyzed incident beam.

Each method of calibration will now be considered in detail.

1. Muon Calibration

Muons are ideally suited for the purpose of calibrating the calorimeter counters relative to each other. Muons can penetrate large amounts of matter without interacting. Thus, a moderate energy muon, say 50 GeV, can penetrate the whole calorimeter easily. By measuring the pulse height in each counter for this muon a simultaneous measure of a single m.i.p. in each counter for the same particle is obtained. This is exactly the relative calibration necessary for good calorimetry.

The amplified outputs (HIs) from the phototubes were used for the muon calibration. A typical muon pulse height distribution in the HIs is shown in figure 12. One notices immediately the prominent Landau tail on this distribution. The best measure of a muon from this distribution is the mean, but because of the tail, the mean is susceptible to statistical fluctuations. To circumvent this problem it is useful to use the mean of the distribution cut at .25 and 2.5 times the mean of the distribution. This value was calculated iteratively. A cut at 2.5 times the mean was used to eliminate effects of the long tail. The cut

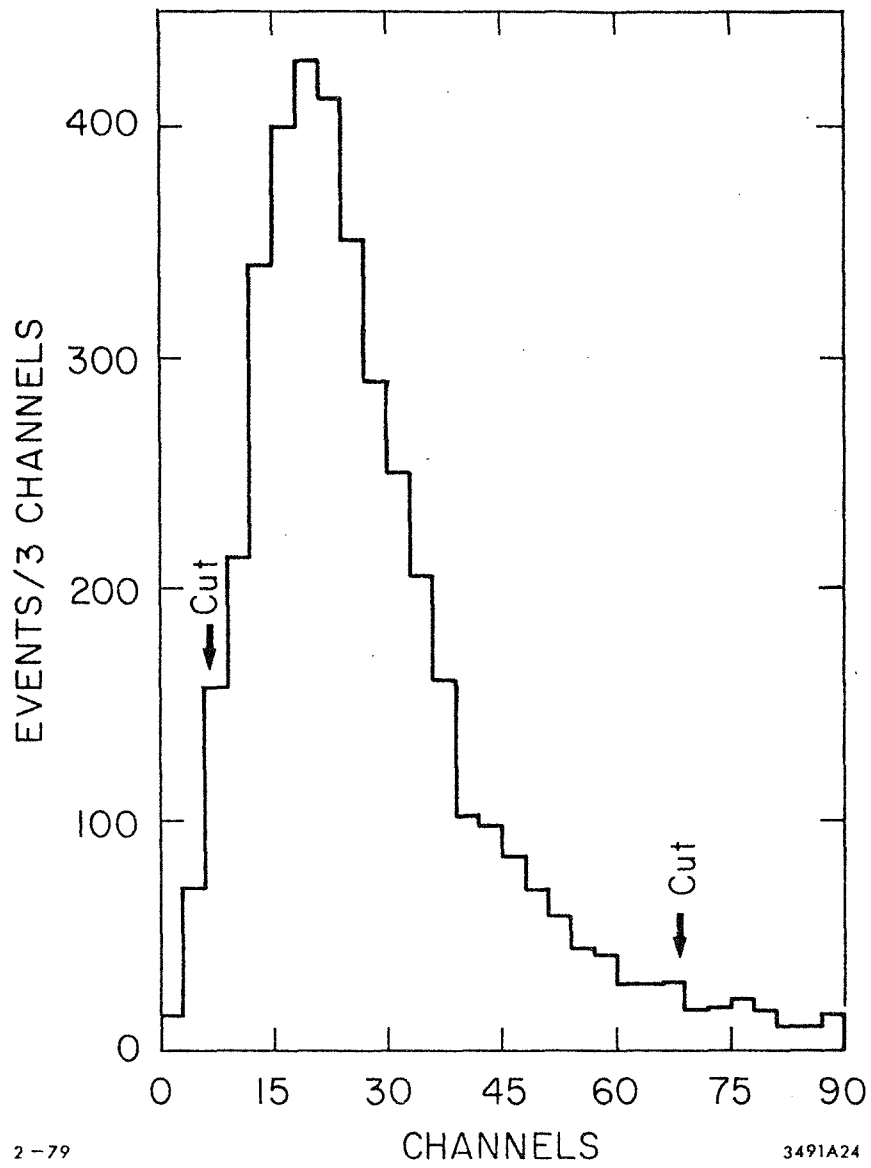

Fig. 12 Typical muon pulse height distribution in the HIs. The arrows indicate the position of the cuts applied in calculating the m.i.p. response for each counter.

at .25 times the mean was to ensure that the distribution was adequately above pedestal and that there was no contribution from width in the pedestal. This procedure was done for each counter and subsequently yielded the m.i.p. value for that counter.

Since it is the unamplified output (LO) which is used in the calorimetry, one must determine the LO calibration from the muon values in the HIs. This required measuring the amplifier gain, i.e. the HI/LO ratio, for each counter. This was accomplished in two ways. The first method used the LEDs that were mounted in each counter. The driving unit that fired these LEDs had a variable amplitude feature. The LEDs were pulsed and the amplitudes changed. A straight line fit to a plot of HI versus LO for different LED amplitudes yielded the HI/LO ratio. The second method used the muon pulse height itself. The events on the Landau tail were used to plot HI versus LO. A straight line fit to the plot of HI versus LO again yielded the HI/LO ratio. The muon method had an advantage over the LEDs since the frequency spectrum of the light emitted by the counter from muons was the same as from the particles traversing the counter during a shower, whereas the LED frequency spectrum might have been significantly different. This is an important consideration for amplifiers with a finite band width. There was an approximately 10% systematic difference in these two methods for the HI/LO ratio.

Although the muon calibration is an unbiased measure of the calorimeter calibration, it was not completely adequate for two reasons. First, the small overlap between the HIs and LOs caused large errors in the HI/LO ratio and limited effectiveness of the method. Secondly, there was an indication that the pion flux associated with the muons

was creating adverse effects on the measurement. Recall that the HIs are a.c. coupled to the ADC units. At a large pion rate this a.c. coupling could cause pedestal shifting in the ADC units due to build up of charge on the coupling capacitors. For these reasons, the muon calibration values were adjusted using the shower calibration method described in the next section.

2. Shower Calibration

This calibration method relies on the fact that on the average, the shower profile should be independent of the position of the first interaction. Therefore, the profile for showers that begin in plate 2 should be the same as for showers beginning in plate 1, except shifted downstream by the thickness of one plate. Those showers beginning in plate 3 would be shifted by a thickness of two plates, etc. From a consistency requirement between these various shower positions, the forty-five calibration constants corresponding to a single m.i.p. for each counter are obtained by minimizing the χ^2 from comparison of these showers.

For this method one needs to define an algorithm for determining the beginning of the shower. By the very nature of the method, the calibration is sensitive to the actual details of the algorithm. In general, the beginning of the shower is found by searching for a positive gradient in the pulse height distribution of the calorimetry counters. If we call i_{BEG} the plate in which the shower starts, then the positive slope implies

$$N_{i_{BEG}} > N_1 \ , \ N_{i_{BEG}+1} > N_2 \ , \ N_{i_{BEG}+2} > N_3$$

where N_i is the number of m.i.p. in the counter behind plate i and $N_1 \geq N_2 \geq N_3$. For reasonable values of N_1, N_2, and N_3, i_{BEG} is unambiguously defined for fast rising showers. Very slow rising showers however, can be confused with other showers which have a large backsplash ("albedo") from the primary interaction which occurred further downstream. The algorithm used in this calibration technique used $N_1 = N_2 = 5$ m.i.p. and $N_3 = 10$ m.i.p. as defined by the muon calibration above.

The χ^2 obtained from comparing the profiles for showers at various depths is

$$\chi^2 = \sum_{i=1}^{7} \sum_{j=i+1}^{8} \sum_{k=1}^{45} \left\{ \frac{C_k N_{i,k} - C_{k-i+j} N_{j,k-i+j}}{\{C_k^2 \sigma_{i,k}^2 + C_{k-i+j}^2 \sigma_{j,k-i+j}^2\}^{\frac{1}{2}}} \right\}^2$$

where $N_{i,k}$ is the number of m.i.p. in counter k for showers starting in plate i as determined from the muon calibration; $\sigma_{i,k}$ is the error in $N_{i,k}$, and C_k is the yet undetermined calibration constant for counter k. One notices immediately that the χ^2 above is left invariant if each C_k is multiplied by some fraction f. To remove this ambiguity, an additional constraint was imposed requiring that the sum of the new calibration constants be equal to the sum of the muon calibration constants ($C_k^{MUON} = 1$)

$$\sum_{i=1}^{45} C_i = 45$$

This can be added to the above χ^2 using a Lagrange multiplier λ to obtain

$$\chi^2 = \sum_{i=1}^{7} \sum_{j=i+1}^{8} \sum_{k=1}^{45} \left\{ \frac{C_k N_{i,k} - C_{k-i+j} N_{j,k-i+j}}{\{C_k^2 \sigma_{i,k}^2 + C_{k-i+j}^2 \sigma_{j,k-i+j}^2\}^{\frac{1}{2}}} \right\}^2 + \lambda \sum_{k=1}^{45} (C_k - 1)$$

Realizing that C_k will be only slightly different from the muon value, C_k can be expanded about the muon value

$$C_k = 1 + \delta_k$$

Expanding the quantity in χ^2 above, keeping only terms to first order in δ_k, the following is obtained

$$\chi^2 = \sum_{i=1}^{7} \sum_{j=i+1}^{8} \sum_{k=1}^{45} \frac{d^2_{i,j,k}}{e_{i,j,k}} \left\{ 1 + \delta_k \left[\frac{N_{i,k}}{d_{i,j,k}} - \frac{\sigma^2_{i,k}}{e_{i,j,k}} \right] - \delta_{k-i+j} \left[\frac{N_{j,k-i+j}}{d_{i,j,k}} + \frac{\sigma^2_{j,k-i+j}}{e_{i,j,k}} \right] \right\}^2 + \lambda \sum_{k=1}^{45} \delta_k$$

where

$$d_{i,j,k} = N_{i,k} - N_{j,k-i+j}$$

$$e_{i,j,k} = \sigma^2_{i,k} + \sigma^2_{j,k-i+j}$$

To obtain the minimum value of δ_k, χ^2 is differentiated with respect to δ_k and the resultant is set equal to 0

$$0 = \frac{\partial \chi^2}{\partial \delta_1} = \sum_{i=1}^{7} \sum_{j=i+1}^{8} 2 \frac{d^2_{i,j,l}}{e_{i,j,l}} \left\{ 1 + \delta_1 \left[\frac{N_{i,l}}{d_{i,j,l}} - \frac{\sigma^2_{i,l}}{e_{i,j,l}} \right] - \delta_{1-i+j} \left[\frac{N_{j,l-i+j}}{d_{i,j,l}} + \frac{\sigma^2_{j,l-i+j}}{e_{i,j,l}} \right] \right\} \left[\frac{N_{i,l}}{d_{i,j,l}} - \frac{\sigma^2_{i,l}}{e_{i,j,l}} \right]$$

$$-2 \frac{d^2_{i,j,l-j+i}}{e_{i,j,l-j+i}} \left\{ 1 + \delta_{1-j+i} \left[\frac{N_{i,l-j+i}}{d_{i,j,l-j+i}} - \frac{\sigma^2_{i,l-j+i}}{e_{i,j,l-j+i}} \right] - \delta_1 \left[\frac{N_{j,l}}{d_{i,j,l-j+i}} + \frac{\sigma^2_{j,l}}{e_{i,j,l-j+i}} \right] \right\} \left[\frac{N_{j,l}}{d_{i,j,l-j+i}} + \frac{\sigma^2_{j,l}}{e_{i,j,l-j+i}} \right] + \lambda$$

By solving the set of 46 linear equations (45 δ_ks and the Langrange multiplier λ), the 45 calibration constants are obtained. One can redefine δ_k, $N_{i,k}$, and $\sigma_{i,k}$ using these new calibration constants and redo the calculation again until a convergent solution is found. As advertised, these constants differed only slightly from the muon calibration constants. To estimate how well the shower calibration performed in measuring the energy, the final resolution was compared to the resolution obtained from the minimization of the resolution which will be discussed in the next section.

3. Minimization of the Resolution

In this technique one optimizes the calibration constants consistent with a minimum resolution for the apparatus. This method yielded the smallest resolution possible and gave a good check of the other calibration methods.

The error in the measured energy is

$$(N-1)\sigma^2 = \sum_{i=1}^{N} (E_i - \bar{E})^2 = \sum_{i=1}^{N} \left(\sum_{j=1}^{45} C_j d_j N^i_j - \bar{E} \right)^2$$

where N^i_j is the number of m.i.p. in counter j from the muon calibration for event i; d_j is the thickness of plate j; and C_j is the undetermined calibration constant; $\bar{E}$ is the average energy and N is the number of events in the data sample. Clearly,

$$\bar{E} = \frac{1}{N} \sum_{i=1}^{N} \sum_{j=1}^{45} C_j d_j N^i_j$$

Again, an additional constraint must be added to the χ^2 for optimization. The χ^2 is constrained by requiring that the average energy does not

change with a change in C_j from the muon value

$$\overline{E}_{MUON} = \frac{1}{N} \sum_{i=1}^{N} \sum_{j=1}^{45} d_j N_j^i = \frac{1}{N} \sum_{i=1}^{N} \sum_{j=1}^{45} C_j d_j N_j^i = \overline{E}$$

Differentiating σ^2 with respect to C_j and setting the result to 0 the equation

$$0 = \frac{\partial \sigma^2}{\partial C_l} = 2 \sum_{i=1}^{N} \left(\sum_{j=1}^{45} C_j d_j N_j^i - \overline{E} \right) d_l N_l^i$$

$$= \sum_{j=1}^{45} C_j d_j d_l \sum_{i=1}^{N} N_j^i N_l^i - \overline{E}\, d_l \sum_{i=1}^{N} N_l^i$$

Solving this set of equations yields the 45 calibration constants.

With infinite statistics, this minimization technique would be the best way to calibrate the calorimeter. However, the statistics are not infinite and the statistical accuracy limited the results of this method. Because the experiment was only optimizing with respect to the resolution, there arose correlations between the calibration coefficients to reduce the resolution which gave nonreasonable solutions for the constants. Because of these problems the minimization method was only used as a check on the other methods.

4. Weighting

As is mentioned in Appendix A, the response of the calorimeter is different for electromagnetic energy deposition and hadronic energy deposition. The electromagnetic shower initiated by an electron or a photon will have a characteristic length governed by the radiation length in the steel of the calorimeter, approximately 1.77 cm. That is to say, all of the energy associated with an electromagnetic cascade

will be deposited in a few radiation lengths. Hadronic showers, on the other hand, have a characteristic length equal to the absorption length of the calorimeter, approximately 17.1 cm, an order of magnitude larger. Also, the total measured energy in an electromagnetic shower is larger than a hadronic shower since the electromagnetic shower will not lose energy to the unsampled nuclear sector. The response of the calorimeter for electromagnetic energy deposition would then be fairly short showers with large pulse heights, while hadronic showers would be longer with reduced pulse height. In addition, the resolution is better for electromagnetic cascades because there is no width usually associated with energy lost to the unmeasured nuclear sector.

Because of these differing responses to electromagnetic and hadronic energy, the measured energy will be sensitive to fluctuations in the π^o content in the primary hadronic shower. Since the π^o decays almost instantaneously into two photons, showers with a large π^o content will have most of the beam energy deposited as electromagnetic showers, being fairly short and with large pulse heights. This effect in the data can be studied by investigating the dependence of the total energy and resolution on the second moment of the distribution η, where η is defined as

$$\eta = \left(\sum_{i=1}^{45} N_i^2 \right)^{\frac{1}{2}} / \sum_{i=1}^{45} N_i \, .$$

N_i is the number of m.i.p. particles in counter i. For a uniform distribution, η is .149. For a triangular distribution over five counters, η is .48. The η distribution for an I.B. run is shown in figure 13. The dependence of the calorimetry parameters on the second moment is shown in figure 14. Increasing energy and improving resolution

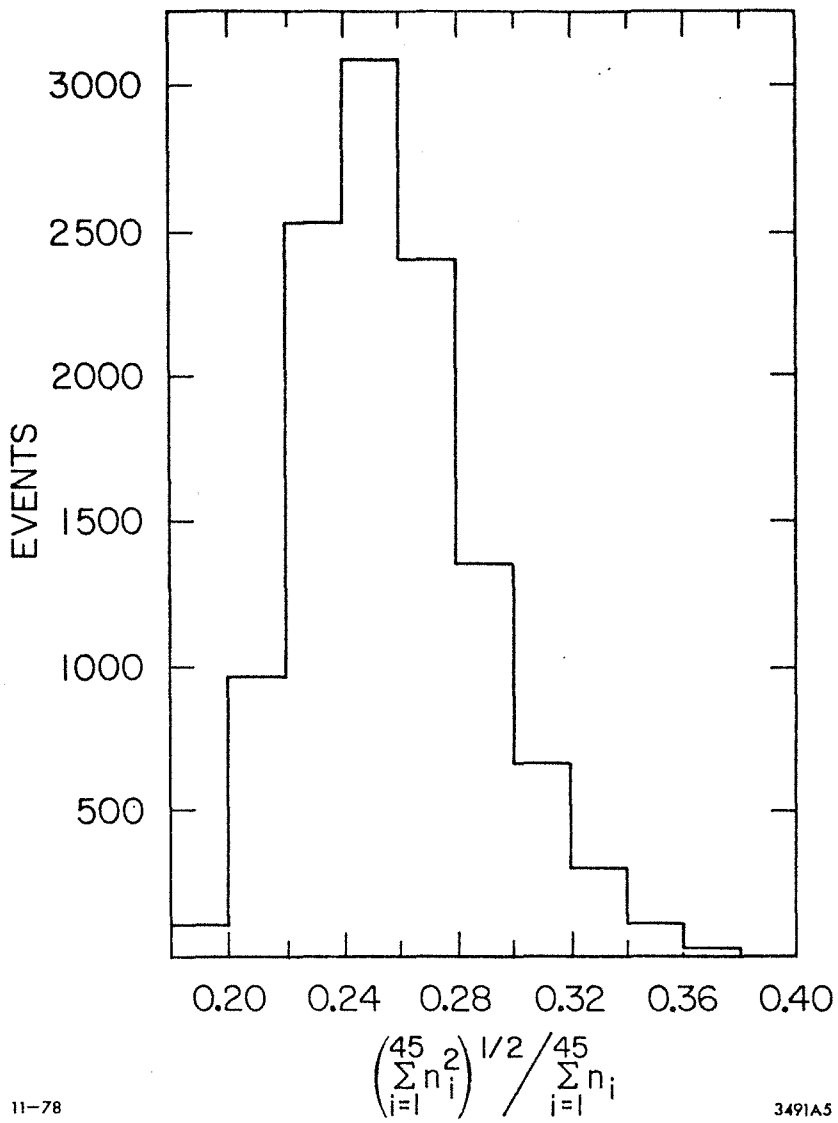

Fig. 13 The shower profile second moment distribution for an I.B. run. n_i is the number of m.i.p. in counter i.

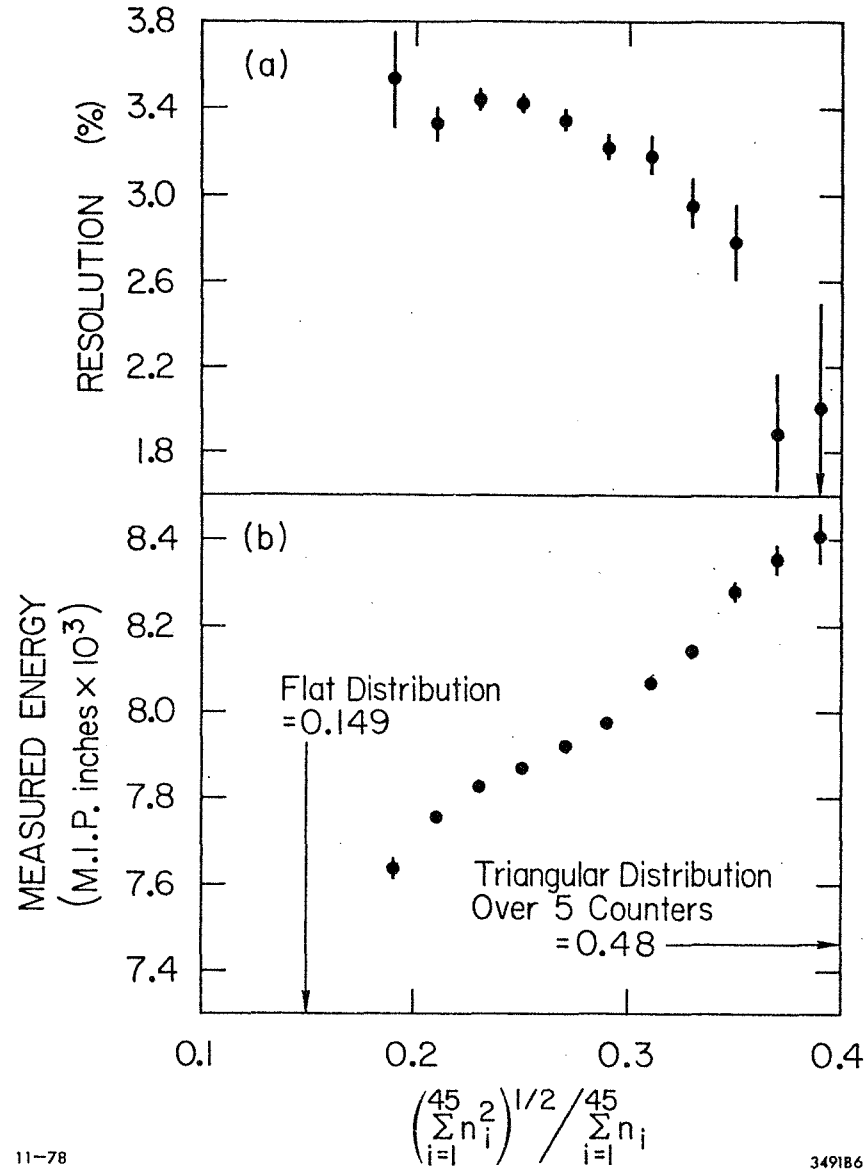

Fig. 14 Dependence of the calorimeter parameters on the second moment of the shower profile. The value of the second moment for two possible distributions is indicated. The measured energy conversion from m.i.p.-inches to Gev is .05039.

for an increase in the second moment is indicative of a larger π^0 component.

To mitigate the second moment effects described above, a weighted pulse height was used in calculating the measured energy. The weighting function was taken to be of the form

$$w_i = 1 - xf(N_i)$$

where x is some fraction of the function $f(N_i)$ to be determined empirically and w_i is the weight for counter i. The measured energy is then

$$E = \frac{K \sum_{i=1}^{45} w_i d_i N_i}{\sum_{i=1}^{45} w_i}$$

where d_i is again the thickness of plate i and K is a normalization to insure that the average weighted energy is equal to the average unweighted energy. Several functions were tried for $f(N_i)$. Figure 15 shows the energy and resolution of the calorimeter as a function of the fraction x for a linear form of $f(N_i)$

$$f(N_i) \propto N_i$$

A clear minimum in the resolution is apparent. All of the forms studied for $f(N_i)$ gave a minimum in the resolution. The final form of $f(N_i)$ used was the linear function

$$f(N_i) = N_i/1500.$$

Noting that the minimum occurs at x = .2, one obtains the final weighting factor

$$w_i = 1 - 1.34\text{x}10^{-4}\ N_i$$

For measured energies less than 400 GeV, the weighting factor was given an additional energy dependence

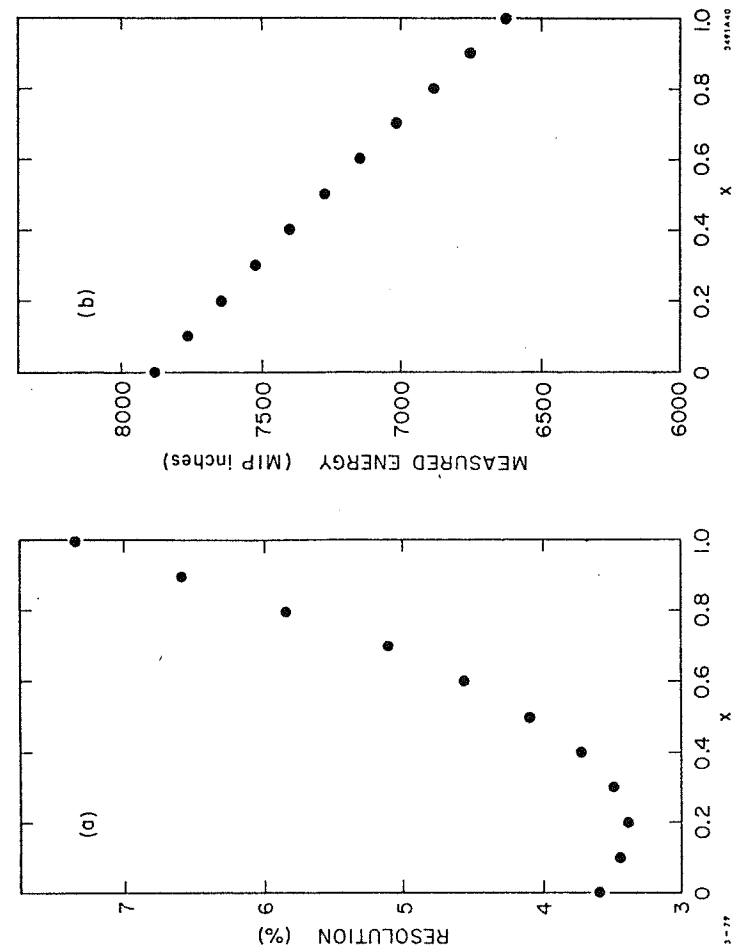

Fig. 15 Dependence of the calorimeter parameters on the weighting fraction x as described in the text.

$$w_i = 1 - 1.34\times10^{-4}\ N_i/(E_{MEAS}/400).$$

where E_{MEAS} is the unweighted measured energy in GeV. E_{MEAS} was used rather than the beam energy to avoid systematic effects for events with a large amount of missing energy. A logarithmic plot of the measured energy after weighting is shown in figure 16. There does not appear to be any nonGaussian behavior in the measured energy. To reinforce this point, the same distribution is shown in a probability plot in figure 17. This distribution is linear, indicative of a Gaussian character.

The response and resolution of the calorimeter using the weighted energy are shown in figures 18 and 19. A fit to the form $A + BE_{BEAM}$ for the weighted energy yields A=2.5±.3 GeV, B=1.003±.004 with a χ^2 of .34 per 5 degrees of freedom. A similar fit to the unweighted energy yields A=1.18±.27 GeV, B=1.003±.004 with a χ^2 of 2.8 for 5 degrees of freedom. The negative offset may arise from slight pedestal shifts during the spill. Also, there seems to be a small systematic (1-4% increasing with decreasing energy) shift in the weighted energy. This shift may be due to a miscalculation in the implicit energy scaling in the weighting formula. Taking into account this negative offset, a fit to the weighted energy of the form AE_{BEAM}^{B} for the resolution yields values of 71.3±1.8% and -.510±.005 for A and B respectively, with a χ^2 of 27 for 5 degrees of freedom. A similar fit to the unweighted energy yields A=64.3±1.6%, B=-.484±.005, with a χ^2 of 19 for 5 degrees of freedom. The χ^2 for the weighted energy gets a large contribution from the low energy points where the weighting scheme may be losing its effectiveness. Fitting only from 100 to 450 GeV yields A=61.4±3.4% and B=-.484±.010 with a χ^2 of 8.7 for 3 degrees of freedom.

In conclusion, the weighted energy appears to be a good measure of the calorimeter performance at large energies. Degradation effects begin to appear at the lower energies. The calibration methods and the resolutions obtained from these measurements are shown in Table II.

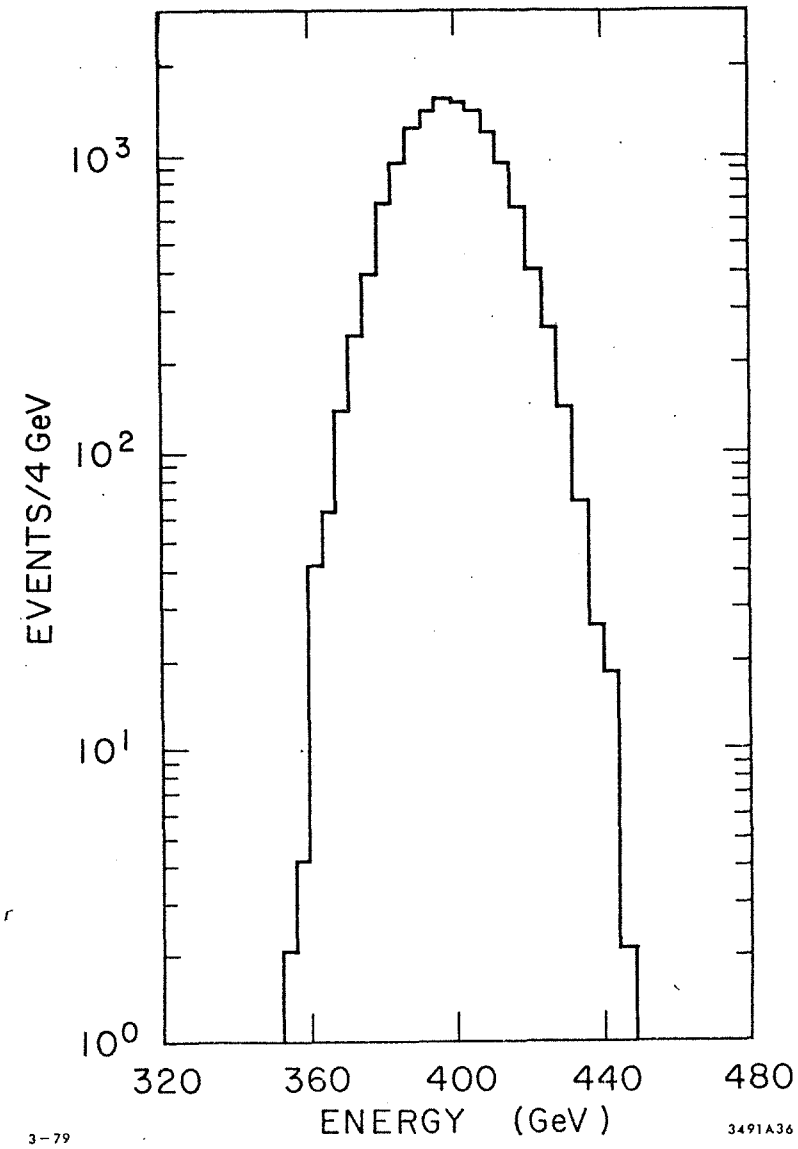

Fig. 16 Calorimeter response after weighting. This distribution has been cut to eliminate tails associated with calorimeter systematics as discussed later in the text.

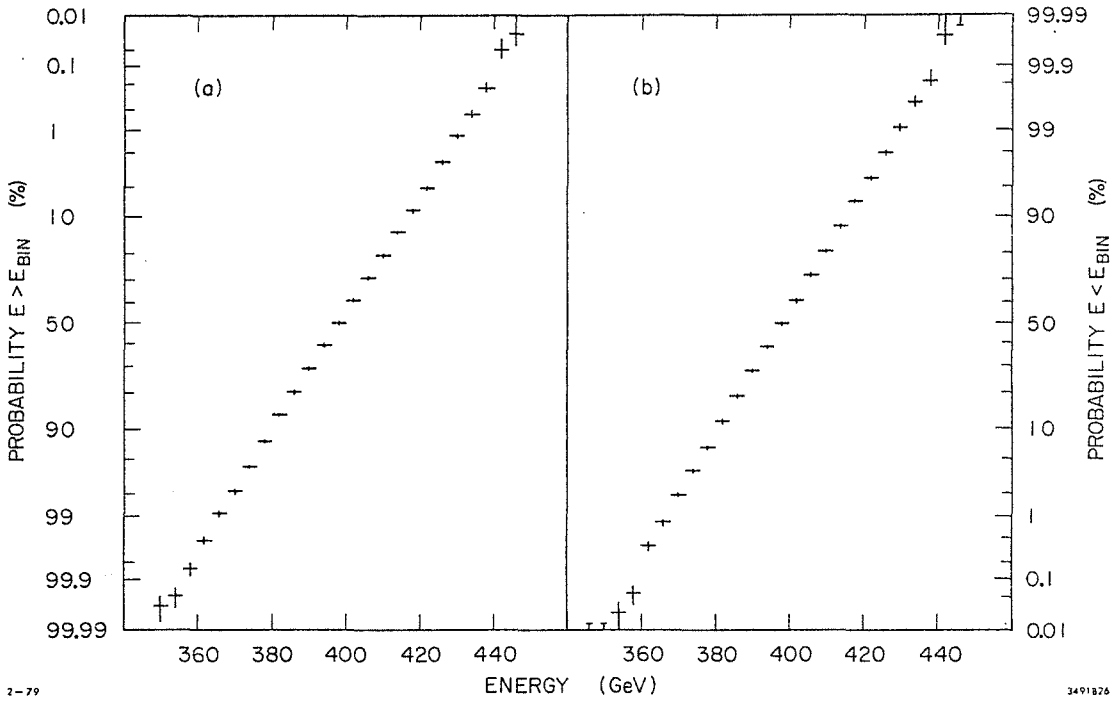

Fig. 17 Calorimeter response after weighting plotted on probability paper. A Gaussian response function translates as a straight line on this plot. Figure (a) is the unweighted measured energy and figure (b) is the weighted measured energy.

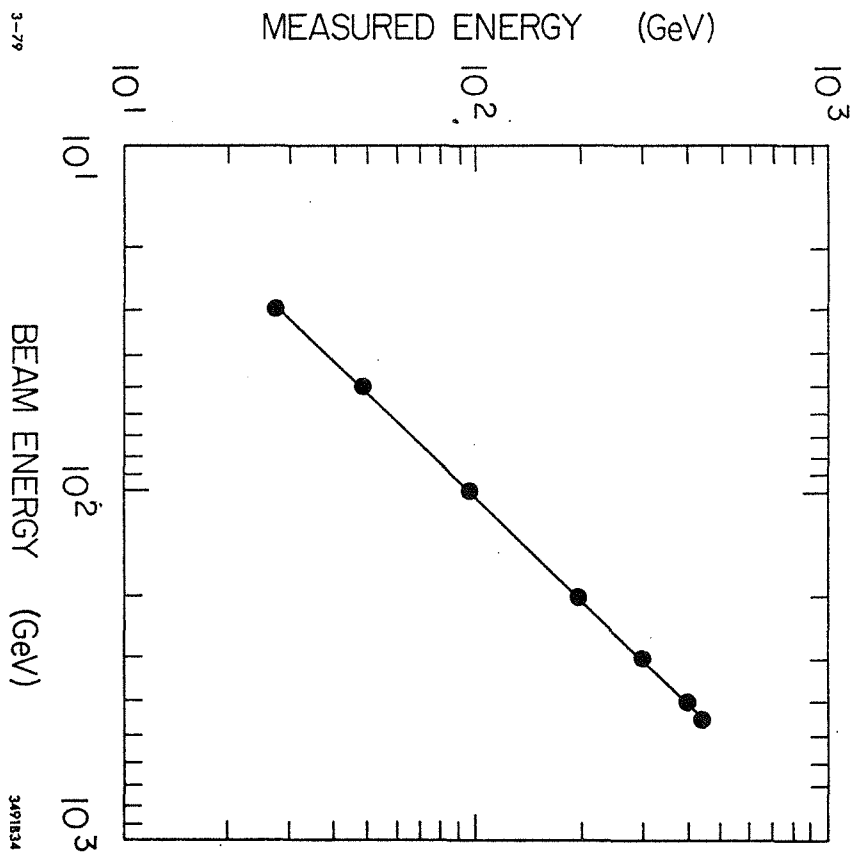

Fig. 18 The weighted measured energy versus incident beam energy

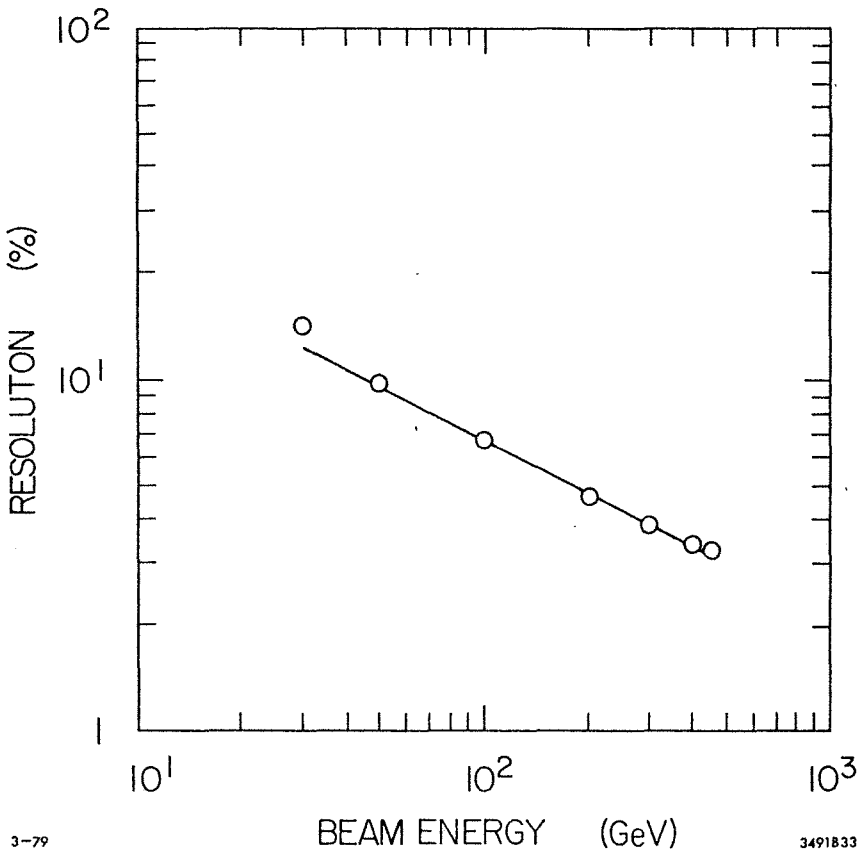

Fig. 19 The calorimeter resolution using the weighted measured energy versus incident beam energy.

Table II.

Calibration results

Method	Resolution
MUONS	4.60 %
SHOWER DEVELOPMENT	3.63 %
MINIMIZE RESOLUTION	3.42 %
SHOWER DEVELOPMENT WITH WEIGHTING	3.38 %

C. Rate Corrections to the Energy

Figure 20 is the measured energy at a high beam rate (300 kHz). The dashed histogram in figure 20 is the low intensity measured energy with the same number of events. It is clear that the measured energy suffered from beam rate effects. The origins of these effects stemmed from two sources. The first source arises from contributions to the total energy from beam particles that preceded the triggering particle. The second source of rate effects is due to gain shifts in the photo-tubes due to large currents in the anodes associated with the high counting rate. This second effect was mentioned previously in the discussion on apparatus. Fortunately, data was available to correct the energy for these rate effects. The corrections applied to the data to overcome these effects are discussed below.

1. EVENT HISTORY Correction

The pulse height associated with a shower in the calorimeter had

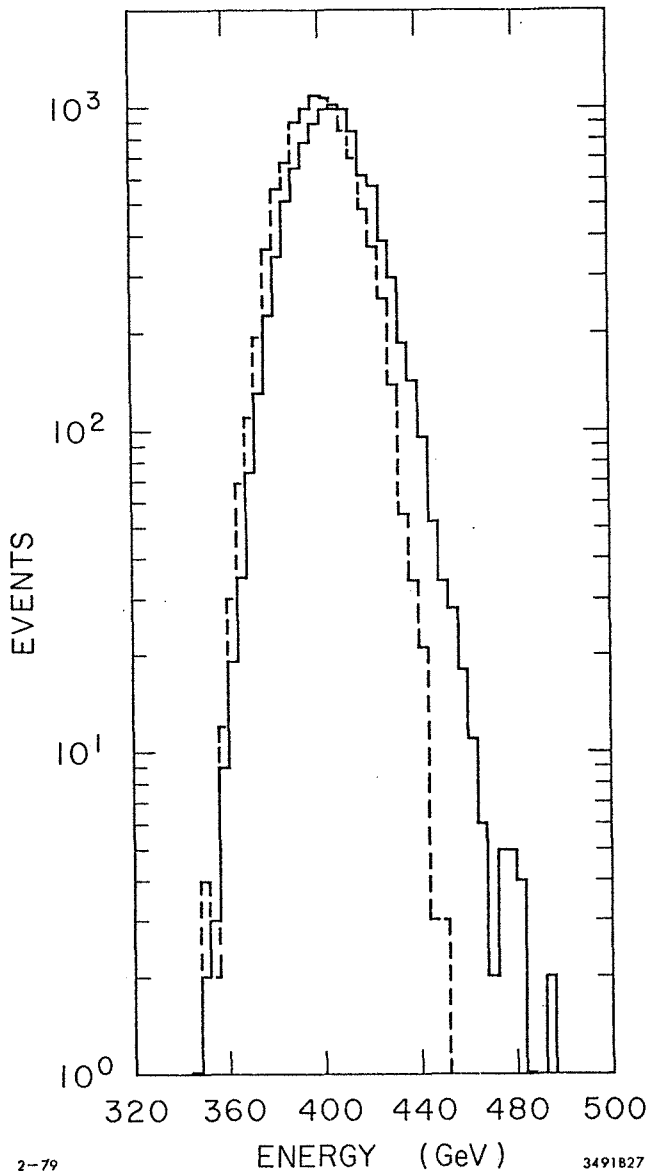

Fig. 20 High intensity measured energy before rate corrections (solid histogram) and low intensity measured energy (dashed histogram).

a long tail extending out to several hundred nanoseconds. At high rates, when the separation between consecutive beam particles decreased, it was possible for another beam particle to impinge on the calorimeter while the tail from the previous particle was still finite. This would lead to a measurement of the energy which was too large. The flasher system and the FLASHER HISTORY were used for studying this overlap effect. Once the effect was understood the EVENT HISTORY could be used to correct the calorimetry data.

To determine the amount of pulse height from the tail of preceding particles to the flasher signal, first the amount due to the flasher itself must be determined. To do this one uses the flasher data from the LED events taken before the spill. Using the flasher values for reference tube 1 and the calorimeter counters on this pre-spill event one forms the ratio

$$R_i = (FL_i/\text{REF } 1)_{LED}$$

where REF 1 is the reference tube 1 flasher value and FL_i is the flasher value for counter i. The LED indicator on this ratio means that it was measured on pre-spill events. To calculate the counter flasher value for the event flashers, one uses the reference tube 1 value for the event flasher and the above ratio. The calculated counter event flasher value is then

$$(FL_i)^{CALC}_{EVENT} = (FL_i/\text{REF } 1)_{LED}\ (\text{REF } 1)_{EVENT}$$

$$= R_i\ (\text{REF } 1)_{EVENT}$$

Subtracting this calculated value from the actual flasher value, $(FL_i)_{EVENT}$, yields the difference due to the tails from the particles before the flasher. To study the time dependence of this effect, those

events with only one hit in the FLASHER HISTORY have been selected. Figure 21 is a plot of the function

$$f(t) = \sum_{i=1}^{31} (FL_i(t))_{EVENT} - (FL_i)^{CALC}_{EVENT}$$

versus the position of the beam hit before the flasher in the FLASHER HISTORY where the sum over i is all of the counters which view the flasher. A fairly logarithmic dependence on the position is evident for times less than 20 r.f. buckets. There is an indication of deviation from this behavior at later times, but the effect at these late times is small and the statistics are poor. This behavior for each of the flasher counters has been fitted to a form

$$\Delta_i(t) = (FL_i(t))_{EVENT} - (FL_i)^{CALC}_{EVENT} = A_i\ e^{-t/\lambda}$$

where t is in r.f. buckets. A_i and λ are to be determined from the data. Figure 22 shows the X^2 distribution for this fit for various values of λ, where X^2 is defined as

$$X^2 = \sum_{i=1}^{50} \sum_{j=1}^{31} (\Delta_j(t_i) - A_j e^{-t_i/\lambda})^2/\sigma^2_{\Delta_j(t_i)}$$

where the sum over i is for a hit within the first 50 r.f. buckets of the FLASHER HISTORY, the sum over j is all of the counters which view the flasher, and $\sigma^2_{\Delta_j(t_i)}$ is the error in $\Delta_j(t_i)$. The minimum occurs for $\lambda = 7.5$ r.f. buckets although $\lambda = 8.0$ buckets is not significantly worse. For $\lambda = 7.5$ r.f. buckets, A_i was approximately 20% of the average shower profile value in counter i. With A_i and λ determined, the EVENT HISTORY hit distribution was then used to correct the measured calorimeter energy. A plot of the energy before and after the EVENT HISTORY correction is shown in figure 23. The dashed histogram in

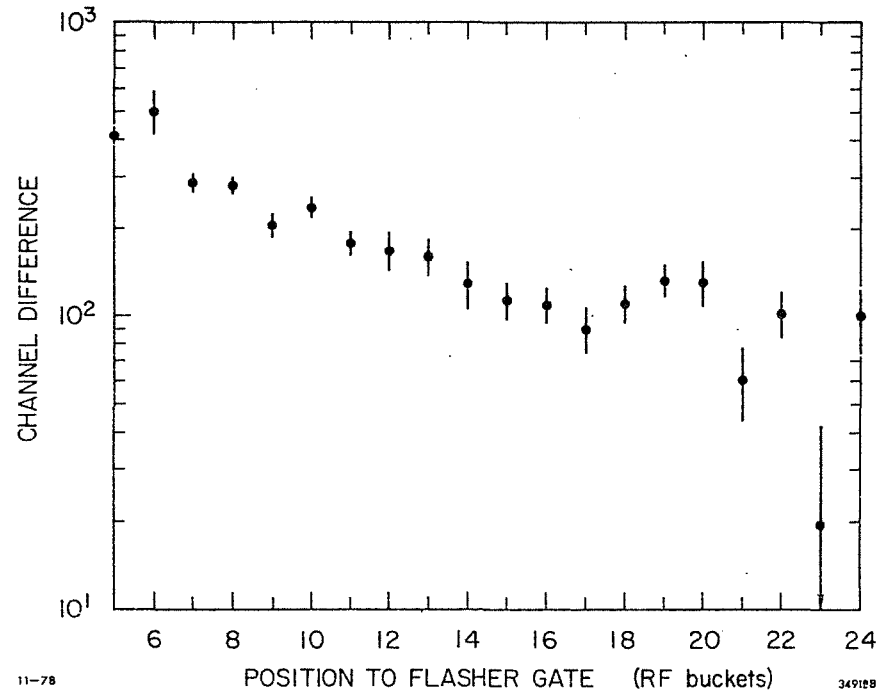

Fig. 21 The function f(t) as defined in the text versus the position of the hit in the FLASHER HISTORY before the flasher gate.

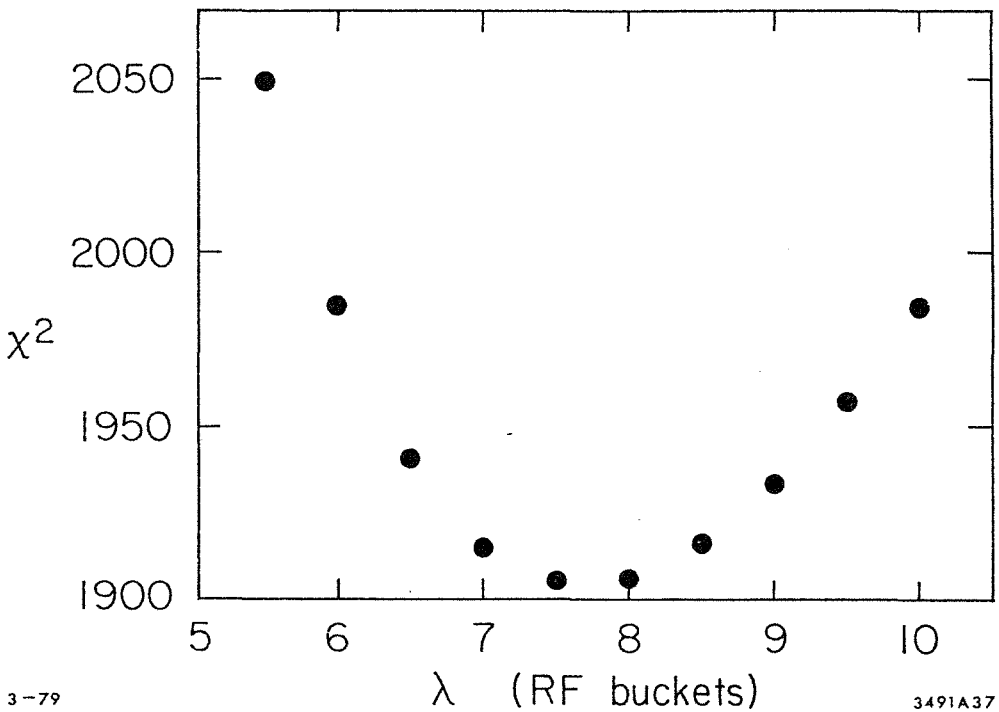

Fig. 22 χ^2 distribution for a fit to the flasher differences of the form $Ae^{-t/\lambda}$ where t is the position of the hit in the FLASHER HISTORY.

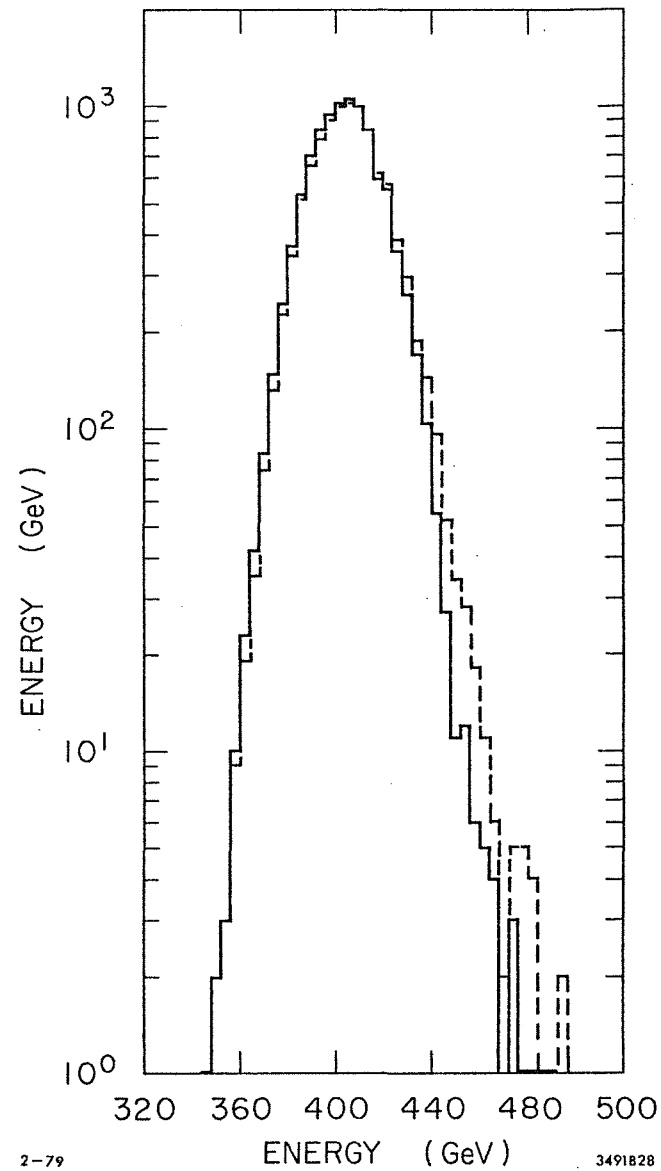

Fig. 23 High intensity measured energy after EVENT HISTORY correction (solid histogram) and before rate correction (dashed histogram).

figure 23 is the uncorrected energy. A significant portion of the high tail is now removed from the data. The residual tail will be discussed in a later section.

Although the EVENT HISTORY correction removes some of the high intensity effects, a glimpse at figure 23 indicates that there are additional rate effects. One such effect is discussed next.

2. FLYING SCALER Correction

Prior to the data taking, measurements were performed on each of the phototubes to study the effect of the gain at high anode currents. These measurements were mentioned briefly in Chapter III and are discussed at some length in Appendix B. The residual rate effect mentioned above could certainly be associated with these effects. The FLYING SCALER was most useful for studying these effects. Although the fluctuations are large, a 400 GeV proton will deposit some average number of m.i.p. in each counter. Keeping track of how many protons hit the calorimeter and when they arrive will give a measure of the current in each phototube since the total current is just the charge deposited at the anode from a single m.i.p. times the average number of m.i.p.s per proton times the number of protons per second. It is possible to study the measured energy as a function of this current.

As discussed in Chapter III, the FLYING SCALER contained twelve scalers. For each scaler the number of protons in a given time interval and the time before the event at which this intensity occurred is available. To study the rate effects with the FLYING SCALER, it was useful to parameterize the FLYING SCALER data in terms of a quantity

called the rate parameter, η, which accounts for possible relaxation effects in the gain shifts by using the time information of the FLYING SCALER. η is determined from the FLYING SCALER by the relation

$$\eta = \sum_{i=1}^{12} N_i \, e^{-t_i/\lambda_{FS}}$$

when N_i is the number of counts in the ith scaler and t_i is the time before the event which this i^{th} scaler was counting. λ_{FS} is a characteristic time associated with the intensity effects on the phototube gain. λ_{FS} is not known a priori, but must be determined from the data.

Figure 24(a) shows a plot of the fractional change in the measured energy versus the rate parameter with λ_{FS} = 300 μsecs. There is a clear monotonic dependence on the rate parameter. The dependence on the rate parameter for various values of λ_{FS} was investigated. The value λ_{FS} = 300 μsecs produced a dependence of the fractional energy on the rate parameter which best approximated an exponential distribution and was thus chosen for the rate parameter calculation. As a comparison, the dependence of the fractional energy on the total number of counts in the FLYING SCALER ($\lambda_{FS} = \infty$) is also shown in figure 24(b). The fractional energy change does not go to zero with $\lambda_{FS} = \infty$ as expected if the $\lambda_{FS} = \infty$ rate parameter was a good indicator of the rate effects in the phototube. The measured energy in these plots has been corrected using the EVENT HISTORY correction.

Although the energy dependence on the rate parameter was not a simple function, this dependence could still be used to correct the energy for this effect. This is done by simply interpolating between the data points in figure 24(a). For a given event one first calculates the rate parameter from the FLYING SCALER data. Having determined

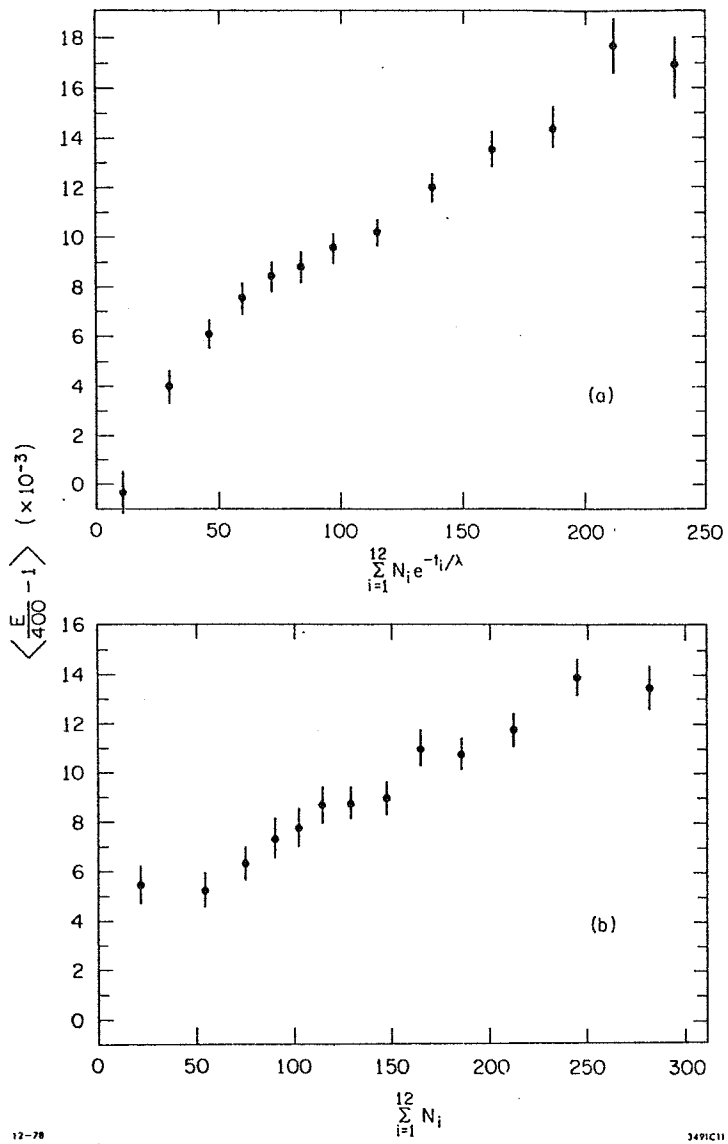

Fig. 24 (a) Fractional change in the measured energy versus the FLYING SCALER rate parameter with λ_{FS}=300 μsecs.

(b) Fractional change in the measured energy versus the FLYING SCALER rate parameter with $\lambda_{FS}=\infty$.

the range in which this parameter lies in figure 24(a), a linear interpolation scheme is used to determine the fractional energy shift

$$\frac{\Delta E}{E}(\eta) = \left(\frac{\Delta E}{E}(\eta_2) - \frac{\Delta E}{E}(\eta_1)\right)(\eta-\eta_1)/(\eta_2-\eta_1) + \frac{\Delta E}{E}(\eta_1)$$

with

$$\eta_2 > \eta > \eta_1$$

$\frac{\Delta E}{E}(\eta_i)$ is the measured fractional energy change at the value of the rate parameter η_i. Having determined the fractional change, the FLYING SCALER corrected energy is determined from the relation

$$E_{FS}^{CORR} = E_{MEAS}\left(1 - \frac{\Delta E}{E}(\eta)\right)$$

where E_{MEAS} is the uncorrected energy. Figure 25 shows the EVENT HISTORY corrected energy before and after the FLYING SCALER corrections. The final corrected measured energy relative to the low intensity measured energy is shown in figure 26. After applying the cuts described below the final resolution was increased by approximately 3% of the low intensity value.

D. Data Cuts

In an attempt to reduce low energy tails arising from systematic calorimeter effects, cuts have been applied to the calorimetry data. These cuts are discussed in detail below.

1. Position of Primary Interaction

Events with a large amount of albedo which occur in the first plate will tend to have a lower energy than the rest of the events because this albedo leaves through the front of the calorimeter.

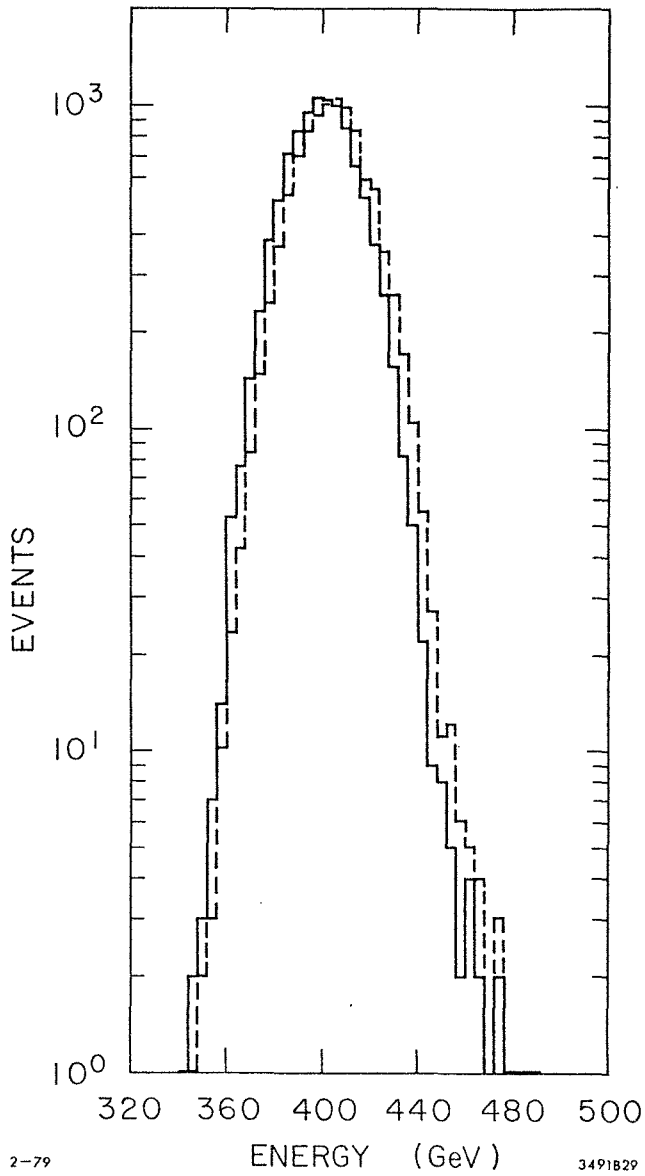

Fig. 25 High intensity measured energy after FLYING SCALER and EVENT HISTORY correction (solid histogram) and after only the EVENT HISTORY correction (dashed histogram).

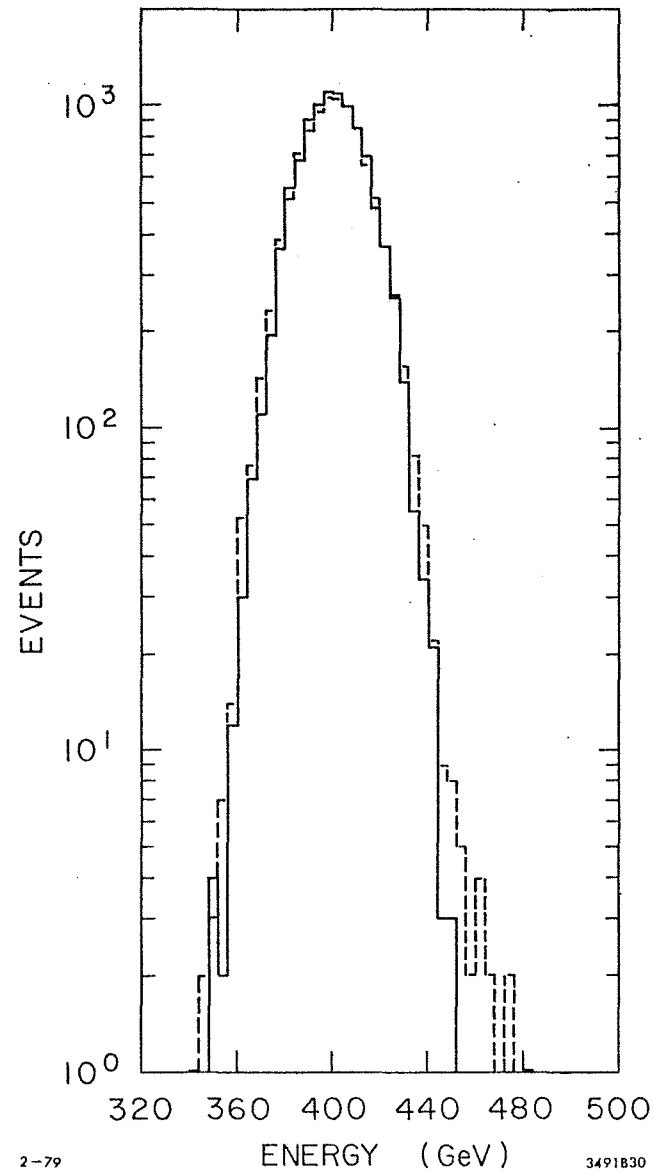

Fig. 26 Low intensity measured energy (solid histogram) and final corrected high intensity measured energy (dashed histogram).

These large albedo events will also give a large pulse height in counter B2 which is mounted to the front of the first plate. By including B2 as a counter in the shower algorithm for determining the beginning of the shower, these large albedo events will appear as showers which begin before the first plate.

Figure 27 shows the measured energy as a function of the shower beginning. The beginning of the shower is defined as the first counter with more than 30 m.i.p. followed by another counter with more than 30 m.i.p., a slightly different definition than used previously for the shower development calibration. A systematic effect is seen for events which begin close to the front of the calorimeter. Accordingly, a cut was applied requiring that the shower begin in or beyond plate 1 as determined from the algorithm. A cut was also applied requiring that the interaction occurred before the 10th plate to help remove abnormally long showers.

2. Total Energy Sum

A cut was placed on the data such that the total interaction had less than 500 GeV total energy. This cut was used to eliminate events with two particles in the same bucket.

3. Shower Profile Cuts

Although on the average the hadron shower is completely contained in the calorimeter, longitudinal fluctuations in the shower profile could yield systematic effects in the measured energy. In particular, very long showers have lower energies due to particles lost out

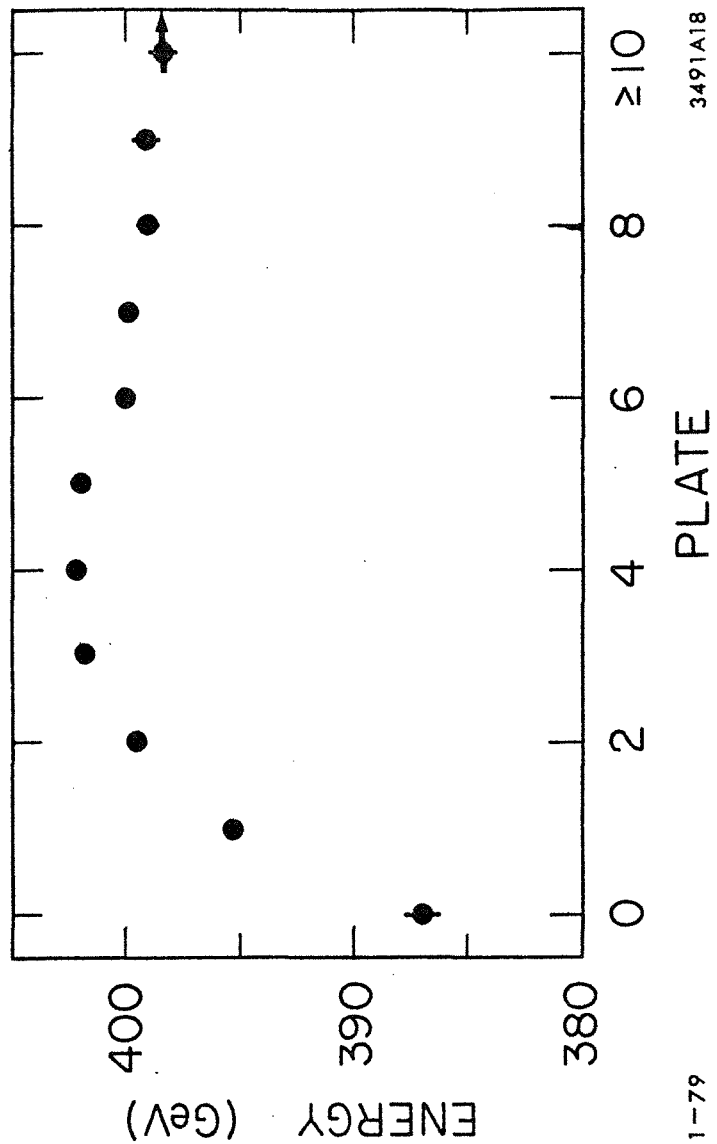

Fig. 27 Calorimeter measured energy versus the plate in which the primary interaction occured. Approximately 5 plates is equal to a proton absorption length in iron.

of the back or side of the calorimeter.

One source of longitudinal fluctuation would be showers that have a high energy hadron leaving the back of MacMurphy giving a large pulse height in the Chief with possible energy being lost out of the back of the calorimeter. One indication of this would be large simultaneous energy deposition in contiguous Chief planes. This can be studied by using the variable

$$\text{SUMCON} = \text{MAXIMUM}\,(n_1^{CHIEF}+n_2^{CHIEF}+n_3^{CHIEF},\ldots n_i^{CHIEF}+n_{i+1}^{CHIEF}+n_{i+2}^{CHIEF},\ldots,n_8^{CHIEF}+n_9^{CHIEF}+n_{10}^{CHIEF})$$

where n_i^{CHIEF} is the number of m.i.p.s in the ith Chief plane. Figure 28 shows the measured energy as a function of SUMCON. There is an indication that for large values of SUMCON the measured energy is lower. A cut was applied to the data requiring SUMCON be less than 30 m.i.p.s.

Another source of fluctuation would be the relative amount of energy deposited in the first 20 plates to the total energy. A small value for this quantity would indicate that most of the shower occurs deep in the calorimeter. These long showers could produce particles which leave the calorimeter through the back or the side. Figure 29 shows the measured weighted energy as a function of the fraction

$$R = \sum_{i=1}^{20} E_i \,/\, E_{MEAS}$$

where E_i is the energy measured in counter i. A systematic effect on the energy measurement is readily apparent. The data was cut requiring that the ratio R be greater than 0.5.

4. Upstream Interaction Cuts

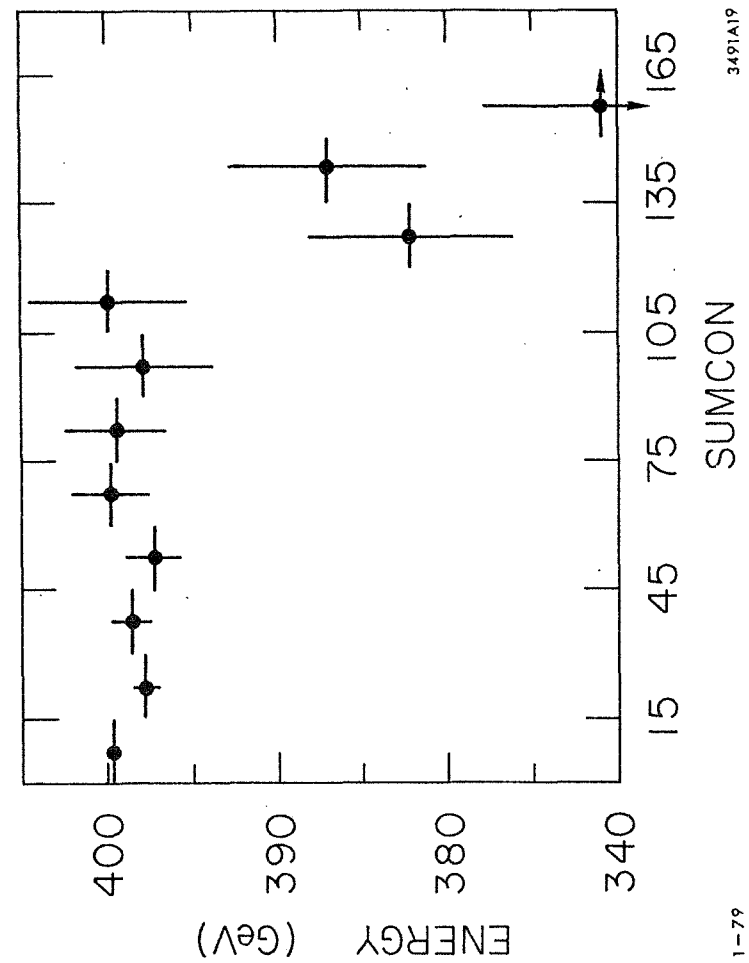

Fig. 28 Calorimeter measured energy versus SUMCON (the sum of the number of m.i.p. in 3 contiguous Chief counters as defined in the text).

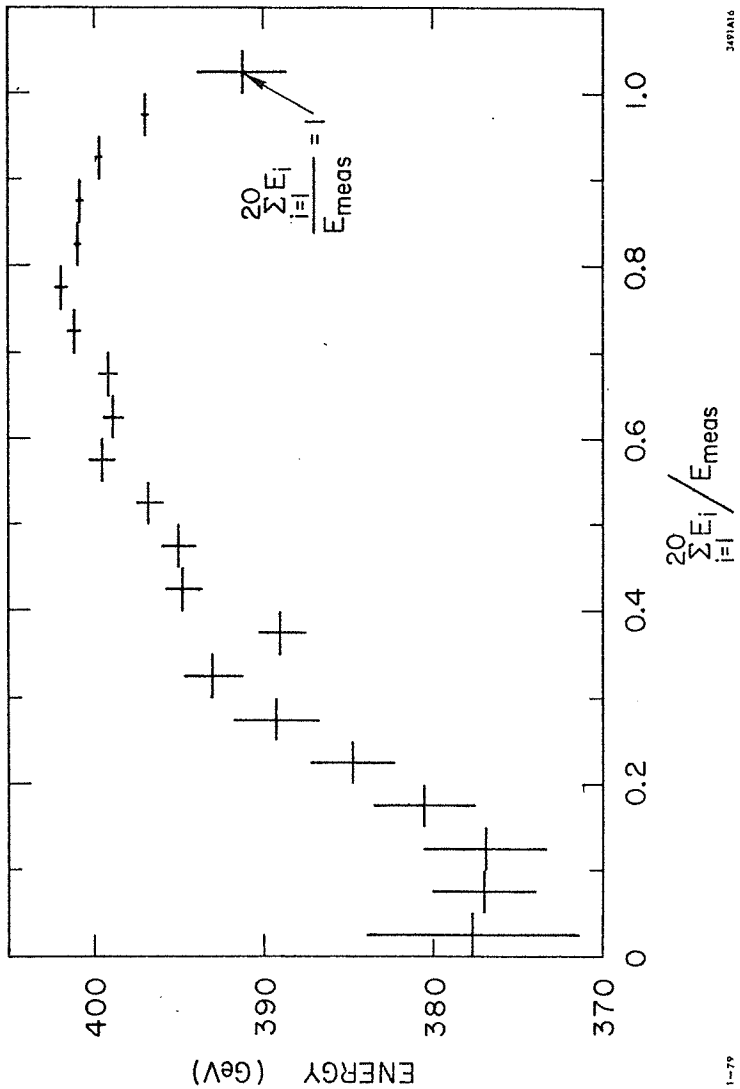

Fig. 29 Calorimeter measured energy versus the ratio of the energy deposited in the first 20 plates to the total energy. E_i is the energy deposited in plate i.

A number of minor cuts were put on the data to help improve the quality of the beam. These cuts consisted of requiring the pulse height in B0 be less than 4 m.i.p. and that the number of hits in the 4th PWC be less than or equal to 2 in both x and y. A cut was also applied requiring that the instantaneous beam rate before the trigger as calculated by the FLYING SCALER rate parameter be less than 212.5. This last cut was used to facilitate the FLYING SCALER rate correction.

5. Muon Cuts

Muons created in the hadronic shower will give rise to a low energy tail similar to ν production. These muons would leave the calorimeter without interacting, losing energy only through ionization. To be sure that only νs are giving rise to a low energy tail, the events with muons in the final state have to be removed from the data sample. Events with muons in the data were eliminated using two cuts, both of which rely on the fact that the muon's penetrating power offers a unique signature for identification. Muons which were at low angles to the beam line were eliminated by a cut on the Chief pulse height. Wide angle muons were eliminated using the toroid acrylic counter information. The acrylic counters are shown in figure 9. The penetration of the steel in front of these counters gives a clearly identified muon. The spark chamber information was not used since this data was not available for all of the runs.

A m.i.p. in a given Chief plane was defined as any counter in that plane giving more than .25 times the muon calibration value of a m.i.p. in the Chief:

$$(1\ \text{m.i.p.})_i = n_i^{\text{CHIEF}} > .25$$

where $(1\ \text{m.i.p.})_i$ is either 0 or 1 and means that the Chief plane i had indications of one or more m.i.p. $(1\ \text{m.i.p.})_i$ is then summed over all of the planes in the Chief.

$$\text{TOTL} = \sum_{i=1}^{10} (1\ \text{m.i.p.})_i$$

and a cut was placed on TOTL to remove penetrating particles, i.e. muons.

To find the position of this cut, the TOTL distribution is studied for events with previously identified muons in the Chief. Events with muon triggers were selected for this purpose. It was also required that these events with muon triggers have only 1 reconstructed track in the spark chambers, that the momentum of the muon be measured in the toroid spectrometer, and that the transverse position of the track be such that it penetrated all of the Chief. These constraints insured that a real muon penetrated the total length of the Chief. A large beam rate was also selected to take acount of a.c. coupling effects in the first few Chief planes. Figure 30 shows the TOTL distribution for these events. There are only 2 events out of the 14,923 events in the sample with TOTL less than 5. Thus for the I.B. events it is required that TOTL be less than 5. A calculation based on the measured muon rate from unbiased proton interactions (1%) yields a contribution of .25 events with muons which passed the TOTL cut in the final data sample.

Wide angle muons in the data sample were eliminated by requiring that no more than 1 out of the 3 acrylic counter planes fired. The efficiency of an individual acrylic counter was determined by comparing

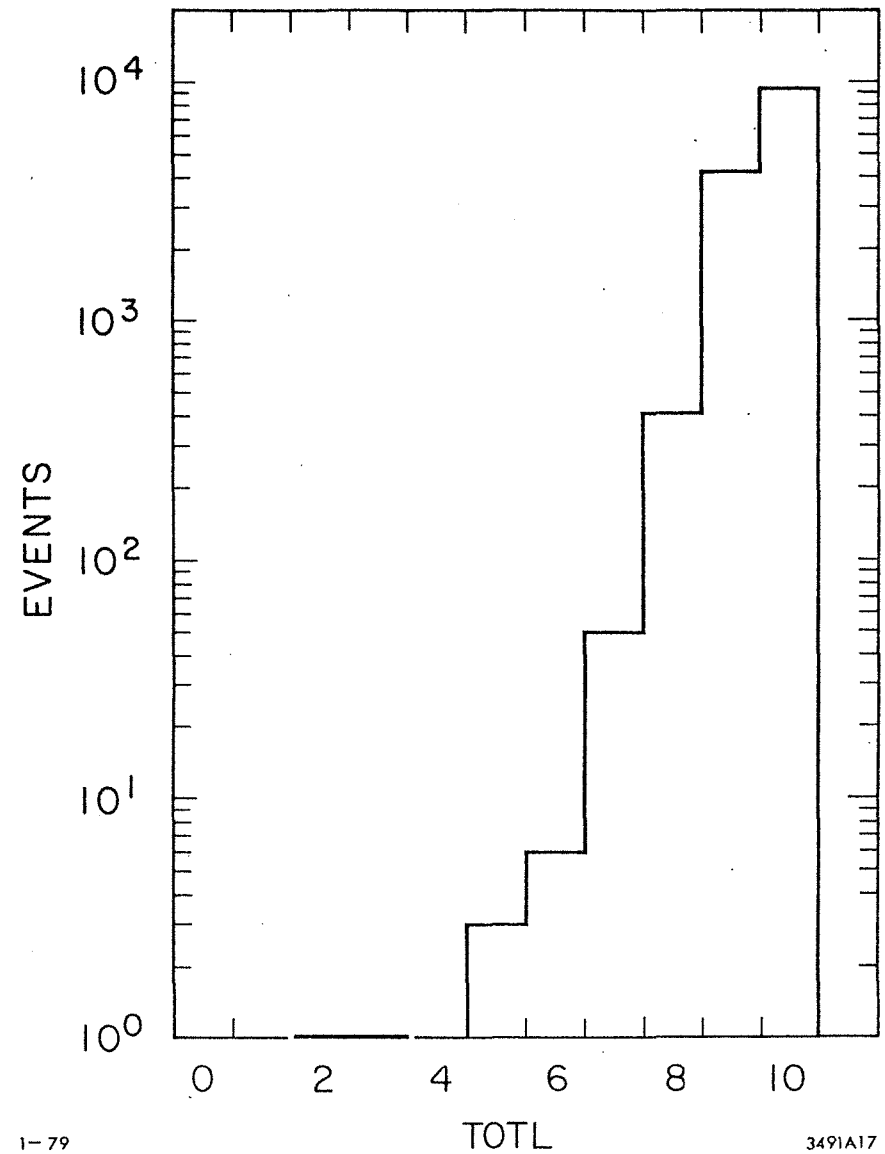

Fig. 30 TOTL (the number of planes showing passage of a m.i.p. in the Chief as defined in the text) for momentum analyzed muons which passed completely through the Chief. There are 2 events with TOTL less than 5.

the number of times all three of the acrylic planes fired to the number of times only two of the planes fired for muon events with reconstructed momentum. Since the muon trigger only required that two of the counters fire, this method gives an unbiased measure of the counter efficiency. An individual counter thus measured gave an efficiency of approximately 90%. The efficiency of the acrylic counters for detecting muons if two or more are required to fire is then

$$P_{WIDE} = P^3 + 3P^2(1-P) = .729 + .243 = 97.2\%$$

where P is the efficiency per plane in the acrylic counters and P_{WIDE} is the total probability of the acrylic counters to detect the muon. Using the prompt μ/π ratio of 10^{-4} measured in proton-proton interactions {47} and taking $N_\pi = 10$, the calculated number of events in the data sample due to wide angle muons only is

$$N_{\substack{WIDE\\ANGLE}} = 1/3 \times \frac{10\ \pi\text{'s}}{\text{PROTON}} \times 10^{-4}\ \frac{\mu}{\pi} \times 2\text{x}10^5\ \text{PROTONS} \times (1-P_{WIDE})$$
$$= 1.8 \text{ events.}$$

The factor of 1/3 comes from those wide angle muons which also traverse the Chief and were subsequently eliminated by the cut on TOTL. This calculation assumes that the prompt muons come only from the primary proton interaction in the calorimeter.

The effect of these cuts on the low intensity I.B. data was to decrease the resolution from 3.48% to 3.40% and to eliminate 16% of the events. For the whole data sample, the effect of the cuts was to reduce the number of events from 197,168 to 150,499 and to improve the resolution from 3.84% to 3.51%. The fraction of events lost due to the various cuts is shown in Table III. The energy distribution after all

corrections and after all the cuts had been applied is shown in figure 31.

Table III.

Percentage of events lost by cuts

Cuts	Fraction Lost (%)
Beginning of shower	5.64
Total energy	.77
Ratio of energy in 1st meter	2.76
Energy in Chief	1.75
Muon in Chief	4.30
Wide Angle Muons	1.61
Good Beam Particle Cuts	
Particle in ADC gate	1.37
Rate Parameter	3.80
HALO cut	1.60
Unique beam track	3.75
Clean beam requirements	5.51
Total fraction of events lost by cuts	23.55

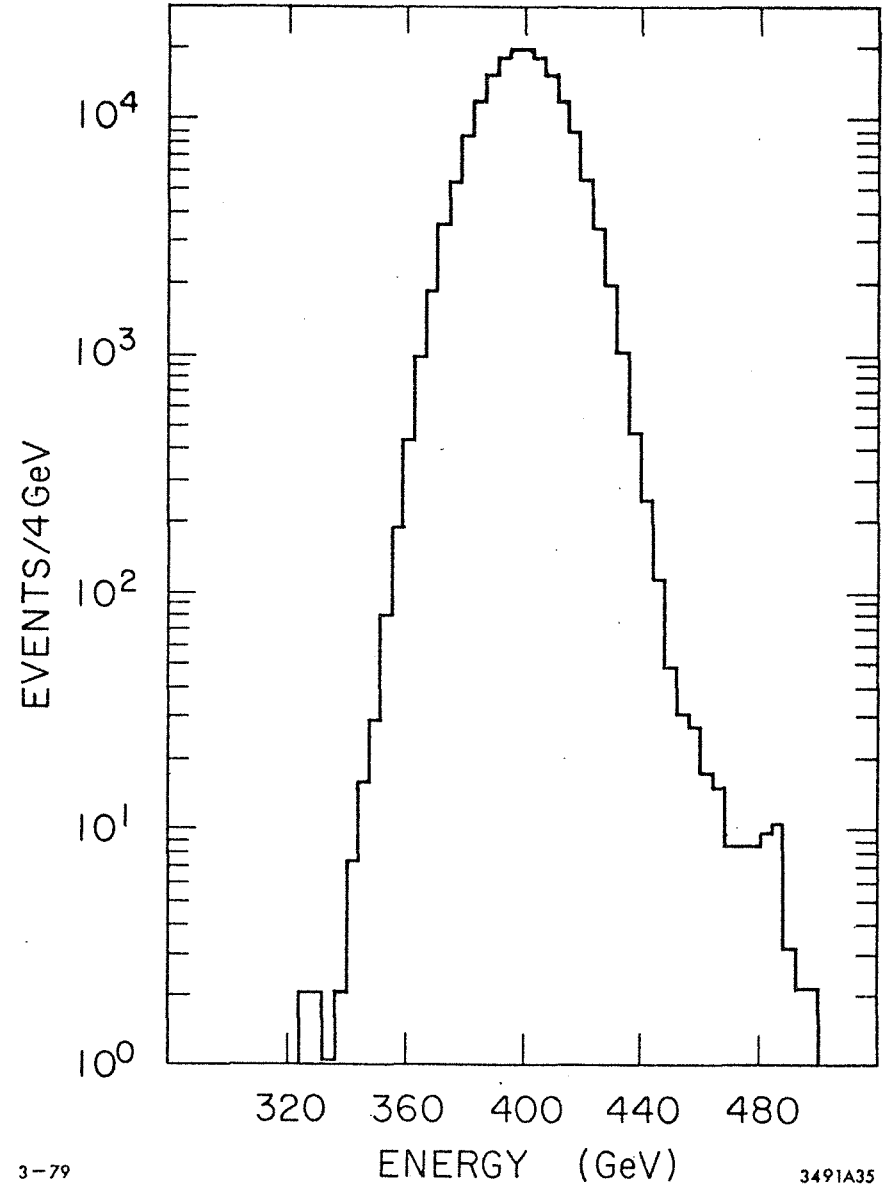

Fig. 31 Final calorimeter measured energy after all corrections and cuts.

CHAPTER VI

Results and Conclusions

How can the energy distribution shown in figure 31 yield information on the production of neutrinos and other neutrino-like particles? First, one must determine the contribution due to the calorimetry process alone in the low energy distribution in figure 31. Excesses beyond this measurement contribution then allow us to set limits on the production of weakly interacting particles. Given a model for this particle production, one must calculate their contribution to the calorimeter response for each of these production models. From these model calculations and the observed distribution, a maximum likelihood analysis then yields the amount of cross section going into these neutrino-like particles.

A. Calorimetry Backgrounds

At some level one expects that the measurement process in hadron calorimetry will obey the law of large numbers leading to a Gaussian response function for the measured energy distribution. Figure 32 and Table IV are more detailed versions of the energy distribution of figure 31. If we compare the data to the Gaussian distribution calculated from a fit to the low energy side of the measured energy distribution, a slight enhancement is noticed. One is leary of claiming evidence for prompt neutrinos based on this data. There could be additional sources of background that might fake such a signal. Although the data has been cut to ensure complete containment of the hadronic shower, there is no definitive way of ruling out an anomalous

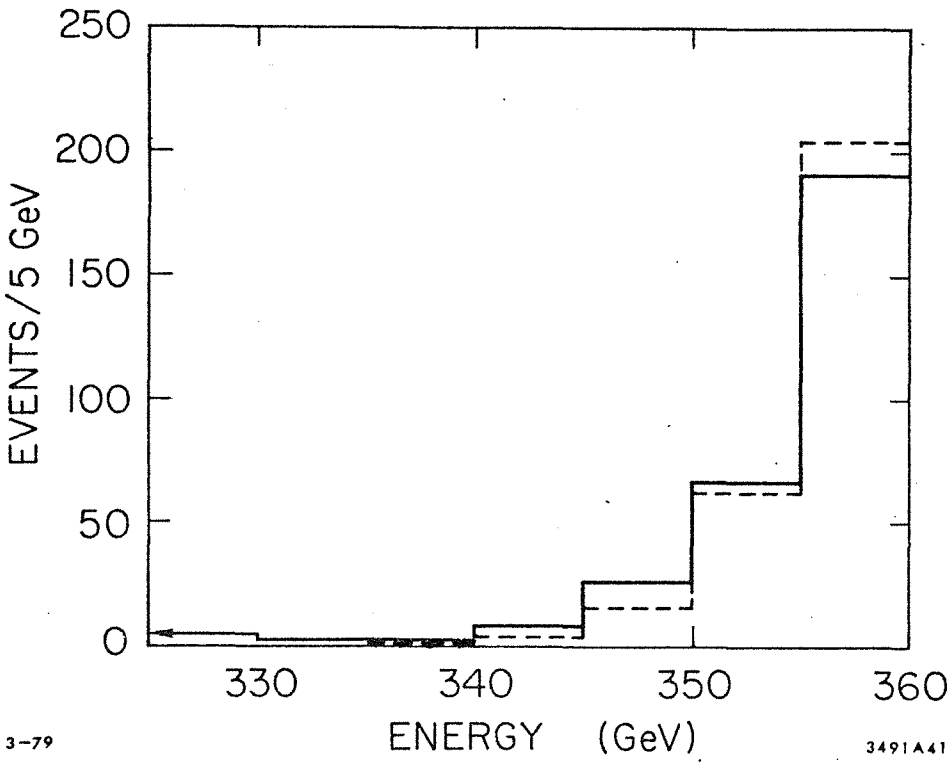

Fig. 32 Low energy distribution of figure 31. The dashed histogram is the measured energy distribution expected from a Gaussian response function using the σ obtained from a fit to the low side of figure 31.

Table IV.

Expected and observed number of low energy events

Energy	Gaussian	Data	Excess
355-360	204	191	-13
350-355	64.1	66	+1.9
345-350	17.7	26	8.3
340-345	4.27	8	3.73
335-340	.91	2	1.09
330-335	.17	2	1.83
<330	.04	3	2.96

fluctuation in the transverse energy deposition with energy leaving the sides of the calorimeter. A naive calculation indicates that the high p_T process usually associated with proton-proton interactions is unlikely to cause such a fluctuation. Nevertheless, some heretofore unknown mechanism may produce such events. Large amounts of energy leaving the front of the calorimeter seems unlikely as a source of a low energy tail.

As well as the above mentioned background, an enhanced energy distribution could arise from neutrinos due to decays of πs and Ks produced in the hadronic shower. Considering the fact that the neutrino energy has to be 50 GeV or more, the contribution from π and K decay can be estimated by just considering the first interaction in the calorimeter. Realizing that the μ produced in any decay has to range out in the calorimeter for the event to be accepted due to the

muon cuts on the data, the number of decays is then

$$N_{E_\nu>50} = BR(h\to\nu)\, N_{had}\, N_P \int_{E_{THRES}}^{E_{MAX}} P^{had}_{decay}(E')\, \frac{dP^{had}}{dE'}(E')\, P^{had}_{E_\nu>50}(E')\, dE'$$

where

E_ν	= neutrino energy
$N_{E_\nu>50}$	= the number of events with E_ν greater than 50 GeV
N_{had}	= the number of πs (Ks) produced per proton in the data sample
$BR(h\to\nu)$	= branching ratio for the hadron to decay to a neutrino
N_P	= the total number of protons in the data sample
E_{THRES}	= the threshold energy for production of 50 GeV neutrinos
$P^{had}_{decay}(E')$	= the probability that a particle of energy E' decays within one interaction length in the calorimeter
$\frac{dP^{had}}{dE'}(E')$	= the probability that a particle of energy E' is produced in the first interaction
$P^{had}_{E_\nu>50}(E')$	= the probability that a particle of energy E' decays to give a neutrino energy greater than 50 GeV
E_{MAX}	= maximum hadron energy consistent with μ range out in the calorimeter

The decay probability within one interaction length is simply

$$P^{had}_{decay}(E') = 1-e^{-\lambda_\pi/\beta\gamma c\tau} \simeq \frac{\lambda_\pi}{\beta\gamma c\tau}$$

where $\beta\gamma$ is the Lorentz factor

$$\beta\gamma = P/M_{had} \simeq E'/M_{had}$$

τ is the hadron lifetime and λ_π is the pion absorption length in the calorimeter. The production probability is taken to be of the form {48}

$$E\,\frac{d^3\sigma}{dp^3} = A(x_R)\left[1 + p_T^{\,2}/M^2(x_R)\right]^{-q(x_R)}$$

with

$$x_R = E^*/E^*_{MAX}$$

E^* is the center of mass energy of the produced hadron and E^*_{MAX} is the maximum value of this quantity. The neutrino spectrum is taken to be flat from the threshold energy to the maximum allowed neutrino energy for the decay. This is of the form

$$P^{had}_{E_\nu>50}(E') = 1 - \frac{E_{THRES}}{E'}$$

For the two body decays

$$\pi \to \mu\nu,\ K \to \mu\nu$$

the muon energy in the decay has a probability distribution which is flat from

$$\frac{M_\mu^{\,2}}{M_h^{\,2}}\, E_h \le E_\mu \le E_h$$

where E_h and M_h are the energy and mass of the decaying hadron respectively, E_μ is the muon energy, and M_μ is the muon mass. For the decays to contribute the μ must range out in the calorimeter which places an upper limit of less than 3.5 GeV for its energy. Thus, π decay ($(M_\mu/M_\pi)^2$ = .57) could at most yield a 2.7 GeV neutrino and satisfy the condition on the muon energy. For K decay ($(M_\mu/M_K)^2$ = .046) there is a range of kaon energies which would satisfy the muon energy condition and give a

50 GeV neutrino

$$52.4 < E_K < 76.6$$

In this case the probability for a 50 GeV neutrino in the decay is

$$P^{had}_{E_\nu>40}(E') = \frac{\text{MINIMUM}(3.5-E_\mu,\{(1-\frac{M_\mu^2}{M_K^2})E' - 50\})}{\{(1 - M_\mu^2/M_K^2)E'\}}$$

For the three body electronic decays of the kaons

$$K^{\pm,o} \rightarrow \pi^{o,\mp} e^{\pm} \nu$$

all kaon energies above threshold contribute. In this case the neutrino energy in the decay will range from

$$0 < E_\nu < \{1 - (M_\pi^2/m_K)\}E_K$$

Thus, kaon energies above 52.4 will contribute. Putting the conditions into the above integral and using the production spectrum and multiplicities (scaled by 1.85 to account for nuclear effects) for $K^{\pm}$,K^o production in proton-proton interactions {48}, the following is obtained

$$N(K^{\pm} \rightarrow \mu\nu)_{E_\nu>50} = .0006 \text{ events}$$

$$N(K^{\pm},K^o \rightarrow \pi e\nu)_{E_\nu>50} = .005 \text{ events}$$

for a total of .006 events. Therefore, shower particle decay is a negligible contribution to the low energy tail distribution.

Although there may be sources of undetermined background in the low energy tail, this data can still be used to set limits on the production of neutrino-like objects. One can rely on the fact that at best, the number of events from neutrino-like sources has to be less than or equal to the observed data. In this spirit, the final production limits established in this thesis have been determined for

three possible cases:

(1) no Gaussian background for events with energies less than 340 GeV

(2) a normal Gaussian background for all events

(3) the observed data is all background

where the Gaussian background is calculated from the σ obtained from a fit to the low side of the measured energy from 335-400 GeV. This fit yields a value for σ of 13.85 GeV/c with a χ^2 of 16.5 for 13 degrees of freedom. The σ for the whole distribution is 14.04 GeV, but this value is affected by the high energy tail of the distribution discussed below and is not a good measure of the Gaussian response on the low energy side of the distribution (a χ^2 of 44.3 for 13 degrees of freedom). The true upper limit is clearly case 1, but it is worthwhile to consider the other two cases as well to get an indication of the range of cross section values consistent with the data.

B. High Energy Tail

The prominent feature of the final measured energy distribution is the tail on the high energy side of the measurement. What is the origin of this tail? How does it effect the results of this experiment? If we compare the high tail in figure 31 to the energy before the rate effects are corrected, shown in figure 20, a strong similarity is evident. The FLYING SCALER correction is not large enough to account for this tail, being at most a few percent. It is similar though, to the energy distribution obtained for those events when there is evidence of particles hitting the calorimeter during the ADC gate as indicated by

the EVENT HISTORY. The following discussion considers this high energy tail in detail. The point of what follows is that the high energy tail is due to an extra deposition of energy in the calorimeter and does not effect the physics of the low energy tail.

There are two possible sources which could deposit more than 400 GeV in the calorimeter and both involve the fact that it is possible to have more than one particle in or near the r.f. bucket of the triggering particle. Approximately 20% of the high intensity data was selected to investigate these sources. Considering just those good events with energies beyond 450 GeV, there are 43 events in the high energy tail whereas 7 events are expected. Thus, there is an additional 36 events not accounted for.

Recall that a subtraction is made to the measured energy for tails arising from beam particles before the event. This correction is of the form

$$\Delta E(t) = Ae^{-t/\lambda}$$

where λ is 7.5 r.f. buckets. The EVENT HISTORY which is used in this subtraction records only whether there was a particle hitting the calorimeter, not how many particles. Thus, there is no way of telling whether there was one or more than one particle in the bucket before the event. Looking at the EVENT HISTORY distribution for the 43 events beyond 450 GeV, there are 10 events with hits within 20 r.f. buckets of the beam particle. One expects only 4 events with random hits from the EVENT HISTORY distribution from the total sample. Events with double hits beyond 20 r.f. buckets could not contribute a significant amount to the measured energy. If all of these hits were double hits then this would explain part of the high energy tail. Is this number consistent with the total EVENT

HISTORY distribution? Figure 33 is the distribution of the first hit in the EVENT HISTORY other than the beam hit. The distribution in figure 33 can be used to calculate the number of events expected with double occupancy in a bucket. The double occupancy probability per bucket is simply

$$P_i = \frac{N_i}{2\,N_{TOTAL}}$$

where P_i is the probability per bucket for a hit in the EVENT HISTORY, N_{TOTAL} is the number of events in the whole sample, N_i is the number of hits in bin i, and the factor 2 comes from 2 buckets per bin. The double hit probability is just $P_{DOUBLE}^{BIN_i}$

$$P_{DOUBLE}^{BIN_i} = 2\,P_i^2 = \tfrac{1}{2}\left(\frac{N_i}{N_{TOTAL}}\right)^2$$

where again the factor 2 comes from 2 buckets per bin. The number of double hit events is simply $N_{DOUBLE}^{BIN_i}$

$$N_{DOUBLE}^{BIN_i} = P_{DOUBLE}^{BIN_i}\,N_{TOTAL}$$

The number of events calculated from the above prescription is 13 events for hits up to 20 buckets before the event which is not inconsistent with the 10 events observed.

A similar high energy tail would occur if particles were hitting the calorimeter after the beam hit and during the ADC gate. These events are eliminated in the analysis by checking the EVENT HISTORY distribution within this time period. However, if the EVENT HISTORY were inefficient then a few such events could still be in the final sample. The light flasher system was used to investigate this source

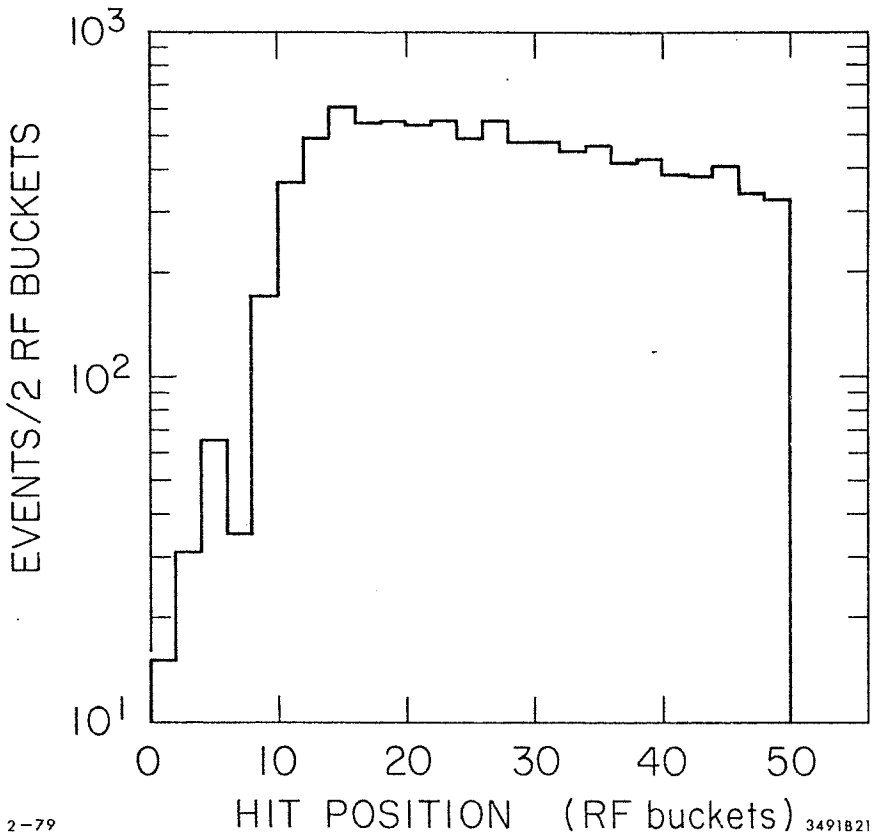

Fig. 33 The distribution of the first hit in the EVENT HISTORY other than the triggering particle for the high intensity data sample considered in the text.

using a sample of data in the later part of the run where the timing for the FLASHER HISTORY was well defined (see Chapter III). After subtracting the contribution to the counter flasher pulse height due solely to the flasher (as in Chapter V), the additional pulse height can be converted to an energy and studied versus the FLASHER HISTORY distribution. Taking only those events where there is no hit in the FLASHER HISTORY during the ADC gate, 27 events are obtained with residual energies greater than 70 GeV out of a total sample of 4015 events. Upon further inspection of these 27 events, 6 gave a clear indication of a real additional energy deposition. Using this fraction, one would expect 47 events in the 20% data sample and could thus account for all of the events in the high energy tail. However, the cuts applied to the total data sample will change this fraction. It is difficult to assess the effects of the cuts on the light flasher energies since the light flasher energies are not subject to timing requirements in the trigger and other possible biases which exist in the 20% data sample. However, if one just uses the known effects of the cuts on the 20% data sample, we obtain 7.8 events in the high energy tail attributable to this source. Although the evidence is not conclusive, there does seem to be an indication that some fraction of the high energy tail is due to EVENT HISTORY inefficiencies.

If the high energy tail is due to extra particles hitting the calorimeter within the ADC gate time, then some number of these extra particles will show up as additional pulse height in the beam defining counters. To study this effect, one can look at the pulse height distribution of the beam counter B0. Figure 34 is a plot of the B0 distribution for the 43 events beyond 450 GeV. Also shown in figure 34 is the single

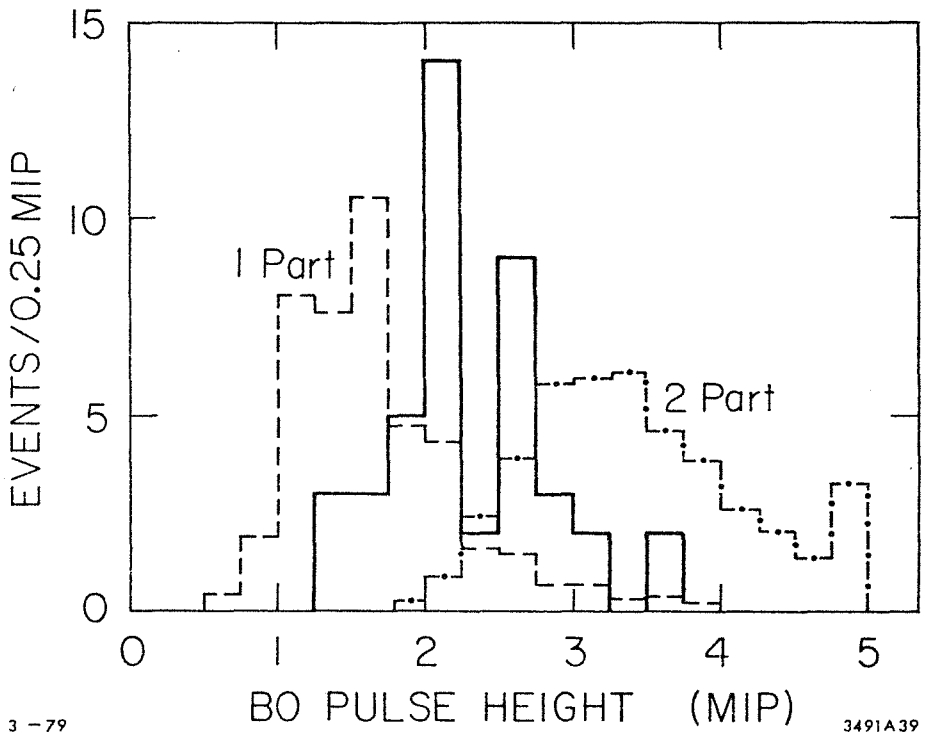

Fig. 34 The pulse height distribution for the beam defining counter B0 for the 43 high energy tail events discussed in the text. The dashed histograms are the single particle (1 PART) and two particle (2 PART) distributions normalized to 43 events. The last bin in the two particle distribution represents the overflow for pulse heights greater than 5 m.i.p.

particle and two particle (calculated from the single particle) B0 distribution normalized to 43 events. Although the actual distribution resembles neither of these other distributions, it appears that there is some contribution due to two particles. A fit constraining the sum of the single and two particle contributions to be equal to the total yields 18 ± 3 single particle and 25 ± 3 two particle events in the above distribution with a X^2 of 35 for 6 degrees of freedom. The poor X^2 simply indicates that the one and two particle contributions are not clearly resolvable in the B0 pulse height distribution. Nevertheless, this does provide additional evidence that the high energy tail is due to a real extra deposition of energy.

After subtracting the number of events from double hits in the EVENT HISTORY correction and 2 particles in the B0 distribution, one is left with 1 ± 6 events. This is within statistical accuracy of being zero. The above discussion thus provides evidence that the high energy tail is due to additional energy deposition and that the physics of the low energy tail is not affected by this deviation.

C. Missing Energy Monte Carlo

The production of neutrinos or neutrino-like particles will produce an enhanced low energy tail on the measured energy distribution. How much enhancement will depend on the production dynamics of these particles and on the resolution of the calorimeter. A Monte Carlo calculation was performed to determine the effect of the production of these particles. The neutrino-like particles are assumed to be produced in the primary proton interaction with a nonvariant cross section of the

form

$$\frac{d^3\sigma}{dp^3} = f(x_F, p_T)$$

where p_T is the transverse momentum of the particle, and x_F is the Feynman scaling variable.

$$x_F = P_L^*/P_{L\,MAX}^*$$

$P_{L\,MAX}^*$ is the maximum kinematically allowed momentum in the center of mass. After transforming to the lab frame, the response of the calorimeter is determined by the relations

$$\overline{E}_{MEAS} = 400 - E_\nu \; ; \; \sigma_{MEAS} = 13.85 \; (\overline{E}_{MEAS}/400)^{\frac{1}{2}}$$

where E_ν is the neutrino (or neutrino-like particle) energy in the lab frame, $\overline{E}_{MEAS}$ is the average measured energy, σ_{MEAS} is the width, and 13.85 is the calorimeter resolution at 400 GeV from the fit discussed previously. The square root dependence is obtained from the study of the resolution versus incident beam energy discussed in Chapter V. A random number is chosen from a Gaussian probability distribution with a mean and width given by the above relations to simulate the calorimeter. This calculation was then performed a large number of times to obtain the probability distribution, $P(E_{MEAS})$, the probability per produced neutrino-like particle that the calorimeter will measure a given energy E_{MEAS}. A comparison of these theoretical probabilities to the data will yield the amount of neutrino-like particles in the calorimetry data for the particular dynamic functions $f(x_F, p_T)$ chosen.

D. Maximum Likelihood Analysis

Because of the limited statistics involved in the tail of the measured energy, the actual limits for the production of these neutrino-like particles are determined using a maximum likelihood method. In this method, one calculates the likelihood function for a given number of produced particles, N. That is the function

$$L(N) = \prod_{i=1}^{N_{BINS}} P_i(N)$$

where the total product is over all of the bins in Table IV. $P_i(N)$ is the probability that the data in the ith bin originated from the production of N particles. This probability is assumed to obey a Poisson distribution

$$P_i(N) = \frac{(\overline{N}_i)^{N_i} \, e^{-\overline{N}_i}}{N_i!}$$

where N_i is the number of events in the ith bin. The value $\overline{N}_i$ is determined from the theoretical probabilities, P_i, the Gaussian background, G_i, and the number, N, from the relation

$$\overline{N}_i = G_i + NP_i$$

The number of produced particles, N, is then that value which maximized L(N). To determine the confidence limit, one needs only to integrate L(N) from zero up to that value of N_f such that

$$\int_0^{N_f} L(N')dN' = f \int_0^{\infty} (L(N')dN'$$

The value f determines the confidence level of N_f. If f equals .66 then $N_{.66}$ is the 66 percent confidence limit. If f equals .9 then $N_{.90}$ is the 90 percent limit and so on. A typical likelihood function is shown in figure 35 with the confidence limits indicated.

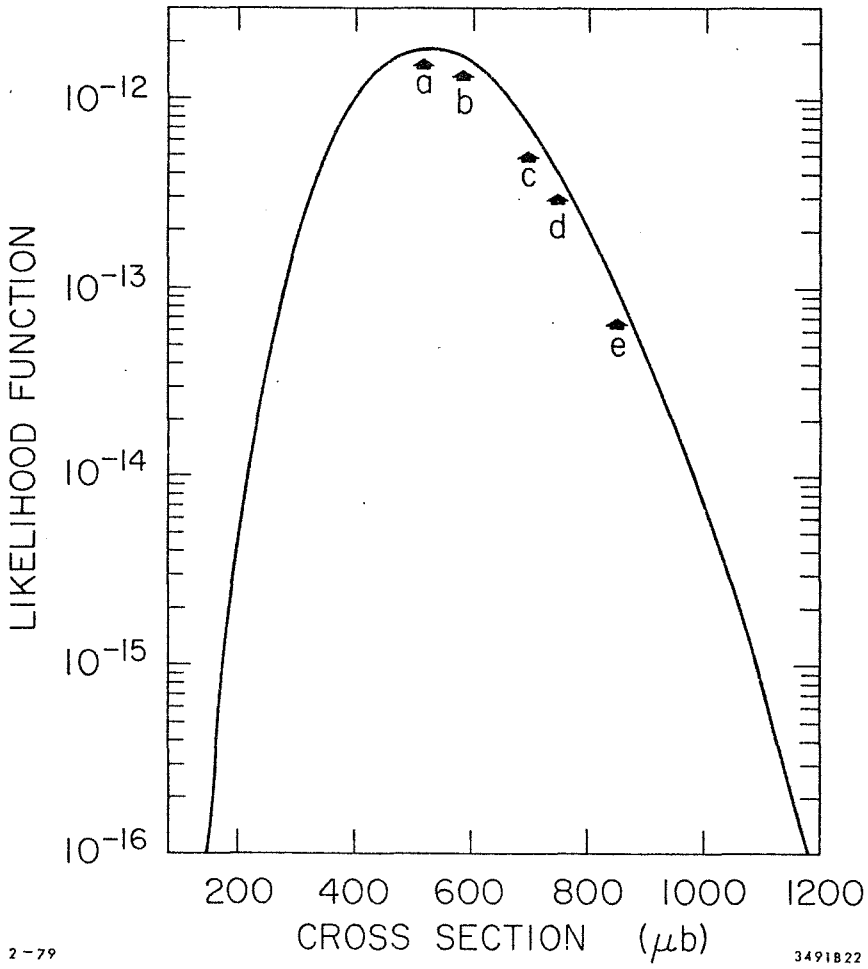

Fig. 35 Typical likelihood function as a function of cross section for the low energy distribution in figure 32. Points a, b, c, d, and e are respectively the maximum, 66% confidence level, 90% confidence level, 95% confidence level, and the 99% confidence level.

1. Supersymmetric Particles

The distribution of figure 32 can be used to set limits on the production of R-hadrons, the supersymmetric analog to the normal hadrons discussed in Chapter II. To do this, a model is needed for the production of these particles. In this model it is assumed that the R-hadron and its anti-particle are produced as an associated pair in the interaction. To account for phase space correlation of the pair produced R-hadron and its anti R-hadron, it is assumed that the R-hadron and its anti R-hadron are produced as a "particle" of mass M {49} with

$$M = 2\,M_R + \Delta$$

where M_R is the mass of the R-hadron. The additional mass Δ is assumed to obey an exponential distribution

$$\frac{d\sigma}{d\Delta} \propto e^{-2\Delta}$$

The particle of mass M is then assumed to be produced with the double differential cross section

$$\frac{d^2\sigma}{dx_F dp_T{}^2} \propto (1 - |x_F|)^n e^{-bp_T}$$

The measured hadronic production of the $\psi(3100)$ is of the form above with n = 5 and b = 2 {24} so that the distribution is probably reasonable for the production of a heavy particle with new quantum numbers. In particular, n = 5 and b = 2 were also used for R-hadron production as well. The "particle" is then allowed to decay into two R-hadrons. These individual R-hadrons are then assumed to decay into two pions and a nuino {27} (either a photino or a gluino as discussed in Chapter II)

$$M_R \rightarrow \pi\pi\ \nu_R$$

The mass of the R-hadron is not known and several values of M_R were used to estimate the dependence of the cross section on the R-hadron mass. Also, since the exact form of the differential distribution is not known, several values for this parameter were tried.

The 95% confidence limits for the parameters used are shown in Table V. It is assumed that the cross section for R-hadron production obeys a linear dependence on the atomic weight of the target particle, in this case Fe. The cross section limit is small for the more massive particles and decreases with decreasing n. The value of 33 μbarns for a M = 1 GeV appears already significant. Theoretical considerations on the nature of supersymmetric interactions would indicate a substantially larger cross section if indeed the gluino was massless {27}. This small limit already indicates that contemporary theoretical ideas regarding supersymmetry may require some alterations {27}.

2. Charm Production

A viable source for the production of prompt neutrinos would be the production and weak decay of some new heavy particle, presumably charm. A Monte Carlo calculation using the model presented in the following discussion was used to estimate the charm production cross section limits derived from the data in Table IV.

Hadronic charm production is presumably manifested as the production of D-$\overline{D}$ pairs in proton-nucleus interactions, the D meson being the lightest known charmed hadron. The pair production of the D-$\overline{D}$ pair has been considered in two ways. The first treats the D and $\overline{D}$ as being produced independently. The second has the D and $\overline{D}$ correlated

Table V.

Supersymmetric particle limits

Mass (GeV)	Production Spectra $\frac{d^3\sigma}{dx_F dp_T^2} \propto (1 - \lvert x_F \rvert)^a e^{-bp_T}$	Cross Section Limit (μbarns)
	Case 1	
.5	a = 5 b = 2	107
1	a = 4 b = 2	35
1	a = 5 b = 2	43
1	a = 6 b = 2	52
3	a = 5 b = 2	11
5	a = 5 b = 2	5
	Case 2	
.5	a = 5 b = 2	82
1	a = 4 b = 2	26
1	a = 5 b = 2	33
1	a = 6 b = 2	39
3	a = 5 b = 2	8
5	a = 5 b = 2	3
	Case 3	
.5	a = 5 b = 2	35
1	a = 4 b = 2	11
1	a = 5 b = 2	14
1	a = 6 b = 2	17
3	a = 5 b = 2	3
5	a = 5 b = 2	1

in phase space. This correlation is accomplished by producing the D-$\bar{D}$ pair as a $\psi''(3770)$ and then allowing the $\psi''(3770)$ to undergo a two body-decay into the D and $\bar{D}$ similar in spirit to the supersymmetry calculation. The differential cross section for the hadronic production of the $\psi''(3770)$ was taken to be of the form

$$\frac{d^2\sigma}{dx_F dp_T^2} \propto (1 - |x_F|)^n e^{-bp_T}$$

As previously mentioned the measured $\psi(3100)$ production cross section is of the form above with n = 5 and b = 2 {24}. Since there is no real model for charm production, this analysis also takes the values n = 5 and b = 2 for charm production. For independent production of the D-$\bar{D}$ pair, the individual Ds were taken to obey this distribution.

Measurements from e^+e^- annihilations provide data on the decays of the charmed meson. The semileptonic decays are well described by the decay

$$D \to K \begin{Bmatrix} e \\ \mu \end{Bmatrix} \nu$$
$$\to K^*(890) \begin{Bmatrix} e \\ \mu \end{Bmatrix} \nu$$

with approximately equal portions of K and $K^*(890)$. The total branching ratio into electrons (muons) is approximately 11%.

The total neutrino spectrum from charm production and decay consists of several components. The electron semileptonic decays contribute to this spectrum both from the decay of a single D and also when both of the produced Ds decay. There is also a contribution from muon decays where the muon ranges out in the calorimeter. This implies a muon of less than 3.5 GeV. Again both single decays and double decays of the D mesons contribute to these muon range out events as well. A

typical lab energy neutrino spectrum for D_{e3} decay is shown in figure 36. The total neutrino spectrum from these contributions is determined from the total semileptonic decay branching ratio (.11) for each produced D-$\bar{D}$ pair from the relation

$$E_{MEAS} = 2(1 - .11)\left(D_{e3}(\text{SINGLE DECAY}) + D_{\mu 3}(\text{SINGLE DECAY})\right)$$
$$+ .11\left(D_{e3}(\text{DOUBLE DECAY}) + D_{\mu 3}(\text{DOUBLE DECAY})\right)$$

where D_{e3} (SINGLE DECAY) is the calorimeter energy spectrum from D_{e3} decay of a single D. D_{e3}(DOUBLE DECAY) is this spectrum for simultaneous decay of both Ds. $D_{\mu 3}$(SINGLE DECAY) is the calorimeter energy spectrum for $D_{\mu 3}$ decay of a single D when the lab energy of the muon is less than 3.5 GeV and $D_{\mu 3}$(DOUBLE DECAY) is the same spectrum for simultaneous decay of both Ds. The number of decaying D-$\bar{D}$ pairs is calculated from this neutrino spectrum and the distribution in figure 32. To get the total number of D-$\bar{D}$ pairs, this number is divided by the semileptonic branching ratio, 11%.

The maximum likelihood 95% confidence level upper limit from the data yield values shown in Table VI. Again, it is assumed that charm particle production varies linearly with the atomic number of the target particle. Those labeled "Associated" refer to correlated production of the D-$\bar{D}$ pair. Those labeled "Inclusive" refer to independent production of the individual Ds.

How do these measurements compare with other experiments which search for charm particles? Unfortunately, the statistical weight of this measurement is such that this result is consistent with all previous searches. This measurement is directly related to the prompt neutrino measurements from the CERN beam dump experiments {4}. To

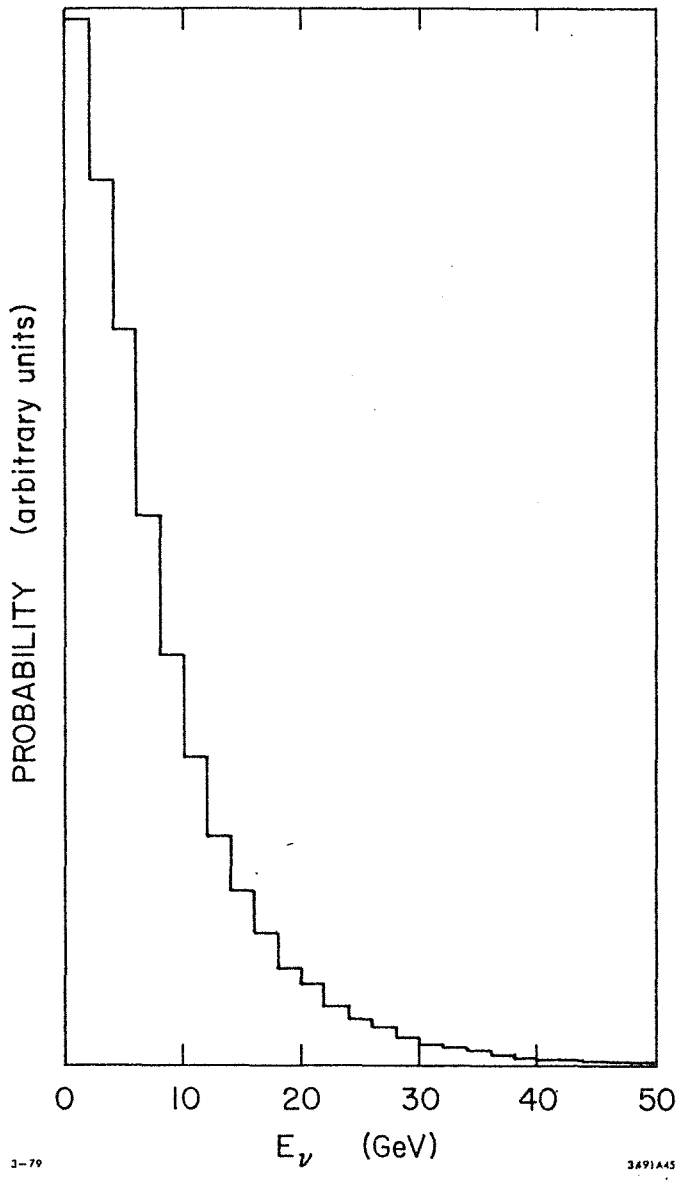

Fig. 36 Laboratory neutrino energy spectrum expected from D_{e3} decay.

Table VI.

Charm particle limits

Parameterization	Cross Section Limit (μbarns)
Case 1	
ASSOCIATED	845
INCLUSIVE	287
CERN	944
Case 2	
ASSOCIATED	670
INCLUSIVE	212
CERN	686
Case 3	
ASSOCIATED	291
INCLUSIVE	90
CERN	293

compare this measurement to those experiments, the charm production model assumed by those experiments was used to calculate the calorimeter response expected in this experiment using the Monte Carlo program. In this model, the D and $\overline{D}$ are produced independently with a double differential distribution of

$$E \frac{d^2\sigma}{dx_F dp_T^2} \propto (1 - |x_F|)^3 e^{-p_T/.7}$$

The semileptonic decay spectrum in this model is the same as previously discussed. Using the same prescription for calculating the total calorimeter energy spectrum from the individual D_{e3}, $D_{\mu 3}$

contributions, the maximum likelihood calculation of the 95% confidence level upper limit produces values also shown in Table VI labeled "CERN." To compare with the beam dump experiments, the charm cross section is taken to obey an $A^{2/3}$ dependence on the atomic weight of the target particle. These limits are consistent with the 100-400 μbarn charm cross sections reported by these experiments.

3. General Particle Production

In a very general way, the distribution in figure 31 can be used to set limits on the production of a large class of neutrino-like particles. To accomplish this, the double differential cross section for the production of these particles is assumed to be of the form

$$\frac{d^2\sigma}{dx_F dp_T^2} \propto (1 - |x_F|)^{\alpha} e^{-\beta p_T}$$

The production limits are then studied as a function of the parameters α and β. The 95% confidence limit for various values and for different masses of these neutrino-like particles are shown in Table VII. A linear dependence on the atomic weight is assumed. A quick perusal of these numbers indicate that the production of any new neutrino-like particle has to be greatly suppressed.

The axion discussed in the second chapter falls into this category of non-interacting particles. To determine the axion contribution to the distribution of figure 32, a Monte Carlo calculation is performed using the theoretically motivated assumption {29,50} that axions are produced with the same distribution as π^os. The π^o energy spectrum is assumed to obey the radial scaling prescription of Taylor et al.

Table VII.

General particle limits (μbarns)

M = 1 MeV

Case 1

β/α	0	2	4	6	8	10
1	4.0	5.1	6.2	7.3	8.2	9.2
3	4.2	5.8	8.2	10.5	13.5	17.2
5	4.2	6.0	8.2	11.0	14.3	18.4

Case 2

β/α	0	2	4	6	8	10
1	1.9	2.7	3.5	4.5	5.4	6.3
3	1.9	3.0	4.4	6.3	8.5	11.3
5	1.9	3.0	4.5	6.5	8.9	12.1

Case 3

β/α	0	2	4	6	8	10
1	1.0	1.3	1.6	2.0	2.3	2.7
3	1.0	1.4	2.0	2.7	3.7	4.8
5	1.0	1.5	2.1	2.9	3.9	5.2

M = 2.5 GeV

Case 1

β/α	0	2	4	6	8	10
1	3.8	4.3	4.6	4.9	5.1	5.3
3	3.9	4.8	5.6	6.3	6.8	7.4
5	3.9	4.8	5.8	6.5	7.3	7.8

Case 2

β/α	0	2	4	6	8	10
1	1.8	2.3	2.7	3.0	3.2	3.5
3	1.8	2.6	3.3	4.0	4.6	5.2
5	1.9	2.5	3.3	4.1	4.7	5.4

Case 3

β/α	0	2	4	6	8	10
1	.9	1.1	1.2	1.3	1.4	1.5
3	.9	1.2	1.5	1.7	2.0	2.1
5	1.0	1.2	1.5	1.8	2.1	2.3

M = 5.0 GeV

Case 1

β	α	μbarns
1	0-10	3.2-2.3
3	0-10	3.4-2.5
5	0-10	3.4-2.5

Case 2

1	0-10	1.5-1.3
3	0-10	1.5-1.4
5	0-10	1.5-1.4

Case 3

1	0-10	.8-.6
3	0-10	.8-.7
5	0-10	.8-.4

{48} for the inclusive production of secondary particles in proton-proton interactions. In the radial scaling formalism the invariant cross section is written in the form

$$E \frac{d^3\sigma}{dp^3} = A(x_R) \left[1 + p_T^2/M^2(x_R)\right]^{-q(x_R)}$$

where $A(x_R)$, $M^2(x_R)$, and $q(x_R)$ are all functions of the radial scaling variable

$$x_R = E^*/E^*_{MAX}$$

where E^* is the center of mass energy of the secondary particle and E^*_{MAX} is the maximum allowed energy for this secondary particle consistent with kinematic and quantum number constraints. The lab energy spectrum obtained from the invariant cross section above has been modified to account for nuclear effects by the relation

$$\left.\frac{d\sigma}{dx_{LAB}}\right)_A = A^{\alpha(x_{LAB})} \left.\frac{d\sigma}{dx_{LAB}}\right)_P$$

where $\left.\frac{d\sigma}{dx_{LAB}}\right)_A$ is the lab momentum spectrum for particles produced in proton-nuclear interactions with a nucleus of atomic number A. $\left.\frac{d\sigma}{dx_{LAB}}\right)_P$ is the same spectrum for A = 1, and $\alpha(x_{LAB})$ is a function of the lab momentum

$$x_{LAB} = P_L^{LAB}/400$$

$\alpha(x_{LAB})$ was taken to be

$$\alpha(x_{LAB}) = \begin{cases} .165 - 1.65\, x_{LAB} & 0 < x_{LAB} \leq .1 \\ .0375 - .375\, x_{LAB} & .1 < x_{LAB} \leq .3 \\ -.25\, x_{LAB} & .3 < x_{LAB} \leq 1 \end{cases}$$

This parameterization has been extrapolated from measurements of particle spectra from proton-nucleus collisions {51}. Since pions are produced with an $A^{2/3}$ dependence on atomic weight, this dependence is also

assumed for axion production. Table VIII shows the 95% confidence level upper limits for two possible masses of the axion. Also shown is the ratio

$$R = \sigma(pN \rightarrow a^{o})/\sigma(pN \rightarrow \pi^{o})$$

The value of 130 mbarns/nucleon has been used for $\sigma(pN \rightarrow \pi^{o})$ as measured in proton-proton interactions {52}. The values in Table VIII are certainly consistent with the results of the CERN beam dump experiments.

Table VIII.

Axion production limits

Mass (GeV)	Cross Section Limit (μbarns)	R
	Case 1	
.001	165	$10^{-2.9}$
1	125	$10^{-3.1}$
	Case 2	
.001	112	$10^{-3.1}$
1	87	$10^{-3.3}$
	Case 3	
.001	48	$10^{-3.4}$
1	37	$10^{-3.5}$

Although the beam dump experiments do not quote the model used in calculating the axion acceptance, it is clear that the beam dump experiments are more sensitive to the detection of the axion than a calorimetry search since these experiments are not rate limited like a calorimetry experiment. However, should the axion properties be different than the

accepted model, then the beam dump limits would vary. In particular, if the lifetime were less than presently believed, the beam dump limits would have to be corrected for lifetime effects whereas a calorimetry search is still sensitive as long as $\tau > 10^{-9}$ secs. It is also worth repeating that a model assumption for the interaction cross section has to be made to interpret the beam dump results as a limit on the production cross section for the axion. Although this is also true for a calorimetry search, the calorimetry search is much less sensitive to these assumptions since it is only the upper limit on the interaction cross section which is of importance in the calorimetry experiment.

E. Conclusions

This thesis was a novel attempt to measure possible production of neutral weakly interacting particles, either neutrinos or neutrino-like particles, in proton-nuclear interactions. The signature for such production would be energy nonconservation in the interaction manifest as an enhanced tail on the low energy side of the measured energy distribution of a hadron calorimeter.

To maximize the experimental sensitivity to such production, the analysis of the calorimeter data has strived to obtain the best resolution possible. This was done by first determining a precise calibration for the calorimeter including corrections for the hadron shower components, then cutting the data to eliminate spurious low energy tails often associated with hadron calorimetry. Lastly, corrections have been applied to the data to alleviate effects such as

particle pile up and gain shifts due to high counting rate in the calorimeter phototubes. The final resolution of 3.51% for the total measured energy distribution compares favorably with measurements performed with other hadron calorimeters {53}. This final distribution shows a small enhancement over the Gaussian fit to the low side of the measured energy.

Although the sensitivity of the experiment is limited, the data have established that the production of any new neutrino-like particle is less than 20 μbarns at the 95% confidence level. The 95% confidence limits obtained by interpreting the low energy tail of the measured energy distribution as due to neutrino production leads to values for charm production which are consistent, if somewhat less sensitive, to other complimentary measurements in the high energy beam dumps. The experiment has also established that axions are produced at less than .001 times the rate of π^0 production in proton-nuclear interactions. This limit is consistent with, although 5 orders of magnitude larger than, the upper limit of 10^{-8} established by the high energy beam dump experiments.

APPENDIX A

Hadron Calorimetry

Calorimetry methods were first used in cosmic ray physics to measure the energies of very energetic particles {54}. Cosmic ray energies can be large (several TeV) and preclude magnetic analysis. However, they can be measured by total absorption methods. With the advent of very high energy accelerators, particle physicists quickly incorporated these techniques. Several of the many applications include measuring scaling variable distributions in neutrino interactions {55}, measurement of neutron energy {56}, and a high transverse momentum trigger for a multi-particle spectrometer {57}, Recently, calorimetry techniques have been actively pursued as nonmagnetic energy measurement for use in experiments at proton-proton colliding beam facilities {58}. This experiment uses calorimetric techniques in a novel way to infer neutrino or neutrino-like particle production in hadron-hadron interactions. This particle production manifests itself in two ways. One way is a shift in the mean measured energy for events with a muon in the final state (the other lepton in the semi-leptonic decay which gave rise to a neutrino). The other would be a significant tail on the measured energy distribution from events with a very energetic neutrino or neutrino-like particle produced in the interaction. In either case, it is clear that a fundamental understanding of the loss mechanisms in the calorimeter is important. This is necessary for a quantitative discussion of "missing energy". It is useful then to discuss briefly the physics and fundamental limitations of hadron calorimetry methods {59}. It is worth noting that one of the PEP

experiments (MAC) is attempting to measure the neutrino associated with semi-leptonic decays of particles produced in positron-electron annihilations in a similar way {60}.

1. Physical Processes in Hadron Calorimetry

When you mention calorimetry one immediately thinks of measuring chemical reactions by changes in temperature. Similar techniques in particle physics are not feasible. A 400 GeV particle interacting in the first part of our calorimeter (10 tons of steel) will only raise the temperature of the steel by 10^{-14} degrees.

Fortunately, an indirect measurement of this heat can be made. This technique uses the fact that this heat is manifested as electron-ion pairs in the medium due to the ionization of its atoms. To a good approximation, the energy of ionization is some constant value E_{ION} for a single electron-ion pair. Therefore, if one just counts the number of ion pairs and associates an energy E_{ION} with each one, by energy conservation the incident particle energy is

$$E_{INCIDENT} = E_{ION} I_0 = E_{ION} \int_0^\infty \frac{dI(x)}{dx}\, dx$$

where I_0 is the total number of pairs and $\frac{dI(x)}{dx}$ is the number of pairs in a width dx at a depth x in the medium. The incident energy is thus proportional to the sum of the number of particles counted at various depths in the medium.

The shower created in the medium consists of electromagnetic and hadronic components. The electromagnetic component, arising from decays of π^0s produced in the medium, consists of a shower of electrons

and photons due to such processes as pair production, bremsstrahlung, ionization, and Compton scattering. The number of electrons in these showers are very large. For instance, a 10 GeV shower will have on the average approximately 50 electrons at the peak of the shower. The hadronic component of the shower is more complicated since these particles can interact with the nuclei in the medium. In these interactions some fraction of the produced particles are neutral pions and will decay into two photons initiating electromagnetic cascades in the medium. The rest of the energy will go into the production of charged secondaries (pions, kaons, nucleons, etc.). In addition, a fraction of the energy of the interaction will go into nuclear break up. Hadrons produced in these secondary interactions will have tertiary interactions and so on. This nuclear-electromagnetic cascade will continue until particle production is no longer kinematically possible, at which point the hadron will range out or be absorbed in the nucleus. One sees then that the actual particle number measured at various thicknesses will be a complicated function of this nuclear-electromagnetic cascade.

The actual shape of the shower profile can be estimated by noting that the number of particles from electromagnetic cascades is much larger than that due to ionization by relativistic charged particles. Thus, the energy going into neutral pions will, to a large extent, determine the total number measured. One can naively sketch a "typical" shower profile. Since the neutral pions from the first interaction will have most of the electromagnetic energy (on the average one-sixth of the incident particle energy), the decays of these neutral pions will give a large peak in the ionizatin profile, labeled 1 in

figure 37 . Since the neutral pions from the second, third, etc. generations of interactions will be of much lower energy, they will show up as a small extended distribution, labeled 2 in figure 37. The sum will yield the total profile shape, labeled curve 3 in figure 37. This "typical" profile should be compared to the measured profile for a 400 GeV proton shower in our calorimeter shown in figure 38. Clearly, on an event by event basis, the profile shape will vary dramatically. This is simply due to the statistical nature of the nuclear interaction.

Although all of the energy of the incident particle will be lost in the medium not all of it will be measured. This is true for several reasons. First, a fraction of the energy will be lost in overcoming nuclear binding effects. Secondly, the heavily ionizing particles produced in the nuclear break up will saturate the dE/dx in the medium and thus not obey the linear relation above {61}. These mechanisms play a major role in hadron calorimetry and provide a lower limit on the ultimate resolution obtainable. This can be seen by noting that the average number of interactions in the calorimeter for a 400 GeV proton is around 300. Monte Carlo calculations indicate that approximately 80 GeV of the initial proton energy is lost by this mechanism.

2. Calorimeter Design Considerations

The important physical parameters of a calorimeter are

(i) the hadronic absorption length of the medium

(ii) the total length and transverse dimension of the medium

(iii) the radiation length of the medium

(iv) the distance between successive detection layers

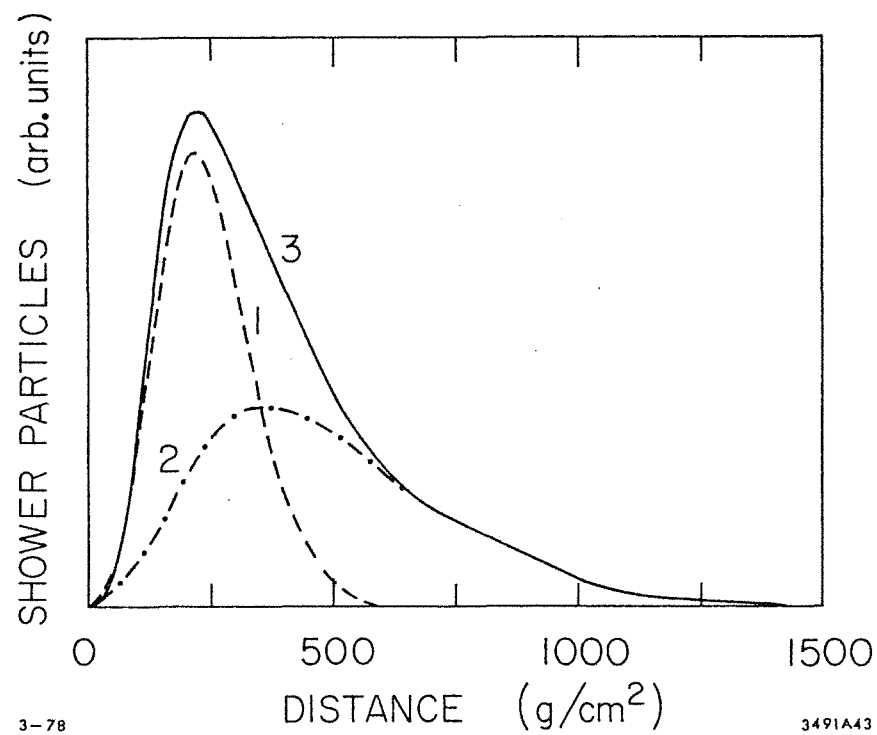

Fig. 37 Typical calorimeter pulse height distribution. Curve 1 is due to π^os from the primary interaction, curve 2 is from particle production in the secondary interactions, and curve 3 is the sum of curves 1 and 2.

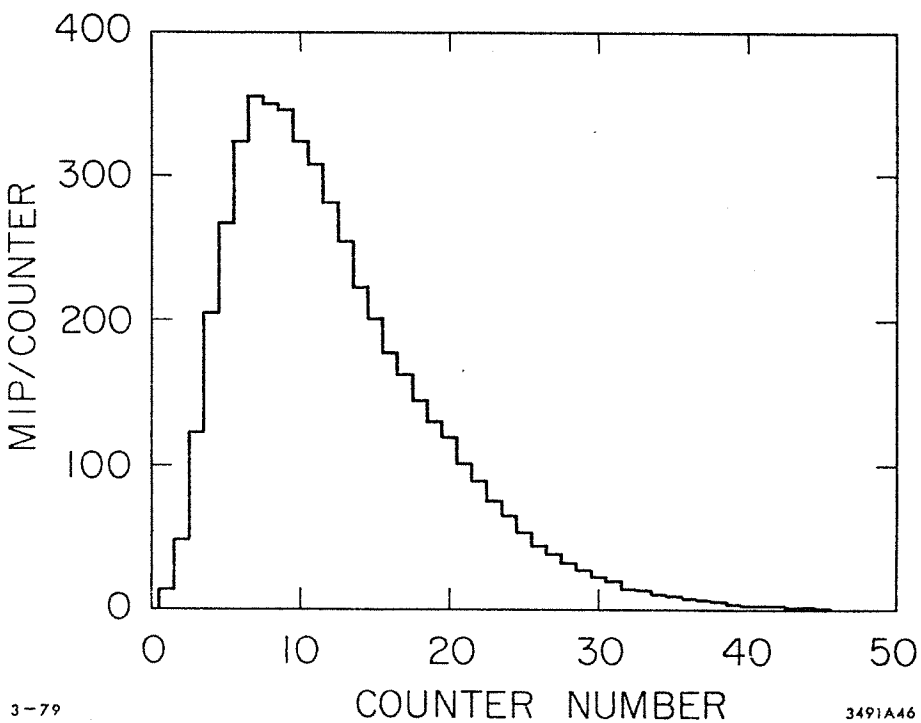

Fig. 38 Average shower profile for a 400 GeV shower in the calorimeter used in this thesis.

The material properties of interest are the radiation length and hadronic absorption length of the medium. The hadronic absorption length of the medium should be as short as possible. This stems from the fact that for calorimetry methods to be useful, one must contain the whole nuclear cascade. Generally, the nuclear cascade has dissipated after 10 or 11 nuclear interaction lengths, although this does depend on the incident energy {62}. However, fluctuations in the longitudinal development are large. To contain these fluctuations, a calorimeter with a somewhat larger number of interaction lengths is required. The calorimeter used in this experiment is 17½ interaction lengths total. In addition, a short interaction length reduces the number of pions that decay causing a low energy tail.

It is absolutely imperative that the total length of the calorimeter be long enough to contain the nuclear cascade. Only a few percent loss out of the back of a calorimeter will change the resolution by a factor of two. This can be traced to fluctuations in the longitudinal development of the shower. Although on the average only a small percentage of the energy is lost, there will be events with significant punch through out the back of the calorimeter. Not only does this ruin the resolution, but worse, introduces nonGaussian tails on the low side of the energy measurement. The data from this experiment can be used to indicate the size of this effect by simulating a calorimeter of somewhat shorter length. Figure 39 shows the calorimeter measured energy for the full calorimeter (solid histogram) and for a calorimeter which consists only of the first 30 plates (40 inches of steel total). Although the average measured energy is only slightly less for the 30

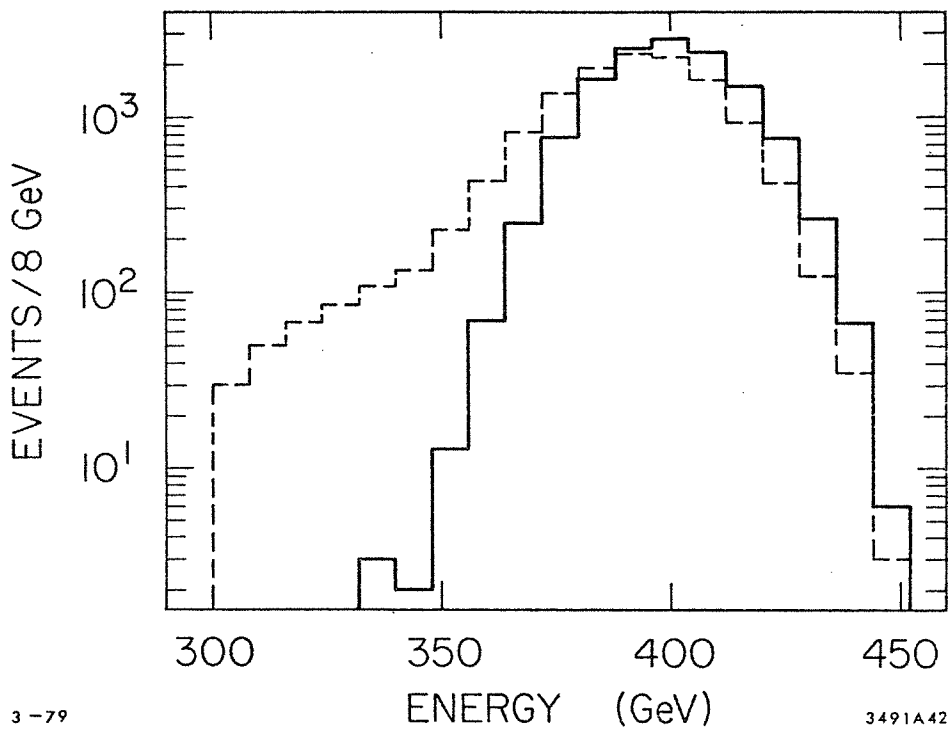

Fig. 39 Calorimeter measured energy for the full calorimeter (approximately 3 meters) (solid histogram) and the same distribution for a calorimeter consisting of only the first 30 plates (approximately 1.3 meters) (dashed histogram, arbitrarily cut off at 300 GeV). Non-containment in the second case leads to nonGaussian behavior in the low side of the measured energy.

plates case (389 GeV versus 400 for the full calorimeter), the resolution is worse by almost a factor of 2 (6.38% versus 3.63% for the full calorimeter). The low energy distribution for the shorter calorimeter is highly nonGaussian.

These same comments also hold true for the transverse size of the calorimeter as well. It should be large enough for complete transverse containment. The number of interaction lengths required to contain the shower transverse to its axis is not well known. For this calorimeter, the measured energy in the most expanded configuration is 7% less than the measured energy in the most compacted configuration with a 40% increase in the width of the distribution. This reduction in measured energy is presumably due to particles being lost out the side of the calorimeter. A Monte Carlo calculation indicates that approximately 800 MeV of energy is being lost transversely in the most compacted configuration of the calorimeter.

The shower in the calorimeter will consist of an electromagnetic component which will roughly determine the number of particles counted and a hadronic component which will determine the shower length. As noted, the hadronic absorption length should be kept short in order to keep the total amount of material at a minimum yet still contain the shower. Since the radiation length of the medium governs the electromagnetic shower, one would like to sample the shower frequently enough on this scale to reduce fluctuations in the measured energy from this sampling error. However, since the radiation length is proportional to Z^2 and the hadronic length is proportional to A, the requirement of a short interaction length implies a short radiation

length. Thus, to sample the electromagnetic component well, the sample spacing must be very small. But a small sample spacing implies that the sampling material becomes an appreciable fraction of the density, thus increasing the effective absorption length and giving rise to increased probability for pions in the shower to decay. In practice, one has to optimize the material used in order to compromise these two conflicting specifications. The criteria for optimization will depend on the actual physics use.

The effects of the sample spacing can be seen by realizing that the sampling is just an approximation to the total integral of the shower profile. The increment in depth times the energy at a given depth approximates the total energy. Thus, the sample spacing should be as small as possible. As previously noted, the sample spacing should be a good match to the radiation length in the medium, but not so small as to cause adverse effects on the hadronic absorption length. Also, the cost goes up quickly with a decrease in the sample spacing. The data from this experiment can also be used to indicate the effects of sample spacing as well. This is done by effectively neglecting counter information and assuming a different effective spacing. Figure 40 shows the results of this analysis. The spacing factor in that figure is defined as the distance between successive counters, i.e. scale factor 2 means that every other counter is taken to give pulse height information. No attempt has been made to eliminate possible systematic effects in Figure 40 induced by selecting specific counters in the calorimeter such as possible bad counters or slightly different attenuations. Nevertheless, it still gives one a feeling for the degradation in the resolution with increasing sample size.

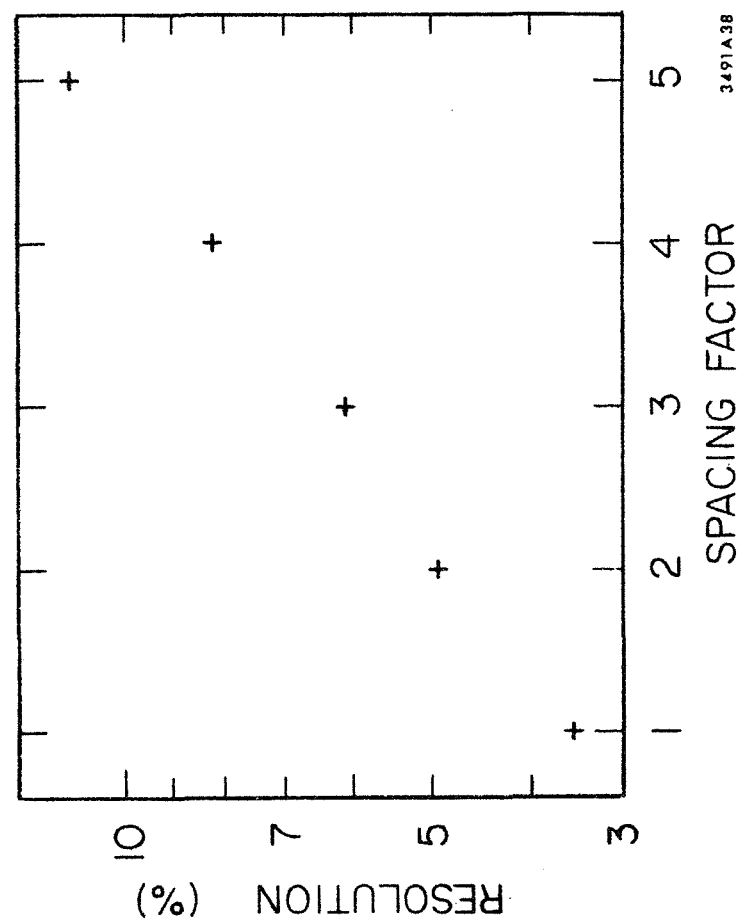

Fig. 40 Calorimeter resolution versus sample spacing. The spacing factor is the factor increasing the sample size from the nominal calorimeter sampling distance (spacing factor = 1.). The crosses serve only as data point demarcations and do not reflect errors in the data points.

APPENDIX B

Photomultiplier Gain Tests

At a very high beam rate, several of the phototubes could have as much as 100 μA of current in the phototube during the spill. Measurements were performed on each phototube to determine the effects of these large currents on the gain of the phototube.

A schematic of the test set up is shown in figure 41. Briefly, the phototube signal from the pulsing LED was integrated with the ADC and then converted to an analog signal to drive the chart recorder. This pulsing LED was coupled to the ADC using a capacitor. This a.c. coupling separated the gain measurement of this pulsing LED from the d.c. background due to the second LED. The second LED was used to mimic large background currents from the high rate. The gain of each tested phototube was equalized using an Americium source imbedded in a NaI(Tl) crystal. The beam spill was simulated by an electronic timing mechanism which turned the second LED on for 1 second every 11 seconds. In this situation, a higher beam rate was simulated by a larger voltage across the second LED giving rise to a larger current at the anode of the phototube from this d.c. LED. The test consisted of studying the behavior of the pulsing LED signal versus the d.c. current at the anode due to this second LED.

The effects caused by the large current varied considerably among the tested phototubes. Some phototubes had a negative gain shift while others showed positive gain shifts. The test results for two typical phototubes are shown in figure 42. The results of these tests were used in placing the phototubes on the counters in the calorimeter.

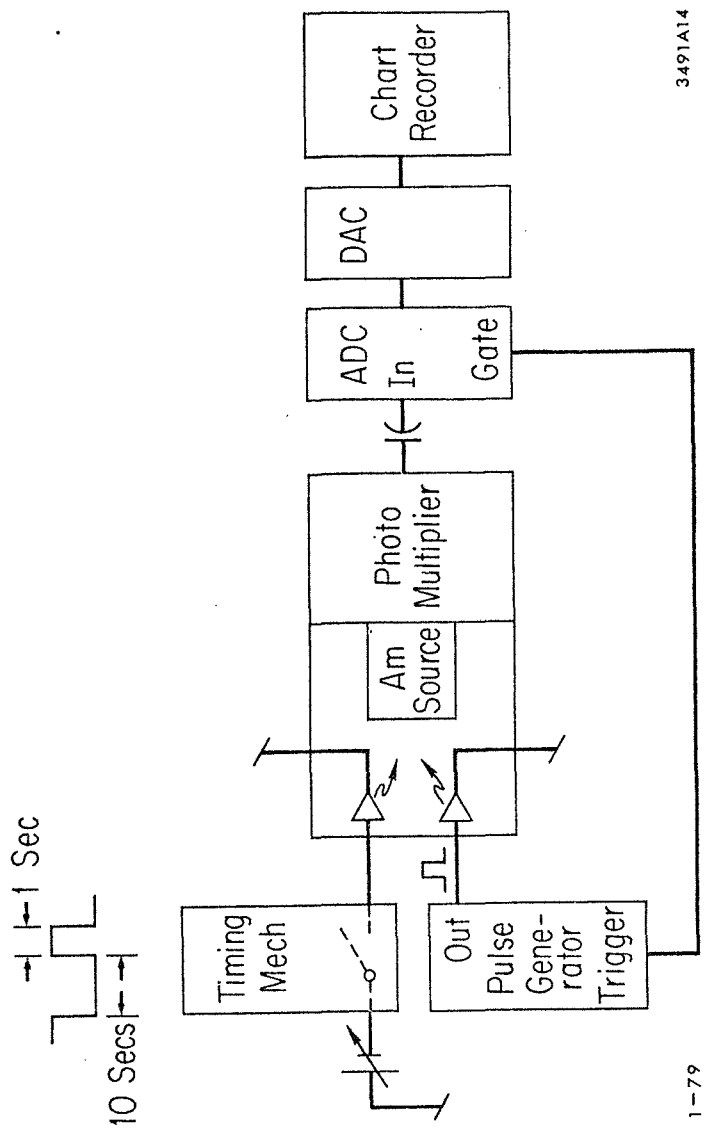

Fig. 41 Schematic of the apparatus used in the photomultiplier gain measurements. The timing mechanism turned on the d.c. LED for 1 second every 11 seconds to mimic the FNAL spill structure.

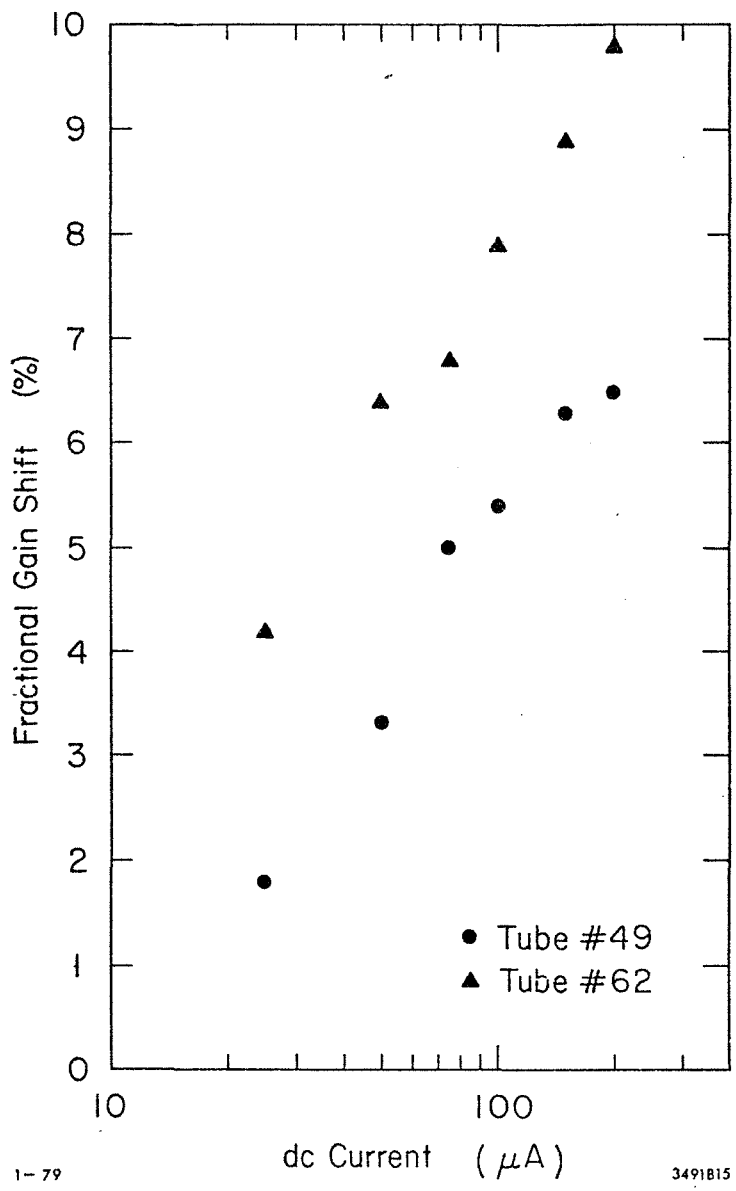

Fig. 42 Typical results from the gain test measurements. The abscissa is the amount of current at the anode of the photomultiplier due to the d.c. LED.

Those phototubes that showed only a minor variation with d.c. current were placed on the counters near shower maximum with those tubes with significant effects being disbursed in portions of the calorimeter with a small average number of particles. In addition, an attempt was made to alternate the sign of the rate effect in phototubes on contiguous counters in order to partially cancel residual effects due to the high rate. Even after these precautions, the measured energy still suffered from large beam rates as discussed in Chapter V.

References

1. Particle Data Group, Phys. Lett. 75B, 1 (1978).
2. J. Bjorken and S. Glashow, Phys. Lett. 11, 255 (1964); S. Glashow et al., Phys. Rev. D2, 1285 (1970); M. Gaillard et al., Rev. Mod. Phys. 47 277 (1975); J. Ellis et al., Nucl. Phys. B100, 313 (1975); G. Goldhaber et al., Phys. Rev. Lett. 37, 255 1976).
3. W. Bacino et al., Phys. Rev. Lett. 40, 671 (1978); J. Feller et al., Phys. Rev. Lett. 40, 274 (1978); R. Brandelik et al., Phys. Lett. 70B, 387 (1977).
4. P. Alibran, et al., Phys. Lett. 74B, 134 (1978); T. Hansl et al., Phys. Lett. 74B, 139 (1978); P. C. Bosetti et al., Phys. Lett. 74B 143 (1978); B. P. Roe et al., Michigan Preprint UM-HE-78-44 and Proceedings of the Bartol Research Foundation Workshop on Charm Production and Lifetimes, October 1978; H. Wachsmuth, CERN Preprint, CERN/EP/PHYS 78-29 and Proc. of the Topical Conference on Neutrino Physics, Oxford July 1978.
5. R. Diebold, Argonne Preprint ANL-HEP-CP-78-45 and Proceedings of the 14th International Conference on High Energy Physics, Tokyo, Japan, August 1978.
6. J. Babcock, D. Sivers, and J. Wolframm, Phys. Rev. D18, 162 (1978); C. E. Carlson and R. Suaya, SLAC-PUB-2212, October 1978.
7. E. J. Bleser et al., Phys. Rev. Lett. 35, 76 (1975); M. A. Abolins et al., Phys. Rev. Lett. 37, 417 (1976); D. Bintinger et al., Phys. Rev. Lett. 37, 732 (1976); J. C. Alder et al., Phys. Lett. 66B, 401 (1977); D. Spelbring et al., Phys. Rev. Lett. 40, 605 (1978).
8. W. R. Ditzler et al., Phys. Lett. 71B, 451 (1977).
9. G. Coremans-Bertrand et al., Phys. Lett. 65B, 480 (1976); W. Bozzoli et al., Lett. Nuovo Cim. 19 32 (1977); N. Ushida et al., Lett. Nuovo Cim. 23, 577 (1978); F. Merritt, private communication.

10. D. J. Crennell, C. M. Fisher, and R. L. Sekulin, Phys. Lett. 78B, 171 (1978).
11. J. Kirkby, Proceedings of the Summer Institute on Particle Physics, SLAC Report No. 215 (1978).
12. L. Baum et al., Phys. Lett. 77B, 337 (1978); A. G. Clark et al., Phys. Lett. 77B, 339 (1978).
13. R. Lipton et al., Phys. Rev. Lett. 40, 608 (1978).
14. B. C. Barish et al., Caltech Report CALT 68-655 and Proceedings of Third International Conference at Vanderbilt University, March, 1978; B. C. Barish et al., Proceedings of the Bartol Research Foundation Workshop on Charm Production and Lifetimes, October, 1978; K. Wyatt Brown, Ph.D. Thesis, California Institute of Technology, 1979.
15. M. J. Lauterbach et al., Phys. Rev. Lett. 37, 1436 (1976); M. J. Lauterbach et al., Phys. Rev. D17, 2507 (1978).
16. M. Perl, Phys. Rev. Lett. 35, 1489 (1975); S. Wojcicki, Proceedings of the Summer Institute on Particle Physics, SLAC Report No. 215 (1978).
17. G. Alexander et al., Phys. Lett. 81B, 84 (1979); W. Bacino et al., SLAC-PUB-2249, Jan. 1978 (to be published in Phys. Rev. Lett.).
18. M. J. Shochet, Proceedings of the Summer Institute on Particle Physics, SLAC Report No. 204, Nov. 1977.
19. S. Weinberg, Phys. Rev. Lett. 19, 1264 (1967); A. Salam, Elementary Particle Theory, Proceedings of the Eighth Nobel Symposium, ed. N. Svartholm (Almquist and Forlag, Stockholm, 1968); F. J. Hasert et al., 46B, 138 (1973); A. Benvenuti et al., Phys. Rev. Lett.

32, 800 (1974); F. S. Merritt et al., Caltech Preprint CALT-68-495, May 1975.

20. S. D. Drell and T. M. Yan, Phys. Rev. Lett. 25, 316, (1970); C. Quigg, Rev. Mod. Phys. 49, 297 (1977).

21. J. J. Aubert et al., Phys. Rev. Lett. 33, 1404 (1974); T. E. Augustin et al., Phys. Rev. Lett. 33, 1406 (1974).

22. J. Rich and D. R. Winn., Phys. Rev., D14, 1283 (1976).

23. B. Knapp et al., Phys. Rev. Lett. 34, 1044 (1975); F. W. Busser et al., Phys. Lett. 56B, 482 (1975); H. D. Snyder et al., Phys. Rev. Lett. 36, 1415 (1976); K. J. Anderson et al., Phys. Rev. Lett. 37, 799 (1976); M. Binkley et al., Phys. Rev. Lett. 37, 574 (1976); Yu. M. Antipov et al., Phys. Lett. 60B, 309 (1976); G. J. Blaner et al., Phys. Rev. Lett. 35, 346 (1975); J. G. Branson et al., Phys. Rev. Lett. 38, 1331 (1977); M. J. Corden et al., Phys. Lett. 68B, 96 (1977); J. H. Cobb et al., Phys. Lett. 68B, 101 (1977); E. Amaldi et al., Lett. al Nuovo Cimento 19, 152 (1977); B. C. Brown et al., preprint FERMILAB-77/54-EXP; A. Bamberger et al., Nucl. Phys. B134, 1 (1979); T. B. W. Kirk et al., Phys. Rev. Lett. 42, 619 (1979); K. J. Anderson et al., Phys. Rev. Lett. 36, 237 (1976); Yu. M. Antipov et al., Phys. Lett. 72B, 278 (1977); Y. B. Bushnin et al., Phys. Lett. 72B, 269 (1977); J. H. Cobb et al., Phys. Lett. 72B, 497, (1978).

24. E. J. Siskind, Ph.D. Thesis, California Institute of Technology, 1979.

25. J. Wess and B. Zumino, Nucl. Phys. B70, 39 (1974); Phys. Lett. 49B, 52 (1974); Nucl. Phys. B78, 1 (1974); P. Fayet and S. Ferrara, Phys. Rept. 32C, 249 (1977).

26. G. R. Farrar, Caltech Preprint CALT-68-681 (1978) and Proceedings of Interantional School of Subnuclear Physics, Erice, Sicily, August 1978.

27. P. Fayet, Phys. Lett. 64B, 156 (1977); G. R. Farrar and P. Fayet, Phys. Lett. 76B 575 (1978); Phys. Lett 79B, 442 (1978).

28. J. Ellis, Proceedings of the Summer Institute on Particle Physics, SLAC Report No. 215, November 1978.

29. S. Weinberg, Phys. Rev. Lett. 40, 223 (1978); F. Wilczek, Phys. Rev. Lett. 40, 279 (1978).

30. B. W. Lee and R. E. Shrock, Phys. Rev. D17, 2410 (1978).

31. R. Cahn, Phys. Rev. Lett. 40, 80 (1978).

32. A. A. Belavin et al., Phys. Lett. 59B, 85 (1975); G. 't Hooft, Phys. Rev. Lett. 37, 8 (1976); C. G. Callen et al., Phys. Lett. 63B, 334 (1976); R. Jackiw and C. Rebbi, Phys. Rev. Lett. 37, 172 (1976).

33. G. 't Hooft, Phys. Lett. 37, 8 (1976) and Phys. Rev. D14, 3432 (1976).

34. R. D. Peccei and H. R. Quinn, Phys. Rev. Lett. 38, 1440, (1977); R. D. Peccei and H. R. Quinn. Phys. Rev. D16, 1791 (1977).

35. J. Kandaswamy et al., Phys. Lett. 74B, 377 (1978); T. Goldman and C. E. Hoffman, Phys. Rev. Lett. 40, 220 (1978); J. Klems et al., Phys. Rev. D4, 66 (1971).

36. J. Ellis and M. K. Gaillard, Phys. Lett. 74B, 374 (1978).

37. K. T. Mahanthappa and Marc A. Sher, Phys. Rev. D18, 848 (1978).

38. P. Ramond and G. G. Ross, Caltech Preprint CALT-68-674 (1978).

39. A. Zepeda, Phys. Rev. Lett. 41, 139 (1978); N. G. Deshpande and D. E. Soper, Phys. Rev. Lett. 41, 735 (1978).

40. S. Weinberg, in A Festshrift for I. I. Rabi, Lloyd Motz, ed. (New York Academy of Sciences, New York, 1977), and references quoted therein.

41. L. B. Leipuner et al., Phys. Rev. Lett. 31, 1226 (1973); J. A. Appel et al., Phys. Rev. Lett. 32, 428 (1974); J. W. Cronin et al., Phys. Rev. D10, 3093 (1974); D. Bintinger et al., Phys. Rev. Lett. 34, 982 (1975); M. G. Albrow et al., Nucl. Phys. B97, 189 (1975); R. Vidal et al., Phys. Lett. 77B, 344 (1978); D. Cutts et al., Phys. Rev. Lett. 41, 363 (1978).

42. H. R. Gustafson et al., Phys. Rev. Lett 37, 474 (1976).

43. D. J. Bechis et al., Phys. Rev. Lett. 40, 602 (1978).

44. J. Lach and S. Pruss, Fermilab note TM-285 (1971).

45. Ken Kesey, One Flew Over the Cuckoo's Nest, a novel (Viking Press, New York, 1962).

46. LeCroy Research Systems Corporation, Technical Data Sheet, CAMAC model 2249A, December 1975.

47. G. B. Bondarenko et al., as cited by V. Lebedev, Proceedings of the XVI International Conference on High Energy Physics, Batavia 1973; J. P. Boymond et al., Phys. Rev. Lett. 33, 112 (1974); J. A. Appel et al., Phys. Rev. Lett. 33, 722 (1974); J. W. Cronin, Proceeding of the International School of Subnuclear Physics, Erice, Italy, 1975; L. M. Lederman, Phys. Repts. 26C, 149 (1976).

48. F. E. Taylor et al., Phys. Rev. D14, 1217 (1976).

49. M. Bourquin and J. M. Gaillard, Nucl. Phys. B114, 334 (1976).

50. H. Quinn, private communication.

51. C. Halliwell et al., Phys. Rev. Lett. 39, 1499 (1977); D. Chaney et al., Phys. Rev. Lett. 40, 71 (1978); D. Burke et al., Michigan

Preprint UM-HE-78-6, April 1978.

52. For the total π^0 cross section in pp collisions see J. Whitmore, Phys. Rep. 27C, 187 (1976).

53. A review of earlier calorimetry work can be found in F. Sciulli, Proceedings of the Calorimeter Workshop, M. Atac editor, Fermilab 1975. Reports of other high energy calorimeter measurements can be found in L. W. Jones et al., Nucl. Instr. and Meth. 118, 431 (1974); A. Benvenuti et al., Nucl. Instr. and Meth. 125, 447 (1975); B. C. Barish et al., Nucl. Instr. and Meth. 130, 49 (1975); M. Holder et al., Nucl. Instr. and Meth. 151, 69 (1978).

54. N. L. Grigorov, V. Z. Murzin, and I. D. Rapaport, J. Exptl. Theor. Phys. 34, 506 (1958) (English translation in Sov. Phys. JETP 7, 348 (1958)).

55. A. Benvenuti et al., Nucl. Instr. and Meth. 125, 447 (1975); B. C. Barish et al., Nucl. Instr. and Meth. 130, 49 (1975); M. Holder et al., Nucl. Instr. and Meth. 151, 69 (1978).

56. M. N. Kriesler et al., Phys. Rev. Lett. 20, 468 (1968); L. W. Jones et al., Nucl. Instr. and Meth. 118, 431 (1974).

57. C. Bromberg et al., Nucl. Phys. B134, 189 (1978); M. D. Corcoran et al., Phys. Rev. Lett. 41, 1447 (1978).

58. C. Akerloff et al., Proceedings of the ISABELLE Summer Workshop, BNL Report 50721, Brookhaven National Laboratory, Upton, New York, July 1977.

59. A significant portion of the following presentation is taken from V. S. Murzin, Progress in Elementary Particle and Cosmic Ray Physics Vol. 9 (North Holland Publ. Co., Amsterdam, 1967). For a general discussion of all phases of hadron calorimetry see

Proceedings of the Calorimeter Workshop, M. Atac editor, Fermilab, Batavia, Illinois, May 1975.

60. R. L. Anderson et al., PEP Proposal PEP-6, Positron Electron Project, Stanford Linear Accelerator Center, Stanford University, December 1975.

61. J. B. Birks, The Theory and Practice of Scintillation Counting (The MacMillan Co., New York, 1964); T. A. Gabriel and J. D. Amburgey, Nucl. Instr. and Meth. 116, 333 (1974).

62. F. Sciulli, Proceedings of the Calorimeter Workshop, M. Atac editor, Fermilab, Batavia, Illinois, May 1975, page 79.